Effects of collisions on the magnetic streaming instability

Loïc Nicolas

▶ **To cite this version:**

Loïc Nicolas. Effects of collisions on the magnetic streaming instability. Physics [physics]. Université Pierre et Marie Curie - Paris VI, 2017. English. NNT : 2017PA066229 . tel-01686142

HAL Id: tel-01686142
https://theses.hal.science/tel-01686142

Submitted on 17 Jan 2018

HAL is a multi-disciplinary open access archive for the deposit and dissemination of scientific research documents, whether they are published or not. The documents may come from teaching and research institutions in France or abroad, or from public or private research centers.

L'archive ouverte pluridisciplinaire **HAL**, est destinée au dépôt et à la diffusion de documents scientifiques de niveau recherche, publiés ou non, émanant des établissements d'enseignement et de recherche français ou étrangers, des laboratoires publics ou privés.

PhD THESIS
OF THE UNIVERSITÉ PIERRE ET MARIE CURIE

presented by

Loïc Nicolas

Submitted in fulfillment of the requirements for the degree of

DOCTEUR ÈS SCIENCES
DE L'UNIVERSITÉ PIERRE ET MARIE CURIE

Spéciality :

Sciences de la Terre et de l'Environnement
et Physique de l'Univers, Paris (ED AA)

Effects of collisions on the magnetic streaming instability

Defended on 2017 in front of the committee:

Ms Caterina Riconda	1	1	President
Mr Mark Sherlock	2	2	Referee
Mr Stefano Gabici	3	3	Referee
Ms Elena Amato	4	4	Examiner
Mr Alexandre Marcowith	5	5	Examiner
Mr Roch Smets	6	6	Supervisor
Mr Andrea Ciardi	7	7	Supervisor

Except where otherwise noted, this work is licensed under
http://creativecommons.org/licenses/by-nc-nd/3.0/

If you're certain, you're certainly wrong, because nothing deserves certainty.
Bertrand Russell Speaks His Mind (1960), Bertrand Russell

Acknowledgement

Ces trois années de thèse ont constitué une excellente expérience, qui m'a beaucoup apporté à la fois sur le plan scientifique, méthodologique, technique, mais aussi humain, ce qui n'est pas à négliger. Beaucoup de monde y a contribué, d'une manière ou d'une autre, et c'est à eux que cette partie est dédiée.

Je voudrais tout d'abord remercier Pascal Chabert et Darek Lis, directeurs respectifs du LPP et du LERMA, de m'avoir accueilli au sein de leur laboratoire. J'y ai beaucoup appris, notamment au conseil de laboratoire du LPP où j'ai eu l'occasion de représenter les doctorants.

I would like to thank the jury of my thesis, for having taken the time to evaluate my work with a careful reading of my manuscript, and for paying a close attention to my defense. They provided doubleplusgood corrections and discussions on the topic. These valuable comments and relevant questions, both on the manuscript and on the presentation, were of the most importance in correcting the mistakes and imprecisions I may have made, which only made this work stronger.

Je voudrais également remercier mes deux directeurs de thèse, Roch Smets et Andrea Ciardi, qui m'ont accompagné au cours de ces trois ans (et même plus). Leurs différents domaines de compétences m'ont permis d'aborder mon sujet sous différents angles, ce qui a indubitablement contribué à la manière dont nous avons pu aborder le problème ensemble. Leurs personnalités ont aussi favorisé les conversations aussi intéressantes qu'agréables. Le financement de cette thèse a été obtenu par Roch et Andrea dans le cadre du Labex Plas@Par, que je remercie également pour cela. Ce travail réalisé dans le cadre du LABEX Plas@Par a bénéficié d'une aide de l'État gérée par l'Agence Nationale de la Recherche au titre du programme Investissements d'avenir portant la référence ANR-11-IDEX-0004-02.

Je n'aurais pas pu en arriver jusque là sans le soutien de ma famille. Mes parents, en particulier, qui m'ont porté jusqu'au point où j'en suis, encourageant toute initiative et curiosité. Biljana m'a également supporté et encouragé avec une constance et une énergie salutaires au cours de ces années. Merci pour ça.

Mes amis aussi m'ont été d'un soutien très précieux pendant le déroulement de cette thèse. Que ce soit lors de conversation portant sur des aspects techniques (des morceaux de code, Rémy m'a dépanné plus d'une fois) ou des conversations sur tout sauf la physique, ces moments ont été importants.

Mes collègues, enfin, ont été d'une grande aide au cours de ces années. Les Gary, pour commencer, cette bande de joyeux lurons qui forment la garysphère du LERMA. Les Gary de première génération, bien sûr, qui partageaient mon bureau, mais aussi ceux de seconde et troisième génération qui faisaient vivre ce laboratoire. Les collègues côté LPP également, ont leur part de contribution dans le travail ici présenté.

Je pourrais aussi citer les diverses entités non-humaines qui m'ont été d'un grand secours dans mes nombreux problème d'ordre technique. Les sites comme Stackoverflow ou Wikipedia cumulent une part non-négligeable du temps que j'ai passé sur cette thèse, de même que l'inévitable Google.

Si l'on s'intéresse à ce sur quoi porte ce manuscrit, on constate qu'il va parler de plasma, puisque c'est le champ d'étude qui nous intéresse ici, et on le constate par les 276 occurrences de ce mot dans le rapport. Ceci tient compte des formes plurielles et ne tient pas compte de la casse, et inclut le corps du texte uniquement (sans page de titre, table des matières, listes des figures et des tables, bibliographies et abstract), y compris les légendes des figures mais pas le contenu même des figures. On s'intéresse aux particules, mentionnées 313 fois (en comptant la mention des macroparticules), mais également aux ondes, 191 fois, qui n'a été trouvé associé avec l'adjectif "polarisé" que 10 fois, alors que c'est un mot clé de la thèse. Ces ondes, qui se manifestent d'ailleurs dans le champ magnétique cité pas moins de 341 fois, peuvent interagir avec les particules via un processus de résonance qui a été rapporté à 122 reprises (ce qui comprend en fait également la mention des processus non-résonants, mais ne compte pas les acronymes comme RHR ou LHR, ce qui pourrait faire largement gonfler les chiffres). Cela forme une partie du cœur de ce sujet, qui est l'instabilité, mot présent 244 fois tout de même, associé avec le mot "streaming" 62 fois pour former un autre des mots-clés. Mais le but avoué de ce travail est d'étudier l'effet sur cette instabilité des collisions, dont il est fait mention le nombre astronomique de 542 fois, ce qui en fait le mot-clé le mieux choisi. Le contexte astrophysique, en particulier des rayons cosmiques, n'est rapporté qu'à 32 reprises, et le modèle numérique utilisé (le modèle hybride), bien que détaillé dans un chapitre, n'apparaît que 9 fois, ce qui en fait le mot-clé le moins récurrent du manuscrit.

Je n'ai pas pu mentionner toutes les personnes qui m'ont apporté leur soutien lors de ces trois années. Je m'excuse auprès de ceux que je n'aurais pas cité, mais le cœur y était et je vous remercie tout de même, tous.

Paris, 2017

Contents

List of figures

List of tables

Chapter 1

Introduction

> One original thought is worth a thousand mindless quotings.
>
> Attributed to Diogenes of Sinope in: William Safire (2001), Let a simile be your umbrella.

The visible world seems essentially made of neutral matter, for which gravitational force is the only one at play. But at astrophysical scale, most of the visible matter in the universe is made of a charged particles called plasma, where electromagnetic force play a leading role in its dynamics. Even though plasmas could be seen by mankind since its origin (the Sun or lightning), their study is a relatively recent field of study since the first scientific description of such state comes from the second part of the nineteenth century. Plasma physics has since been the object of numerous studies, ranging from the study of astrophysical processes to nuclear fusion for energy production.

In plasma physics, because of the coupling between the constituent charged particle and the electromagnetic fields, there exist a very wide range of plasma waves. Furthermore, in the presence of a source of free energy (bulk velocity, temperature anisotropy, density gradient...), these waves can be unstable. Plasma instabilities are very common in both natural and laboratory plasmas. Their study is an important research topic with wide ranging applications from astrophysical plasmas, fusion devices to electric discharges.

The magnetic streaming instability arises when two magnetized plasmas stream into each other with a relative velocity higher than the local Alfvén speed. Under such conditions, the electromagnetic normal modes (waves) of the plasma are unstable and their amplitude grows exponentially. The kinetic energy of the streaming particles feeds the growing waves, which react by scattering the particles. Their direct ordered motion is thus randomized, leading to a decrease of the relative streaming velocity of the plasmas, and finally to the saturation of the instability.

The magnetized streaming instability has many applications in the space and astrophysical plasmas, where most of these plasmas are bathed in a magnetic field (whether it comes from a near star, a planet or a galaxy). As an example, the instability is thought play a key role in the development of low-frequency electromagnetic modes that are driven by unstable ion beams upstream of the Earth bow shock (see Onsager, Winske, and Thomsen 1991), which are self-generated by the shock itself. One of the numerous

applications of the magnetic streaming instability lies in the interaction of cosmic rays with the interstellar medium. Cosmic rays are high energy particles (from MeV to ZeV) essentially of galactic origin (see Zweibel 2013). First observed at the beginning of the 20th century, they were initially thought to be energetic photons, but were later identified as charged particles. The original name, however, sticked and we still call cosmic rays these energetic particles. The acceleration mechanisms that allow the cosmic rays to reach very high energies (above 10^{10} eV) is still a current topic of study, and the scientific community currently believes that a variety of acceleration mechanisms are at play in different sources and generate cosmic rays of different energies. One of these acceleration mechanisms require strong magnetic fields at supernovae shocks, that bounce cosmic rays across the shock like a ball in a tennis game (see Marcowith et al. 2016). The generation of these strong magnetic fields also involve the work of the magnetic streaming instability.

The interstellar medium is the tenuous gas that fills the galaxy between the stellar systems. The term interstellar medium gather a vast number of different physical conditions, from the dense and cold molecular clouds to the hotter and tenuous medium (see Ferrière 2001). This medium bathes in a galactic magnetic field, whose origin is still debated in the scientific community since its discovery in 1949. In this interstellar medium, the cold molecular clouds are the place of star formation. In order to allow the gravitational collapse to take place, the medium need to not be too coupled to the magnetic field, otherwise the magnetic pressure would oppose the collapse. This uncoupling can be achieved by regulating the ionization of the molecular clouds, and cosmic rays are believed to play an important role in this regulation (see Padovani et al. 2014).

Cosmic rays streaming through the interstellar medium can trigger the magnetic streaming instability. This is a source of energy exchange that transfers the kinetic energy of the cosmic rays to the background. This generates an enhanced wave activity, which confines the (low energy) cosmic rays to low, bulk streaming velocities (see Padoan and Scalo 2005). Cosmic rays are in fact believed to play an important role in the ionization of molecular clouds. Because of the increase of the collision cross section with particle energy, this ionization process is effective for cosmic rays with energy ranging from 10 to 100 MeV.

By their very definition, plasmas dynamics is largely dominated by collective effects due to electromagnetic effects. Indeed, any gas will statistically contain a number of charged particles, but this portion is so low that the charged particles will have practically no effect on the general dynamics of the system. When a neutral gas starts to carry a large enough number of charged particles, they start to experience collective effects due to electric and magnetic fields. In such a plasma state, we can distinguish two forms of electromagnetic fields: the one externally applied or induced by the general behaviour of the plasma like the waves, and that we call macroscopic field, and the one generated by individual particles that we call microscopic field. At small scale, the dynamics of a charged particle can be modified by another charged particle in a close neighbourhood, which makes a Coulomb collision. At larger scale, the shielding resulting from other particles soften the associated electric force. The scale length associated to the limit between these two behaviours is the Debye length, meaning that particle collisions occur at smaller scales, inside the Debye sphere (see Trubnikov 1965). In many plasmas, such as the solar wind, the dynamics is totally determined by the macroscopic fields, the collision mean

free path being of the order of the Sun-Earth distance. But in dense enough plasma, microscopic fields due to the charge of the particles play an important part in the dynamics, by modifying the trajectory of particles entering the Debye sphere of another particle. These Coulomb collisions are an efficient way to scatter particles in phase space, hence modifying their velocity and pitch-angle.

The context of this work came from a growing collaboration between Roch Smets and Andrea Ciardi on the interaction of low energy cosmic rays with the interstellar medium in 2009. After Andrea joined the LERMA, they decided to resume this study by proposing a thesis topic, to which I applied at the end of my master in Paris. I then started to work at LERMA beside a team working on the simulation of scalable laboratory experiments to study the processes happening during early stages of a star formation (such as the accretion of matter by stars or the emission of jets). Benjamin Khiar studies accretion shocks using a MHD code that was developed by Andrea during his thesis, and also participated to a collaboration with an experimental team of the LULI (another laboratory specialized in the manipulation of high power lasers) to reproduce astrophysical jets in laboratory. Julien Guyot also uses this MHD code and works on implementing a PIC module to study the acceleration of cosmic rays in astrophysical shocks. Beside my time passed in LERMA, I also had the opportunity to discuss with people in the LPP that work on numerical simulations. This field of study gathers peoples from the different teams of the lab, from magnetic fusion to cold plasma, including space plasmas.

In this thesis we study the magnetic streaming instability in both the collisionless and collisional limits using the PIC-hybrid code HECKLE, for which I have developed a Monte Carlo collision module. While the instability has been studied in the collisionless case, both analytically (in Gary 1991, Gary 1993) and numerically with kinetic codes (Winske and Leroy 1984, Wang and Lin 2003), no work exist in the literature for the collisional case. Based on these previous works, we can simulate the instability both in collisionless and collisional cases to compare and identify the effects of the collisions on it.

The work presented in this manuscript is articulated as follow. Chapter 2 gives an overview of the context of the magnetic streaming instability, including some applications to astrophysical plasmas. It also gives some elements on analytical results showing that the instability makes electromagnetic waves grow with a certain growth rate. Chapter 3 presents the numerical model we use in this study to simulate the plasma, as well as a detailed presentation of the collision module included during this work (based on Takizuka and Abe 1977). Chapter 4 presents numerical results of the magnetic streaming instability in the collisionless case, and shows the presence of three different modes, associated with different kind of waves. Chapter 5 gives results of the magnetic streaming instability in several collisional regimes, and shows that the presence of collisions have a quenching effect on the produced waves. More precisely, the beam gives part of its kinetic energy to the background plasma through collisions, which leaves less energy for the electromagnetic waves. Finally, chapter 6 gives a summary of the results and a discussion about some future works that could be done on this topic.

Bibliography

Onsager, T. G., D. Winske, and M. F. Thomsen (1991). "Interaction of a finite-length ion beam with a background plasma - Reflected ions at the quasi-parallel bow shock". In: *Journal of Geophysics Research* 96, pp. 1775–1788 (cit. on p. 1).

Zweibel, E. G. (2013). "The microphysics and macrophysics of cosmic rays". In: *Physics of Plasmas* 20.5, p. 055501 (cit. on p. 2).

Marcowith, A. et al. (2016). "The microphysics of collisionless shock waves". In: *Reports on Progress in Physics* 79.4, 046901, p. 046901 (cit. on p. 2).

Ferrière, K. M. (2001). "The interstellar environment of our galaxy". In: *Reviews of Modern Physics* 73, pp. 1031–1066 (cit. on p. 2).

Padovani, M. et al. (2014). "The role of cosmic rays on magnetic field diffusion and the formation of protostellar discs". In: *ArXiv e-prints* (cit. on p. 2).

Padoan, P. and J. Scalo (2005). "Confinement-driven Spatial Variations in the Cosmic-Ray Flux". In: *Astrophysical Journal, Letters* 624, pp. L97–L100 (cit. on p. 2).

Trubnikov, B. A. (1965). "Particle Interactions in a Fully Ionized Plasma". In: *Reviews of Plasma Physics* 1, p. 105 (cit. on p. 2).

Gary, S. P. (1991). "Electromagnetic ion/ion instabilities and their consequences in space plasmas - A review". In: *Space Science Reviews* 56, pp. 373–415 (cit. on p. 3).

— (1993). *Theory of Space Plasma Microinstabilities*, p. 193 (cit. on p. 3).

Winske, D. and M. M. Leroy (1984). "Diffuse ions produced by electromagnetic ion beam instabilities". In: *Journal of Geophysics Research* 89, pp. 2673–2688 (cit. on p. 3).

Wang, X. Y. and Y. Lin (2003). "Generation of nonlinear Alfvén and magnetosonic waves by beam-plasma interaction". In: *Physics of Plasmas* 10, pp. 3528–3538 (cit. on p. 3).

Takizuka, T. and H. Abe (1977). "A binary collision model for plasma simulation with a particle code". In: *Journal of Computational Physics* 25, pp. 205–219 (cit. on p. 3).

Chapter 2

Elements on the magnetic streaming instability

> Welcome...to the desert of the real.
>
> Morpheus - The Matrix (1999), The Wachowski.

Contents

Counter-streaming plasmas can drive waves unstable under some conditions, feeding off the kinetic energy available to produce electrostatic or electromagnetic waves that grow in time before saturating in a nonlinear phase. The drift velocity is thus reduced and the energy redistributed to relax to a more stable configuration. This type of mechanism is ubiquitous in space and astrophysical plasmas, showing a wide variety of processes under a wide variety of conditions. This chapter presents some introductory elements on streaming instabilities, then discusses some of the conditions where it can be of importance before presenting the physical processes involved in the particular instability which is the focus of this present work as well as some elements of analytical theory applied to this instability.

2.1 Streaming instabilities

We need to distinguish the two populations at play in such instability as the particles of each of these populations are playing a different role ; we call **main** (referred to with the subscript m) the core of the plasma, and **beam** (with the subscript b) the other population subject to a drift motion relative to the **main**. As instabilities have often the effect of rearranging the way energy is distributed in a system, their study is very important to the understanding of many systems, and as the streaming instabilities are ubiquitous in many environments in astrophysics (as will be seen later), this study integrates a wide field of study which tends to explain phenomena such as production of ultra-relativistic particles or early star formation. There is a wide zoology of modes and processes that are involved in a streaming configuration (whether the beam or the main are ions or electrons, with or without a magnetic field, electrostatic or electromagnetic modes...) discussed in Gary 1993 and Marcowith et al. 2016 and we will now quickly present some of them and especially the one we are interested in presently in order to put it in its context.

2.1.1 Electrostatic modes

The most simple situation is that of two homogeneous, counter-streaming plasmas where no magnetic field plays a role. When a beam of electrons streams in a plasma, this case can give rise to two electrostatic instabilities, the first being a Langmuir beam instability (as referred to by Gary 1993) in the condition:

$$\left(\frac{V_b}{v_{T,b}}\right)^3 \left(\frac{n_b}{n_0}\right) < 1 \tag{2.1}$$

with V_b and $v_{T,b}$ the beam mean velocity and thermal velocity (with the thermal energy $T_b = m_b v_{T,b}^2$), n_b the beam density and n_0 the total electron density. In that case the wave satisfy the dispersion relation:

$$\omega^2(k) = \omega_{p,e}^2 + 3k^2 v_{T,e}^2 \tag{2.2}$$

$$\omega_{p,e} = \sqrt{\frac{n_e e^2}{\varepsilon_0 m_e}} \tag{2.3}$$

with ω and k the frequency and wave number of the wave, n_e is the electron density of the medium, e the electronic charge, ε_0 the permittivity of free space and m_e the electron mass. This type of wave is observed in the Earth foreshock and generated by type 3 solar bursts (see Cairns and Robinson 1999). On the other hand, when the condition below is satisfied:

$$\left(\frac{V_b}{v_{T,b}}\right)^3 \left(\frac{n_b}{n_0}\right) \geq 1 \tag{2.4}$$

the electron/electron beam instability is triggered and the waves obey the relation:

$$\omega = kV_b \tag{2.5}$$

According to Tsurutani and Lakhina 1997, this corresponds to an inverse Landau damping, where the waves gain energy from particles faster than its phase velocity, as opposite to the Landau damping where the particles slower than a wave phase velocity gain energy from them, damping the waves in the process.

When the beam is made of ions of mass m_i and thermal energy less than the electrons $T_i \ll T_e$, an ion/ion acoustic instability occurs, provided that its drift speed is higher than the ion thermal velocity, that slows down the beam and generates waves with phase speed:

$$\frac{\omega}{k} \approx c_s \left(\frac{n_m - n_b}{n_e}\right) \tag{2.6}$$

$$c_s = \left(\frac{T_e + 3T_i}{m_i}\right)^{1/2} \tag{2.7}$$

where c_s is the ion acoustic velocity. These modes are present not only in space plasmas (see Feldman et al. 1973) but also in the laboratory, like for example in low pressure electric discharges (Sydorenko et al. 2007).

2.1.2 Electromagnetic modes

Beside electrostatic modes, particle beams or counter-streaming plasmas can drive several electromagnetic instabilities, depending on the existence of a DC magnetic field, and of the direction of the wave vector relative to this magnetic field. The stability of such systems usually depends on the drift speed of the beam and in the presence of a magnetic field, one of the conditions for the development of certain instabilities is for the relative streaming velocity to be above the Alfvén speed of the background plasma $V_A = \frac{B}{\sqrt{\mu_0 n_i m_i}}$.

When a beam of electrons is drifting in a plasma along a magnetic field, this triggers a filamentary instability and produces electromagnetic waves with frequency of the order of the electron plasma frequency, propagating perpendicular to the initial magnetic field. If the beam is made of ions, the instability develops on the time and length scales of the ion cyclotron frequency $\Omega_{C,s} = q_s B/m_s$. These are much larger than those of the electrons, and it is often the case that the electrons can be treated as a mass-less, neutralizing fluid. These instabilities, referred to in Gary 1993 as ion/ion electromagnetic instabilities, are the focus of the present work, and we shall refer to the different modes as magnetic streaming instability.

2.1.3 Anisotropy instabilities

Instabilities can also be driven by an anisotropy in the temperatures parallel and perpendicular to the magnetic field. These are often placed in the class of streaming instability, even though the growing perturbations are *not* fed by the kinetic energy associated with the relative streaming velocity between two populations, but by the anisotropy in the temperature of one or several plasma components.

The Weibel instability (see Weibel 1959, Medvedev et al. 2004) takes place when the electron perpendicular temperature exceeds the parallel one ($T_{\perp,e} > T_{\parallel,e}$), which creates electromagnetic waves propagating along the magnetic field, as explained in Cottrill et al. 2008, and restore isotropy in phase space. The firehose instability occurs when the parallel temperature is larger than the perpendicular temperature and when the parallel thermal pressure exceeds the magnetic pressure ($T_\parallel > T_\perp$ and $\beta_\parallel > 1$) and produces waves propagating along the magnetic field, relaxing the distribution to a more isotropic temperature. As opposite the mirror instability happens when the perpendicular temperature is higher than the parallel temperature, producing electromagnetic waves propagating across the magnetic field lines and also relaxing the plasma to an isotropic distribution.

2.2 Astrophysical context

Magnetic streaming instabilities are ubiquitous in many environments in space and astrophysical plasmas, and show a wide variety of conditions. In this section we approach some of the cases where this instability takes an important role in the physics of the system.

2.2.1 Earth bow shock

The interest in ion/ion-driven electromagnetic streaming instabilities in space plasmas started with satellites observation, such as the Explorer 34 mission studies in Fairfield 1969, which detected waves at about $0.01 - 0.05$ Hz upstream of the Earth bow shock, or in Russell, Childers, and Coleman 1971, who reported observations with Ogo 5 of left-handed polarized waves. These waves were originally believed to originate from ion-cyclotron resonances. However, they were instead later identified as right-hand polarized waves (once the Doppler effect on the very low frequency waves was taken into account

by considering the high speed of the spacecraft compared to the phase speed of the waves as explained in Hoppe et al. 1981) and they were proposed to originate from a population of back-streaming ions reflected by the Earth bow shock. This creates a double component plasma with the reflected ions and the incoming solar wind ions, along the solar magnetic field. This two-components ion distribution was later observed in the solar wind by Feldman et al. 1973, thus confirming the idea that back-streaming ions in the Earth bow shock may be responsible for the observed wave activity, as well as the enhanced interplanetary magnetic fields reported by Tsurutani et al. 1987. The ISEE mission (Bonifazi et al. 1980) also confirmed the presence of different ion populations in the fore-shock region shock: (i) solar wind ions with a bulk speed of the order of $V_{SW} = 300 km.s^{-1}$ and a density of $5 cm^{-3}$; (ii) reflected ions with a density around $n_D = 0.26 cm^{-3}$ speed $V_D = 541 km.s^{-1}$ and a thermal speed $v_{T,D} = 222 km.s^{-1}$; (iii) diffuse ions with a density $n_D = 0.29 cm^{-3}$ speed $V_D = 400 km.s^{-1}$ and a thermal speed $v_{T,D} = 776 km.s^{-1}$. All those components are contained in a magnetic field of ~ 10 nT.

Reflected ions are shown to drive unstable both right-hand resonant and non-resonant modes when both plasmas are homogeneous, and the relationship between the observed waves and the ion component presented above was first investigated in Winske and Leroy 1984, who studied the generation of right-hand polarized waves due to the ion/ion-driven electromagnetic streaming instability. Their numerical simulations also showed that the observed diffuse ion population component could be explained as being the result of the isotropization of the beam (reflected ions) by the instability. According to Onsager, Winske, and Thomsen 1991, the plasma and especially the beam, in the case of the bow shock, are not necessarily uniform unlike in the previous studies, so he studied the effects of the finite length of the beam and showed that the right-hand is more important than in the homogeneous case, because of the direction of propagation of the generated waves and the time the waves are in contact with the beam to interact.

2.2.2 Cometary environment

The solar wind can also interact with an ion population around comets which happen to have a distribution function relevant to the streaming instability. Such distributions were observed in the vicinity of Comet Halley in Mukai et al. 1986 by the Suisei probe, where a population of cometary ions is responsible for the generation of turbulence when interacting with the solar wind, creating a population of scattered ions called "pickup ions". An analytical model of this situation has been developed in Gary and Madland 1988 and in Yoon 1990. In this context the direction between the incoming solar wind and the solar magnetic field can vary and this was addressed by Wang and Lin 2003 where numerical simulations were carried out to study the effect of this angle. They showed that the generated waves mainly propagate along the magnetic field and in the same direction as the beam, even though oblique waves can propagate as well.

2.2.3 Interstellar medium

The interstellar medium corresponds to 10-15% of the galactic mass and shows a wide range of conditions in density and temperature, from the cold molecular clouds, with a

medium	n	T	B
molecular cloud	$10^8 - 10^{12}\mathrm{m}^{-3}$	10K	$10^{-10} - 10^{-9}T$
hot ionized gas	$10^3\mathrm{m}^{-3}$	10^6K	$10^{-9}T$
solar wind at the Earth	$5.10^6\mathrm{m}^{-3}$	10^6K	$10^{-9} - 10^{-8}T$
cometary environment	$10^5\mathrm{m}^{-3}$	10^8K	

Table 2.1: Physical conditions in the different situations.

temperature around 10 K and a density up to $10^6\mathrm{cm}^{-3}$, to relatively hot ionized gas, with a temperature around 10^6 K and a density of the order of $10^{-3}\mathrm{cm}^{-3}$ (see Ferrière 2001, which gives an overview of the different conditions in the interstellar medium, including the cosmic rays and their role in the dynamics of this matter). It is mainly composed of hydrogen (90%) and is immersed in an ambient magnetic field, which was first indirectly observed by Hall 1949 with the polarized light of stars, whose magnitude ranges from tenths to few nT. Table 2.1 gives the physical conditions for some of the situations seen in this chapter.

2.2.4 Cosmic rays

Cosmic rays (CR) are energetic particles (mostly protons) travelling throughout the galaxy. They cover a huge range of energies, from a few MeV (10^6 eV) up to few ZeV (10^{21} eV). Figure 2.1 shows the spectrum of cosmic rays, made with both Earth and spaced based detectors. Below the GeV-energies, the magnetosphere and the solar wind make it difficult to clearly identify the origin of the observed particles. At 10^6 GeV, the slope steepens and this first discontinuity is called the "knee", then the slope flattens after the "ankle" at 10^9 GeV and a cutoff happens around 10^{11} GeV, above which no CR were observed (although particles at these energies are difficult to observe with the actual detectors). The presence of several slopes in the spectrum, seems to indicate different acceleration mechanisms that are reviewed in Castellina and Donato 2011, giving a model for each energy domain: CR up to the knee at 10^6 GeV are accelerated by a process called diffusive shock acceleration (discussed in the next section) at supernova remnants (SNR); between the knee and the ankle, the acceleration of cosmic rays is still in debate, but the possibility of a subset of SNRs that can accelerate particle to higher energy than the knee due to exceptionally energetic supernovae explosions is considered (see Parizot 2014); finally above the ankle (10^9 GeV), CRs are believed to have an extra galactic origin and therefore accelerated outside our galaxy. Recent reviews of observation and the physical mechanism involved in cosmic ray transport in the interstellar medium and acceleration mechanisms are given in Blandford, Simeon, and Yuan 2014, Zweibel 2013 and Marcowith 2014.

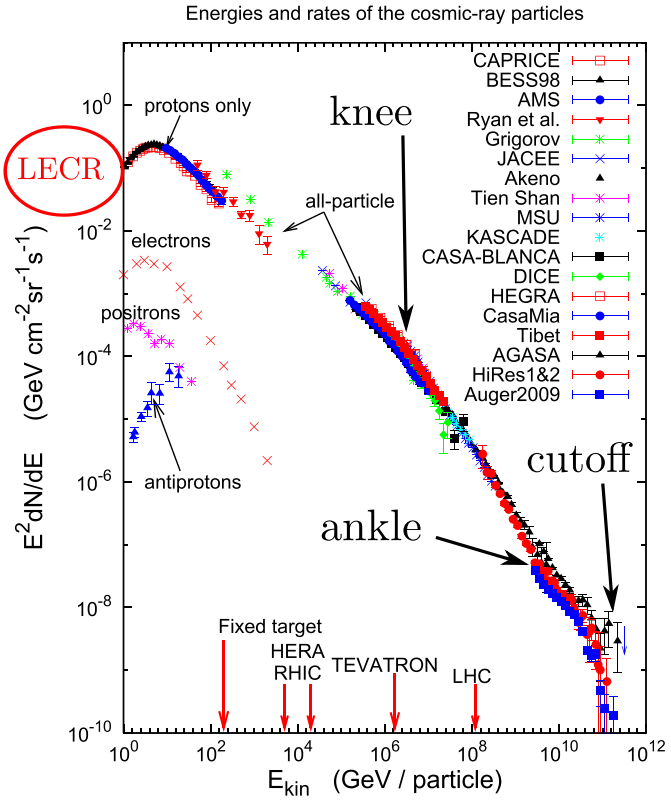

Figure 2.1: Energy spectrum of the observed cosmic rays using many experimental data. The figure is adapted from Zweibel 2013. The low energy cosmic rays (LECR, below the GeV, in the red circle) do not appear on this spectrum.

2.2.5 Supernovae shocks

The processes responsible for the acceleration of cosmic rays to the energy mentioned before need to be of high efficiency. One of these processes is thought to happen in supernovae remnant shock through a process called diffusive shock acceleration, or first-order Fermi acceleration. As explained for example in Gargaté and Spitkovsky 2012, this happens when a particle crosses many times the shock front, being reflected every time by the magnetic turbulence and gaining energy at each crossing. It can explain the first part of the CR spectrum in figure 2.1, before the knee (up to 10^6 GeV), and requires a strong magnetic turbulence and generates an energy spectrum for the particles that depends on the compression of the shock. To generate such strong magnetic field, CR are also involved trough a current-driven instability presented in Bell 2004, who developed a model to explain such a non-resonant instability. As explained in Bell et al. 2013, CR escaping from the supernovae remnant drive this instability through their current, which is able to generate magnetic fields up to hundreds of μG, and Stroman, Pohl, and Niemiec 2009 made some simulations and showed that this instability is able to amplify the initial magnetic field up to 20 times. This modifies the structure of the shock, and can explain the magnetic fields needed for the first-order Fermi acceleration to take place, which happens to generate a power-law spectrum consistent with the one of the CR up to the knee.

2.2.6 Cosmic rays in the interstellar medium

Low-energy cosmic rays (LECR, in the red area at 10-100 MeV on figure 2.1) streaming in molecular clouds in the interstellar medium (ISM) along the galactic magnetic field create a population that can interact with this medium trough the magnetic streaming instability. This transfers part of their energy in their surroundings in the form of thermal energy and slows down the CR in the densest parts of the molecular clouds (Padoan and Scalo 2005), which can explain the confinement time of CRs in the Galaxy of millions of years as explained in Amato 2011. Moreover, as discussed in Padovani, Galli, and Glassgold 2009, these CR have an important effect on the chemistry of the molecular clouds since they are a strong source of ionization for the di-hydrogen molecules. Padovani, Hennebelle, and Galli 2014 summarizes the chemical processes involving the CR and shows that when increasing the magnetic field (due to the streaming instability as proposed by Morlino and Gabici 2015), the ionization decreases, which has the effect of decoupling the cloud with the magnetic field as seen in Padovani and Galli 2013. This decoupling, together with the heating of the molecular clouds, are conditions that favor the formation of stars in protostellar disks. In a review, Bykov et al. 2013 mentions the different instabilities suspected to be responsible for the cosmic rays confinement, especially the Bell's instability (Bell 2004) along with a resonant mode.

2.3 Lab experiments

As the processes in astrophysics mostly happen on very long times compared to human timescales (the typical growth of a supernova remnant happens overs $\sim 10^6$ years and the

characteristic cosmic ray lifetime is about 10^7 years as discussed in Ferrière 2001) and length-scales, they are difficult to observe. Thus, there have been discussions about how to reproduce these phenomena in controlled experiment in laboratory. In 1964, Dawson 1964 proposed a way of producing plasma by shooting a solid or liquid target with a high power laser. This was a setup already considered for thermonuclear fusion experiment and he proposed to use it for astrophysical studies. The use of laser-produced high energy density plasmas for studying astrophysical shocks is now widely used, as in Kuramitsu et al. 2011 who reproduced cosmic rays acceleration using a laser pulse, or Fox et al. 2013 who studied Weibel-like instabilities in the context of astrophysical shocks. Weidl et al. 2016 presented simulations of laser experiments on the Large Plasma Device (with magnetic fields of 200 G, main density of $6.10^{12} cm^{-3}$ and temperature of 1eV) in order to produce an ion beam in a plasma along a magnetic field and showed evidence of the magnetic streaming instability in such conditions.

In many of the astrophysical cases presented before, Coulomb collisions between ions in the plasmas are negligible. However in some of them (interstellar medium) and in laboratory experiments, such collisions cannot be neglected. That is why we are presently interested in the effects of this kind of interaction on the magnetic streaming instability.

2.4 Collisions in a plasma

Collisions in plasmas can be due to neutral components in the plasma, but also to long-ranged Coulomb forces (in very ionized plasmas), which make them collective as the effects of many small-angle collisions overcome the effects of a few strong collisions. As these collisions are negligible in the heliosphere, all previous studies about magnetic streaming instabilities were made using the collisionless plasma hypothesis when considering kinetic models because they applied mostly to this environment. However in some cases such as high density shocks or laboratory experiments, Coulomb collision become important and must be taken into account. Collisional effects have, however, been studied for other instabilities, as in Mamun and Shukla 2000, who studied electrostatic modes and showed a damping of a dust-acoustic mode due to collisions with neutral dusts, or in Cottrill et al. 2008, who performed analytical studies of a collision operator in the context of the fast ignition and showed that the collision have a damping effect on the electrostatic instability but also the ability to enhance some electromagnetic instabilities. For the purpose of this work, we study the effects of Coulomb collisions on the previously studied collisionless instability, using a Monte-Carlo method presented in section 3.5 as a numerical collision operator.

2.5 Non-Maxwellian distribution

In the conditions where collisions are not dominant, the distribution function of the plasma can be non-Maxwellian, as observed in the near-Earth environment (see Lazar et al. 2008). Lazar et al. 2008 analytically investigated the influence of kappa distribution function (the kappa distribution is a power law instead of an exponential for the Maxwellian) on the magnetized streaming instability and showed that the growth rate is

strongly influenced by the shape of the distribution and that in the case of a kappa function, the growth rates are lower than in the Maxwellian case. However, as most studies in magnetized case were made with Maxwellian equilibrium distributions, and since we are presently interested in the effects of collisions on the instability and that collisions are expected to suppress any deviation from a Maxwellian (see section 3.6), we use Maxwellians as initial distribution functions for the ions in the simulations.

2.6 Physics of the magnetic streaming instability

During the early stage of the instability (the linear phase) the electromagnetic perturbation growth exponentially with growth rate γ ($B(t) \propto e^{\gamma t}$), then it reaches a saturation with a maximum value of the perturbation B_{max} and finally relaxes to a lower amplitude steady-state. During the linear stage, the bulk energy of the beam (associated with the bulk fluid velocity of the beam) is partially transferred to the waves and the rest in the perpendicular velocity of the particles of the beam, which is called the pitch-angle scattering. This section presents some main results of the linear theory as well as qualitative explanations of the processes involved in the instability.

2.6.1 Linear theory

Linear theory uses the Vlasov equation with the first-order perturbation method to calculate the dispersion relation (relationship between the complex frequency ω (including the real frequency and the growth-rate) and the real wave number k of the produced waves) for the generated waves. It is valid for small perturbations and shows that the initial perturbation grows at a rate that depends on the wave vector $\gamma(k)$ (see section 2.7 for more details), as well as the presence of a maximum in the growth rate γ_{max}, associated with a specific value of the wave vector k_{max}. More details about linear theory can be found in section 2.7.

We shall now focus on the current status of research of ion/ion-driven magnetic streaming instability with propagation parallel to the magnetic field, as it has been shown that they are the fastest growing (see Wang and Lin 2003). Linear theory (Gary 1991) has shown that there are essentially three different modes, with different polarization and corresponding to different, unstable magnetosonic waves. There are two ion-cyclotron resonant modes, with right-hand and left-hand polarization, and one non-resonant mode which is right-hand polarized, but counter-propagating with respect to the driving beam direction. Both resonant modes and the non-resonant mode are electromagnetic in nature, and only occur in the presence of a magnetic field. Each of these modes originate from a distinct normal mode that is found when the beam has no drift velocity.

Here we will present the two different kind of modes that are generated by the magnetic streaming instability and appear in the linear theory. A current-driven picture for both resonant and non-resonant modes was proposed by Schure et al. 2012, where both

mechanisms are driven by the Lorentz force $\mathbf{j} \times \mathbf{B}$ induced by the beam, which first-order component writes:

$$\mathbf{j}_1 \times \mathbf{B}_0 + \mathbf{j}_0 \times \mathbf{B}_1 \tag{2.8}$$

The first term is at the origin of the two resonant modes, the second is at the origin of the non-resonant mode.

2.6.2 Resonant modes

The resonant mode, driven by the component $\mathbf{j}_1 \times \mathbf{B}_0$ of the Lorentz force, occurs when a sufficient number of particles resonate with the waves, fulfilling the resonance condition:

$$\omega - k_{\parallel} v_{\parallel} \pm \Omega_C = 0 \tag{2.9}$$

where ω and $k_{\parallel}$ are the frequency and wave number parallel to the magnetic field of the wave, $v_{\parallel 1}$ the parallel component of the resonating particle and $\Omega_C = qB/m$ the cyclotron frequency of the particle of mass m and charge q. The $\pm$ sign depends on the polarization of the wave and shows the presence of two different modes, oppositely polarized, that will be investigated in the following chapters. $\omega - kv_{\parallel}$ is the frequency of the wave as seen by the particle considering the Doppler effect, and when it is equal to the particle cyclotron frequency, the particle always experiences the same electromagnetic field and the resonance takes place. This is illustrated in figure 2.2, representing the motion of a particle (red) around a magnetic field line (green) following the electromagnetic field in the frame of a wave (blue). Tsurutani and Lakhina 1997 give a more general resonance condition:

$$\omega - k_{\parallel} v_{\parallel} + n\Omega_C = 0 \tag{2.10}$$

with n a positive or negative integer. The case $n = 0$ corresponds to the Landau resonance and the cases $n = 1$ and $n = -1$ are respectively the right and left fundamental resonance conditions that we will consider in this paper. The right-hand resonant mode ($n = 1$) has been widely studied and is believed to be responsible for the waves observed in the solar wind and mentioned in section 2.2.1 (see Winske and Leroy 1984)

2.6.3 Non-resonant mode

The non-resonant mode, contrary to the resonant modes, does not require a resonance condition to be fulfilled. It was referred by Gary 1991 and Winske and Leroy 1984 as "firehose-like", which happens when a strong temperature anisotropy along a magnetic field $T_{\parallel}/T_{\perp} > 1$, with a parallel pressure exceeding the contributions of the perpendicular and the magnetic pressures $\beta_{\parallel} > 1$. In the case of the streaming instability, they believed that the role of the pressure was played by the bulk pressure of the beam, associated with its mean velocity.

According to Malovichko, Voitenko, and De Keyser 2014, this instability actually has a current-driven origin which was not identified at the time by Winske and Leroy 1984 and it is identical to the instability described by Bell (Bell 2004). As shown in figure 2.3 (taken from Zirakashvili, Ptuskin, and Völk 2008), the driving force is $\mathbf{j}_0 \times \mathbf{B}_1$ (in red),

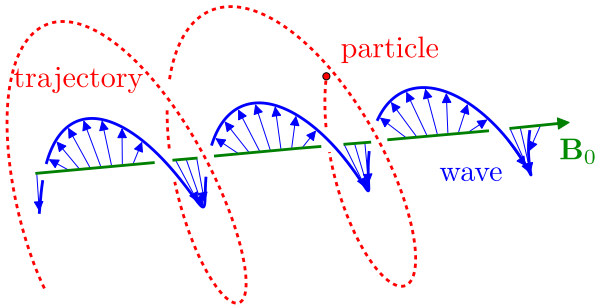

Figure 2.2: Scheme of the resonant mode. The particle trajectory (red) around the magnetic field (green) follows the polarized electromagnetic field of the waves (blue).

which acts on the beam-induced current, and the reaction to this force (blue) increases the magnetic perturbation, creating a feedback that enhances the driving force. This mode does not require an ion-cyclotron resonance to take place. It was in fact initially studied within a fluid approach in Bell 2004, and only later re-derived within a fully kinetic description by Amato and Blasi 2009.

2.7 Analytical results

To study analytically the development of the instability we use the linear theory from the Vlasov equation, which applies while the perturbation is still relatively small (in the first moments of its development). In this section we present the main equations and results as well as the underlying hypothesis. The detailed development of these equations can be found in Montgomery et al. 1976 (original development), Gary 1991 (review of previous theoretical works) and Gary 1993 (book that summarizes the linear developments of most of the streaming configurations).

2.7.1 Dispersion relation in the general case

In heliospheric plasma, Gary 1991 focused the linear development of the Vlasov equations for a collisionless magnetized plasmas. The Vlasov equation then writes:

$$\frac{\partial f}{\partial t} + \mathbf{v} \cdot \frac{\partial f}{\partial \mathbf{x}} + \frac{q}{m} (\mathbf{E} + \mathbf{v} \times \mathbf{B}) \cdot \frac{\partial f}{\partial \mathbf{v}} = 0 \tag{2.11}$$

with $f = f(\mathbf{x}, \mathbf{v}, t)$ the particle distribution function. For a homogeneous plasma, the dependence in space vanishes ($f = f(\mathbf{v}, t)$). Furthermore, the plasma we consider is gyrotrop, which means that the 2 directions in the perpendicular plan are equivalent. In such a case, the distribution function only depends on the parallel and perpendicular component of the velocity $f(v_\parallel, v_\perp, t)$. On the distribution function we apply the perturbation theory, considering the distribution function to be $f(\mathbf{x}, \mathbf{v}, t) = f_0(v_\parallel, v_\perp) + f_1(\mathbf{x}, \mathbf{v}, t)$ with $f_1 \ll f_0$, f_0 being the equilibrium distribution function, that does not depend on time nor

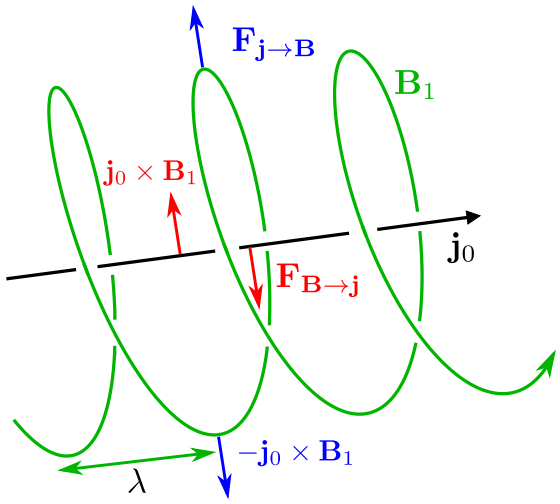

Figure 2.3: Scheme for the non-resonant mode. The perturbed magnetic field (green) acts on the current with the Lorentz force (red) and there is a reaction on the background that amplifies the waves (red).

space and f_1 the perturbation. The perturbation is of the form

$$f_1(x,v,t) = f_1(v)e^{\imath(\mathbf{k}.\mathbf{x}-\omega t)}$$

with $\omega = \omega_r + \imath\gamma$, ω_r being the frequency of the wave and γ its growth (or damping) rate. When $\gamma > 0$, the modes is unstable ($f_1 \propto e^{\imath(\mathbf{k}.\mathbf{x}-(\omega_r+\imath|\gamma|)t)} = e^{\gamma t}e^{\imath(\mathbf{k}.\mathbf{x}-\omega_r t)}$), and when $\gamma < 0$, the modes is damped. The general solution then writes:

$$\omega^2 - k^2c^2 - k^2c^2\sum_s \frac{\omega_{p,s}^2}{2k^2c^2n_s}\int v_\perp \left(k_\parallel v_\perp \frac{\partial f_{s,0}}{\partial v_\parallel} + \left(\omega - k_\parallel v_\parallel\right)\frac{\partial f_{s,0}}{\partial v_\perp}\right)\left(k_\parallel v_\parallel - \omega \mp \Omega_{C,s}\right)^{-1} = 0 \tag{2.12}$$

where the sum is over all species. This expression can be simplified by considering Maxwellian equilibrium distribution functions. Such an assumption enables a simpler study of the dispersive properties of our system. Using such distributions for f_0:

$$f_0(v_\parallel, v_\perp) = \frac{n_0}{(2\pi v_T^2)^{3/2}}\exp\left[-\frac{m(v_\parallel - V_b)^2}{2k_BT_\parallel} - \frac{mv_\perp^2}{2k_BT_\perp}\right] \tag{2.13}$$

Here $k_BT = mv_T^2$ is the thermal energy, and $T_\parallel$ and $T_\perp$ are the temperatures parallel and perpendicular to the magnetic field. Considering only electromagnetic modes propagating parallel to the initial magnetic field $\mathbf{k} \parallel \mathbf{B}_0$ we get the dispersion relation:

$$1 - \left(\frac{kc}{\omega}\right)^2 + \sum_s \left(\frac{\omega_{p,s}}{\omega}\right)^2 \zeta_s Z\left(\zeta_s^\pm\right) = 0 \tag{2.14}$$

where the sum is over all the species and $\omega_{p,s}$ the plasma frequency. ζ, $\zeta^{\pm}$ and Z (the plasma dispersion function or *Fried and Conte* function, Fried and Conte 1961) are defined as:

$$\zeta_s = \frac{\omega - kV_s}{kv_{T,s}} \tag{2.15}$$

$$\zeta_s^{\pm} = \frac{\omega - kV_s \pm \Omega_{C,s}}{kv_{T,s}} \tag{2.16}$$

$$Z(\zeta) = \pi^{-1/2} \int_{-\infty}^{\infty} \frac{e^{-t^2}}{t-\zeta} dt = \imath\sqrt{\pi} e^{-\zeta^2} \mathrm{erfc}(-\imath\zeta) \tag{2.17}$$

where $\Omega_{C,s}$ is the cyclotron frequency, ω and k are the frequency and wave vector of the wave, V_s and $v_{T,s}$ are the fluid and thermal velocities of the population s. The $\pm$ sign depends on the helicity of the perturbation, meaning the sense of rotation of the field in space at a given time (contrary to the polarization which is the sense of rotation of the field in time at a given space, this difference will be discussed in more details in chapter 4. In this case, the $+$ sign being positive helicity (left rotation) and $-$ being for the negative helicity (right rotation).

We consider three populations: the main plasma m, the beam b and the electrons e, with $V_e = 0$ (frame of the electrons). We focus on low frequency modes (below the proton gyrofrequency). At these frequencies, electrons are so fast they can be considered to move instantaneously to follow the evolution of the ions. We get the dispersion relation:

$$1 - \left(\frac{kc}{\omega}\right)^2 + \left(\frac{\omega_{p,m}}{\omega}\right)^2 \zeta_m Z\left(\zeta_m^{\pm}\right) + \left(\frac{\omega_{p,b}}{\omega}\right)^2 \zeta_b Z\left(\zeta_b^{\pm}\right) + \left(\frac{\omega_{p,e}}{\omega}\right)^2 \frac{\omega}{kv_{T,e}} Z\left(\zeta_e^{\pm}\right) = 0 \tag{2.18}$$

In order to solve equation 2.18 numerically, we developed a code that uses a complex solver (in a python library) to find the roots of this equation for a given value of k. This gives an approximation of the complex value of ω, and iterating this process for a number of values of k gives the ω and γ values as a function of k. Figure 2.4 shows the growth rate γ represented in red and the real frequency in blue, using this code. Ω_C is the proton cyclotron frequency and c/ω_p is the proton inertial length. The growth rate shows a maximum γ_{max} at the value k_{max}, which is the fastest growing mode that we are the most likely to observe in a simulation or in an experiment. However, there is a range of k that is unstable ($\gamma > 0$), which extends from $k = 0$ to $k\ c/\omega_p \approx 1.7$ (ω_p is the proton plasma frequency and c the speed of light) and this range gives the limit values of the length and resolution of the spatial domain for the simulation so we can observe these waves. For the negative part of the graph and for wave numbers above this range ($k\ c/\omega_p > 1.7$), the waves are stable. The graph can be separated in two domains, the domain with $k > 0$ corresponding to waves that propagate in the same direction as the beam and with $k < 0$ for the waves propagating against the beam. Here the waves propagate in the positive direction, and since the equation was solved for the left helicity ($+$ sign in equation 2.18), we can conclude that the observed mode is the right-hand resonant mode discussed in 2.6.2. Around $k\ c/\omega_p \approx 0.15$, the real frequency curve shows a local maximum, that is

actually the mark of a splitting of this curve into two branches, of which only one is shown here but other graphs in the following parts will show both of them.

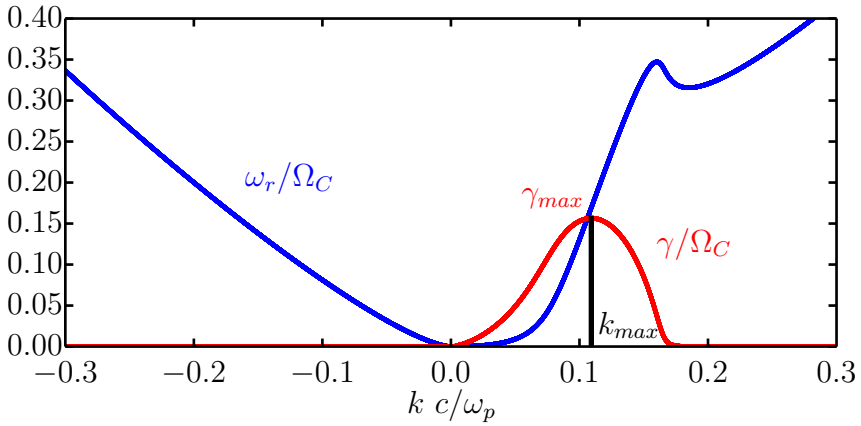

Figure 2.4: A dispersion graph ($\omega(k)$) for the conditions $f = n_b/n_m = 0.01$, $V_b = 10V_A$ and $v_{t,m} = v_{T,b} = V_A$ (which gives a plasma β of ≈ 2 and can be directly compared to previous works), with the real wave frequency ω_r in blue and the growth rate γ in red. It is a case we will use in the next chapters. The Larmor radius of the beam particle is $\rho_L = 2\ c/\omega_p$

2.7.2 Cold case

When dealing with cold plasmas, $v_{T,j} \to 0$ (the thermal velocity is small compared to the Alfvén speed) and we have the limit for the previous expressions:

$$v_{T,s} \to 0 \Rightarrow \zeta_s^{\pm} = \frac{\omega - kV_s \pm \Omega_{C,s}}{kv_{T,s}} \to \infty \tag{2.19}$$

The limit for the plasma dispersion function for large ζ with $\zeta = x + \imath y$ and $x > 0$:

$$\lim_{\zeta\to\infty} Z(\zeta) \approx \imath\sqrt{\pi}\sigma e^{-\zeta^2} - \zeta^{-1}\left[1 + \frac{1}{2\zeta^2} + \cdots\right] \tag{2.20}$$

where $\sigma = 0, 1, 2$, depending on the sign of the imaginary part of ζ. Considering the three populations, given that $V_e = 0$ (we are in the frame of the electrons), $m_p = 1836m_e$ and $\omega \ll \Omega_{C,e}$, this gives the dispersion relation in the cold plasma limit:

$$\omega^2 - k^2c^2 - \frac{\omega_{p,m}^2(\omega - kV_m)}{\omega - kV_m + \Omega_m} - \frac{\omega_{p,b}^2(\omega - kV_b)}{\omega - kV_b + \Omega_b} + \frac{n_e e}{\varepsilon_0 B}\omega = 0 \tag{2.21}$$

Equation 2.21 can be solved as well, and we can compare this solution to the one given by the general equation 2.18 with very low temperatures. Figure 2.5 **(a)** shows the same as in figure 2.4 with thermal velocities of about $10^5 V_A$. We can observe at first that the maximum growth rate in the cold case, which is about $\gamma_{max} \approx 0.17\Omega_C$ is higher than for figure 2.4 (that had thermal velocity of $v_T \approx V_A$) which is around $\gamma_{max} \approx 0.15\Omega_C$, this

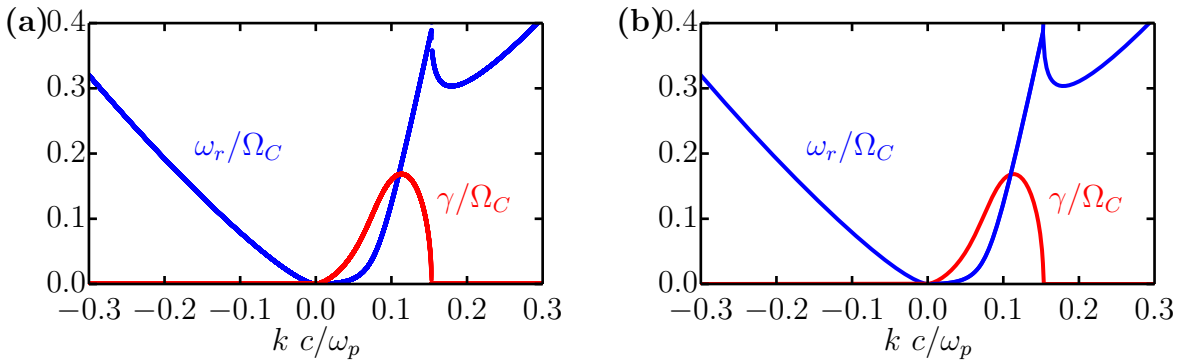

Figure 2.5: Dispersion graph ($\omega(k)$) for the conditions $f = 0.01$ and $V_b = 10V_A$, with the real wave frequency ω_r in blue and the growth rate γ in red. **(a)** was obtained solving equation 2.18 with very low temperatures and **(b)** solving equation 2.21.

effect will be addressed in chapter 4. Figure 2.5 **(b)** plots the solution of equation 2.21, and we can see that both solutions are very close, and we use the same equation to plot figure 2.6, which shows a different situation, with a density ratio (noted f) $f = n_b/n_m = 0.1$ and $V_b = 10V_A$, another case we will use in the following chapters.

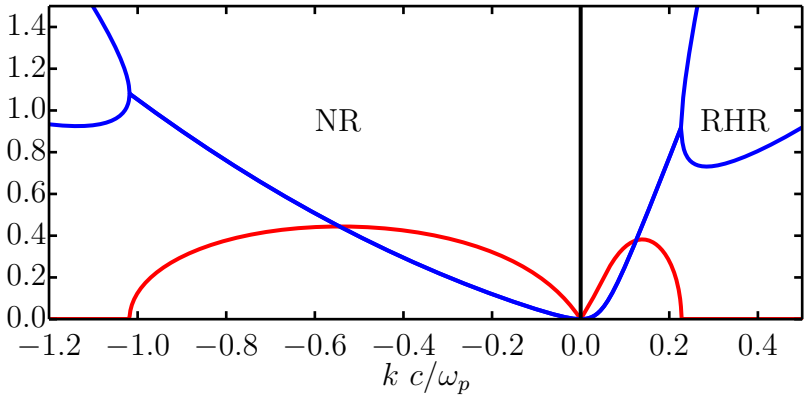

Figure 2.6: A dispersion graph ($\omega(k)$) for the conditions $f = 0.1$ and $V_b = 10V_A$ in the cold plasma approximations (equation 2.21), with the real wave frequency ω_r in blue and the growth rate γ in red. It is a case we will use in the next chapters.

We can identify the presence of two different modes in the negative (left) and positive (right) part of the dispersion graph, both having approximately the same γ_{max}. Both modes can thus coexist and be observed in the same conditions, producing different kind of waves. These mode are identified as:

- $k > 0$: the right-hand resonant modes (RHR), that will be treated in 4.2.2 and that is also the one mode we see in figure 2.4. The waves travel in the same direction as the beam and right-hand polarized.

- $k < 0$: the non-resonant mode (NR), will be addressed in section 4.3. The waves travel in the opposite direction of the beam and are right-hand polarized as well.

The differences between these modes will be investigated in more details in chapter 4. We have $\gamma_{max}^{(NR)} = 0.44\Omega_C$ for the NR mode and $\gamma_{max}^{(RHR)} = 0.38\Omega_C$ for the RHR mode, and the corresponding wave numbers $k_{max}^{(NR)}\ c/\omega_p = -0.54$ and $k_{max}^{(RHR)}\ c/\omega_p = 0.14$. Solving equation 2.21 does not allow to find the left-hand resonant mode, as this instability only appears when the beam has a very high temperature, therefore is not included in the hypothesis used to derive the equation.

2.8 Heavy elements

All previously shown dispersion relations are for hydrogen plasmas (with $m_m = m_b = m_p$ and $q_m = q_b = e$), but in some cases, the plasma can be of more complex composition (interstellar medium, laboratory experiments) and effects due to a higher mass of one of the populations must be taken into account. In this section we are then interested in the influence of these parameters on the dispersion relation, using the same method as in section 2.7.2 and varying the species mass to study the effects on γ_{max} and k_{max}. A theoretical study has been done in Wang, Gary, and Liewer 1999, who studied the effects of the mass of the beam ions on the RHR and the NR modes, and showed the presence of an heavy-ion/proton instability. We use a situation similar to the one presented in figure 2.6, with a coexistence of the right-hand resonant mode and the non-resonant mode at approximately the same γ_{max} ($f = 0.1$ and $V_b = 10V_A$), and vary either the mass of the main plasma m_m while keeping $m_b = m_p$ (m_p being the proton mass) or the mass of the beam m_b while keeping $m_m = m_p$.

Figure 2.7 **(a)** shows in red the maximum growth rate for the RHR ($\gamma_{max}^{(RHR)}$, in solid line) and non-resonant ($\gamma_{max}^{(NR)}$ in dashed line) modes and the associated k_{max} in blue as a function of the main mass m_m/m_p. We can observe that, when increasing the mass of the main plasma, the non-resonant mode become much less important while the right-hand resonant mode remains approximately at the same level. The wavelength, however, stays constant for the NR mode and decreases a bit for the RHR mode. This may be linked to the component of the driving force involved in each of these instabilities: increasing the magnetic perturbation is more difficult with a heavier background as the ions have more inertia, and since the driving force of the NR mode depends on the amplitude of these perturbations for NR mode, this makes it more difficult to grow when increasing m_m. On the contrary, the main mass has no such effect on the current perturbation, and therefore does not constraint the RHR mode in the same way.

On the other hand, figure 2.7 **(b)** plots the evolutions of the maximum growth rate for the RHR ($\gamma_{max}^{(RHR)}$, in solid line) and non-resonant ($\gamma_{max}^{(NR)}$ in dashed line) modes and the associated k_{max} as a function of the beam mass m_b/m_p and shows a strong dependence of the RHR mode that decreases strongly when the beam gets heavier while the NR mode is barely affected, which is consistent with the result found in Winske and Quest 1986 for the same case. We can see that the RHR mode is impacted, while the NR instability remains almost unchanged. Again, thinking in term of inertia, this can be explained in

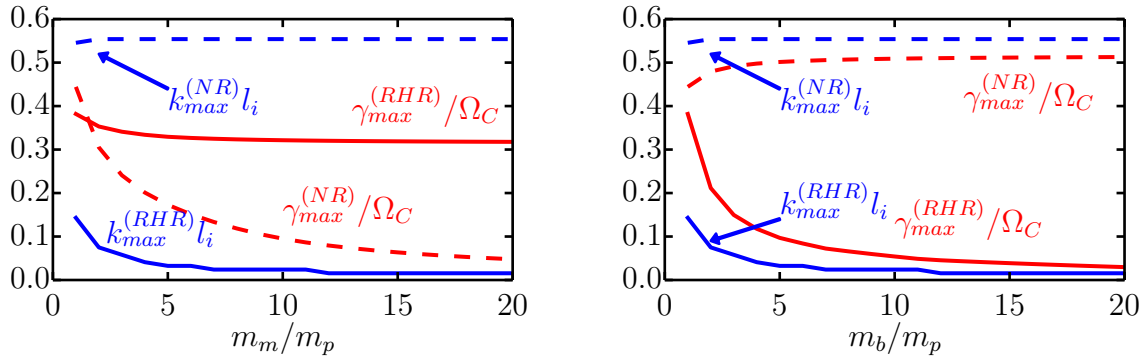

Figure 2.7: Evolution of the maximum growth rate γ_{max} (red) and the associated wavenumber k_{max} (blue) for the RHR (plain) and the NR (dashed) modes with the mass of the main plasma m_m for panel **(a)** and the mass of the beam for panel m_b. Here $l_i = c/\omega_p$ is the proton inertial length.

the fact that the Lorentz force has more difficulties to accelerate heavier ions of the beam, thus reducing the growth of the current perturbation. As the resonant mode rely on this first-order component of the current, these modes are less likely to develop in the presence of a heavier beam.

2.9 Numerical model

Although instabilities can be studied analytically within the framework of linear theory, which applies when the perturbation from an equilibrium state is relatively small in amplitude, time-dependent numerical simulations are necessary to follow the instability from its onset into the non-linear phases, and to study its saturation mechanisms. Such numerical simulations allows us to take advantage of the massive computational power available with the computers to solve the equations of the model beyond the linear stage. As the very heart of the instability lies in the form of the distribution function, as in the resonant modes where we need to treat wave-particle interactions, a MHD (that consider the plasma as a single fluid, including both ions and electrons) model would not be able to capture the physics involved in this phenomenon. We thus need a kinetic description. For the instabilities involving electron time and length scales, a full PIC model (that treats both ions and electrons with a kinetic model) is needed but in the case of the magnetic streaming instability, we are looking at scales of the order of the ionic gyrofrequency and inertial length of the ions. Therefore we can consider the electrons as a massless fluid since their mobility can then be considered as infinite, so the calculation time will be shorter, and only the ions will get a kinetic description and be modelled as macroparticles. The model we use is described in section 3.

We have seen in this chapter that there is a wide variety of streaming instabilities in plasmas, and discussed few of them, like some electrostatic, electromagnetic or anisotropy instabilities. We have also seen that these kind of instabilities are found in many places

in the universe in a broad diversity of physical conditions. Focusing on a particular case, we proposed a physical explanation for the phenomena occurring in this instability, and presented some main analytical results related to it. In the following sections, we will investigate in more details the mechanisms of this instability in the collisionless case (chapter 4) and collisional case (chapter 5) using the model presented in chapter 3.

Bibliography

Gary, S. P. (1993). *Theory of Space Plasma Microinstabilities*, p. 193 (cit. on pp. 8, 10, 18).

Marcowith, A. et al. (2016). "The microphysics of collisionless shock waves". In: *Reports on Progress in Physics* 79.4, 046901, p. 046901 (cit. on p. 8).

Cairns, I. H. and P. A. Robinson (1999). "Strong Evidence for Stochastic Growth of Langmuir-like Waves in Earth's Foreshock". In: *Physical Review Letters* 82, pp. 3066–3069 (cit. on p. 9).

Tsurutani, B. T. and G. S. Lakhina (1997). "Some basic concepts of wave-particle interactions in collisionless plasmas". In: *Reviews of Geophysics* 35, pp. 491–501 (cit. on pp. 9, 17).

Feldman, W. C. et al. (1973). "Double ion streams in the solar wind". In: *Journal of Geophysics Research* 78, p. 2017 (cit. on pp. 9, 11).

Sydorenko, D. et al. (2007). "Effects of non-Maxwellian electron velocity distribution function on two-stream instability in low-pressure discharges". In: *Physics of Plasmas* 14.1, 013508, p. 013508 (cit. on p. 9).

Weibel, E. S. (1959). "Spontaneously Growing Transverse Waves in a Plasma Due to an Anisotropic Velocity Distribution". In: *Physical Review Letters* 2, pp. 83–84 (cit. on p. 10).

Medvedev, M. V. et al. (2004). "Generation of Magnetic Fields in Cosmological Shocks". In: *Journal of Korean Astronomical Society* 37, pp. 533–541 (cit. on p. 10).

Cottrill, L. A. et al. (2008). "Kinetic and collisional effects on the linear evolution of fast ignition relevant beam instabilities". In: *Physics of Plasmas* 15.8, 082108, p. 082108 (cit. on pp. 10, 15).

Fairfield, D. H. (1969). "Bow shock associated waves observed in the far upstream interplanetary medium". In: *Journal of Geophysics Research* 74, p. 3541 (cit. on p. 10).

Russell, C. T., D. D. Childers, and P. J. Coleman Jr. (1971). "Ogo 5 observations of upstream waves in the interplanetary medium: Discrete wave packets". In: *Journal of Geophysics Research* 76, p. 845 (cit. on p. 10).

Hoppe, M. M. et al. (1981). "Upstream hydromagnetic waves and their association with backstreaming ion populations - ISEE 1 and 2 observations". In: *Journal of Geophysics Research* 86, pp. 4471–4492 (cit. on p. 11).

Tsurutani, B. T. et al. (1987). "Magnetohydrodynamic Waves Detected by Ice at Distances Equal-To 280,000,000-KILOMETERS from Comet p/ Halley - Cometary or Solar Wind Origin". In: *Astronomy and Astrophysics* 187, p. 97 (cit. on p. 11).

Bonifazi, C. et al. (1980). "Backstreaming ions outside the earth's bow shock and their interaction with the solar wind". In: *Journal of Geophysics Research* 85, pp. 3461–3472 (cit. on p. 11).

Winske, D. and M. M. Leroy (1984). "Diffuse ions produced by electromagnetic ion beam instabilities". In: *Journal of Geophysics Research* 89, pp. 2673–2688 (cit. on pp. 11, 17).

Onsager, T. G., D. Winske, and M. F. Thomsen (1991). "Interaction of a finite-length ion beam with a background plasma - Reflected ions at the quasi-parallel bow shock". In: *Journal of Geophysics Research* 96, pp. 1775–1788 (cit. on p. 11).

Mukai, T. et al. (1986). "Ion dynamics and distribution around Comet Halley - Suisei observation". In: *Geophysical Research Letters* 13, pp. 829–832 (cit. on p. 11).

Gary, S. P. and C. D. Madland (1988). "Electromagnetic ion instabilities in a cometary environment". In: *Journal of Geophysics Research* 93, pp. 235–241 (cit. on p. 11).

Yoon, P. H. (1990). "Kinetic instability associated with spherical shell distribution of cometary pickup ions". In: *Geophysics Research Letters* 17, pp. 1033–1036 (cit. on p. 11).

Wang, X. Y. and Y. Lin (2003). "Generation of nonlinear Alfvén and magnetosonic waves by beam-plasma interaction". In: *Physics of Plasmas* 10, pp. 3528–3538 (cit. on pp. 11, 16).

Ferrière, K. M. (2001). "The interstellar environment of our galaxy". In: *Reviews of Modern Physics* 73, pp. 1031–1066 (cit. on pp. 12, 15).

Hall, J. S. (1949). "Observations of the Polarized Light from Stars". In: *Science* 109, pp. 166–167 (cit. on p. 12).

Castellina, A. and F. Donato (2011). "Astrophysics of Galactic charged cosmic rays". In: *ArXiv e-prints* (cit. on p. 12).

Parizot, E. (2014). "Cosmic Ray Origin: Lessons from Ultra-High-Energy Cosmic Rays and the Galactic/Extragalactic Transition". In: *Nuclear Physics B Proceedings Supplements* 256, pp. 197–212 (cit. on p. 12).

Blandford, R., P. Simeon, and Y. Yuan (2014). "Cosmic Ray Origins: An Introduction". In: *ArXiv e-prints* (cit. on p. 12).

Zweibel, E. G. (2013). "The microphysics and macrophysics of cosmic rays". In: *Physics of Plasmas* 20.5, p. 055501 (cit. on pp. 12, 13).

Marcowith, A. (2014). "Cosmic Ray propagation in the interstellar medium". In: *Frontiers of Fundamental Physics 14 (FFP14)*, p. 56 (cit. on p. 12).

Gargaté, L. and A. Spitkovsky (2012). "Ion Acceleration in Non-relativistic Astrophysical Shocks". In: *Astrophysical Journal* 744, 67, p. 67 (cit. on p. 14).

Bell, A. R. (2004). "Turbulent amplification of magnetic field and diffusive shock acceleration of cosmic rays". In: *Monthly Notices of the RAS* 353, pp. 550–558 (cit. on pp. 14, 17, 18).

Bell, A. R. et al. (2013). "Cosmic-ray acceleration and escape from supernova remnants". In: *Monthly Notices of the RAS* 431, pp. 415–429 (cit. on p. 14).

Stroman, T., M. Pohl, and J. Niemiec (2009). "Kinetic Simulations of Turbulent Magnetic-Field Growth by Streaming Cosmic Rays". In: *Astrophysical Journal* 706, pp. 38–44 (cit. on p. 14).

Padoan, P. and J. Scalo (2005). "Confinement-driven Spatial Variations in the Cosmic-Ray Flux". In: *Astrophysical Journal, Letters* 624, pp. L97–L100 (cit. on p. 14).
Amato, E. (2011). "The streaming instability: a review ". In: *Mem. Societa Astronomica Italiana* 82, p. 806 (cit. on p. 14).
Padovani, M., D. Galli, and A. E. Glassgold (2009). "Cosmic-ray ionization of molecular clouds". In: *Astronomy and Astrophysics* 501, pp. 619–631 (cit. on p. 14).
Padovani, M., P. Hennebelle, and D. Galli (2014). "Cosmic rays as regulators of molecular cloud properties". In: *ArXiv e-prints* (cit. on p. 14).
Morlino, G. and S. Gabici (2015). "Cosmic ray penetration in diffuse clouds". In: *Monthly Notice of the Royal Astronomical Society* 451, pp. L100–L104 (cit. on p. 14).
Padovani, M. and D. Galli (2013). "Cosmic-Ray Propagation in Molecular Clouds". In: *Cosmic Rays in Star-Forming Environments*. Ed. by D. F. Torres and O. Reimer. Vol. 34. Advances in Solid State Physics, p. 61 (cit. on p. 14).
Bykov, A. M. et al. (2013). "Microphysics of Cosmic Ray Driven Plasma Instabilities". In: *Space Science Reviews* 178, pp. 201–232 (cit. on p. 14).
Dawson, J. M. (1964). "On the Production of Plasma by Giant Pulse Lasers". In: *Physics of Fluids* 7, pp. 981–987 (cit. on p. 15).
Kuramitsu, Y. et al. (2011). "Model experiment of cosmic ray acceleration due to an incoherent wakefield induced by an intense laser pulse". In: *Physics of Plasmas* 18.1, p. 010701 (cit. on p. 15).
Fox, W. et al. (2013). "Filamentation Instability of Counterstreaming Laser-Driven Plasmas". In: *Physical Review Letters* 111.22, 225002, p. 225002 (cit. on p. 15).
Weidl, M. S. et al. (2016). "Hybrid simulations of a parallel collisionless shock in the large plasma device". In: *Physics of Plasmas* 23.12, 122102, p. 122102 (cit. on p. 15).
Mamun, A. A. and P. K. Shukla (2000). "Streaming instabilities in a collisional dusty plasma". In: *Physics of Plasmas* 7, pp. 4412–4417 (cit. on p. 15).
Lazar, M. et al. (2008). "Counterstreaming magnetized plasmas with kappa distributions - I. Parallel wave propagation". In: *Monthly Notice of the Royal Astronomical Society* 390, pp. 168–174 (cit. on p. 15).
Gary, S. P. (1991). "Electromagnetic ion/ion instabilities and their consequences in space plasmas - A review". In: *Space Science Reviews* 56, pp. 373–415 (cit. on pp. 16–18).
Schure, K. M. et al. (2012). "Diffusive Shock Acceleration and Magnetic Field Amplification". In: *Space Science Reviews* 173, pp. 491–519 (cit. on p. 16).
Malovichko, P., Y. Voitenko, and J. De Keyser (2014). "Oblique Alfvén Instabilities Driven by Compensated Currents". In: *Astrophysical Journal* 780, 175, p. 175 (cit. on p. 17).
Zirakashvili, V. N., V. S. Ptuskin, and H. J. Völk (2008). "Modeling Bell's Nonresonant Cosmic-Ray Instability". In: *Astrophysical Journal* 678, pp. 255–261 (cit. on p. 17).
Amato, E. and P. Blasi (2009). "A kinetic approach to cosmic-ray-induced streaming instability at supernova shocks". In: *Monthly Notices of the RAS* 392, pp. 1591–1600 (cit. on p. 18).
Montgomery, M. D. et al. (1976). "Electromagnetic instabilities driven by unequal proton beams in the solar wind". In: *Journal of Geophysics Research* 81, pp. 2743–2749 (cit. on p. 18).
Fried, B. D. and S. D. Conte (1961). *The Plasma Dispersion Function* (cit. on p. 20).

Wang, J. J., S. P. Gary, and P. C. Liewer (1999). “Electromagnetic heavy-ion/proton instabilities”. In: *Journal of Geophysics Research* 104, pp. 24807–24818 (cit. on p. 23).

Winske, D. and K. B. Quest (1986). “Electromagnetic ion beam instabilities - Comparison of oneand two-dimensional simulations”. In: *Journal of Geophysics Research* 91, pp. 8789–8797 (cit. on p. 23).

Chapter 3

Presentation of the numerical model

> I have merely shown that mathematical analysis is possible; I have not shown it to be practical.
>
> Hari Seldon - Prelude to Foundation (1988), Isaac Asimov.

Contents

Linear theory provides no information on the saturation while quasi-linear theory provides some information on the saturation but none on the non-linear behaviours of the instability. However, these non-linear behaviours are important to understand the complete evolution of the instability. To move beyond the approximations of linear and quasi-linear theories, it is however necessary to solve the full time-dependent Vlasov equation numerically, without the restrictions of linear theory, such as small perturbations, early times, etc.

In this chapter, we present the model we use for the simulations of the magnetic streaming instability and the inclusion of ion-ion collisions. Section 3.1 presents a basic overview of different plasmas models and their specificities, section 3.2 will present in details the model we use in the present work, section 3.3 presents some elements of collisions in plasmas in analytical calculations while section 3.4 gives a more detailed approach to the physics of Coulomb collisions. In section 3.5 we present the collision module that was implemented in the numerical code, while section 3.6 presents some benchmarks that were made to test this collision module. Finally section 3.8 present the numerical setup we use throughout our study.

3.1 Plasma models

The complexity of many plasma processes makes it difficult to describe them using only analytical calculations. This largely motivates the use of numerical simulations which take advantage of the computational power available nowadays on the many, easily accessible supercomputers. Depending on the time and length scales we are considering, and to be as efficient as possible in the description of a given phenomenon, different kind of plasma models are at our disposal. For example, there is no need to use a full description of each particle interactions (N-body problem) when the timescales are such that the plasma are always in a Maxwellian form due to collisions between the particles. Instead one may be content to manipulate the macroscopic quantities that are the first moments of the distribution function, such as the density, the fluid velocity or the pressure of the plasma. In this section we present the the principal features of the main types of models for plasmas, starting with the kinetic approach, then moving on with the fluid models, and finally giving a description of hybrid models.

3.1.1 Kinetic models

The kinetic description for a plasma comes from the solution of the Vlasov equation. There are several ways to solve Vlasov equation numerically (equation 2.11). One of the most widely used methods is the Particle-In-Cell approach, which consists in solving the Vlasov equation for discrete parts of the distribution function, represented by so-called "macroparticles". The electromagnetic fields are then updated on the grid using the information inferred from the "macroparticle" position.

Macroparticles are computational particles that represent a large number of real particles. The position and velocity of this macroparticles are then the average position and velocity of an ensemble of real particles. In PIC methods, each macroparticle has a finite size analytically described by a shape factor (see e.g. Birdsall and Langdon 1991 or Lapenta 2012) . These "shape functions" are used to interpolate the density in any position in space $\mathbf{x}$ and velocity space $\mathbf{v}$ depending on the position and velocity of the macroparticle $\mathbf{x}_p$ and $\mathbf{v}_p$. The distribution function produced by a macroparticle is given by:

$$f_p(\mathbf{x},\mathbf{v},t) = N_p S_{\mathbf{x}}\left(\mathbf{x}-\mathbf{x}_p(t)\right) S_{\mathbf{v}}\left(\mathbf{v}-\mathbf{v}_p(t)\right) \tag{3.1}$$

where N_p is the number of real particles represented by a macroparticle and $S_{\mathbf{x}}$ and $S_{\mathbf{v}}$ are the shape functions in the real and velocity spaces. The total distribution function in the 6 dimensional space (3 for the real space and 3 for the velocity space) is thus the sum of all contribution of the macroparticles. The shape function in a given dimension can be of order 0 (rectangle function), order 1 (triangle function) or of higher orders.

The second and third terms of the Vlasov equation are used to solve the equations of motion (in our case, in the nonrelativistic regime) for the macroparticles with mass m and charge q:

$$m\frac{d\mathbf{v}_p}{dt} = q\left(\mathbf{E}+\mathbf{v}_p\times\mathbf{B}\right) \tag{3.2}$$

$$\frac{d\mathbf{x}_p}{dt} = \mathbf{v}_p \tag{3.3}$$

To calculate the electric and magnetic fields $\mathbf{E}$ and $\mathbf{B}$, PIC codes use Maxwell's equations:

$$\nabla\times\mathbf{E} = -\frac{\partial\mathbf{B}}{\partial t} \tag{3.4}$$

$$\nabla\times\mathbf{B} = \mu_0\varepsilon_0\frac{\partial\mathbf{E}}{\partial t}+\mu_0\mathbf{J} \tag{3.5}$$

$$\nabla\cdot\mathbf{E} = \frac{\rho}{\varepsilon_0} \tag{3.6}$$

$$\nabla\cdot\mathbf{B} = 0 \tag{3.7}$$

where ρ and $\mathbf{J}$ are the total charge density and current density on a grid, calculated from the macroparticles.

In full-PIC codes, both electrons and ions are described as macroparticles. However, as the electrons are much lighter than ions, their characteristic time-scales (e.g. $\Omega_{C,e}^{-1}$ or $\omega_{p,e}^{-1}$) are much smaller than those associated with the response of the ions. For large, multi-dimensional systems with hundreds of millions of particles, this can lead to prohibitive time-steps. To solve this problem, one approach in many PIC codes is to use an artificially low mass ratio for the ions and the electrons. For example, this ratio can be as low as $m_i/m_e \approx 100$, and still be tolerable to describe accurately many processes (see Birdsall and Langdon 1991).

While kinetic models have the advantage of providing an accurate description of the plasma, and obviously kinetic effects such as particle resonances, they remain computa-

tionally very time-consuming. In general they are limited to spatial and temporal scale not too large with respect to the Debye length and the inverse of the plasma frequency, which are well below those that can be afforded by fluid models.

3.1.2 Fluid models

When the description of a phenomenon does not require the kinetic description of the plasma, a fluid model is appropriate. It is usually interesting when the time scales of the study are large enough for the particles in a plasma to relax to a Maxwellian (through collisions or interactions with magnetic turbulence, for instance) at all time, but can also work for example with Lorentzian distribution. In a fluid model, only the real space is discretized and the fluid equations are solved on the grid at each timestep. This allows to disregard the motion of individual particles (or rather macroparticles in the case of a PIC code), and simulate very large domains in multi-dimensions.

The transition from a kinetic to a fluid description of a specie in a plasma comes from the reduction of its distribution function to its moments. The fluid variables are thus these moments for each species s. Usually the first three are used: the density n_s, the fluid velocity $\mathbf{V}_s$ and the pressure tensor $\mathbf{P}_s$. When considering several species (for example two species of ions and one specie of electrons), we can use a multi-fluid description, where each of the species are described as a different fluid. A particular case of multi-fluid model is the two-fluid, where the two species considered are the electrons and the ions. A variation of the two-fluid model is the widely used single fluid MHD model where all the plasma, electrons and ions, are treated as a single fluid. In the non-relativistic regime ($V/c \ll 1$ with V the typical velocity of the system), low-frequency limit ($\omega \ll \omega_{p,e}$ where $\omega_{p,e}$ is the plasma frequency) and under the assumption that the ion Larmor radius is negligible compared to the size of the system ($\rho_{L,s} \ll L$), the MHD model is then described by the following set of equations (see Krall and Trivelpiece 1973):

- the continuity equation:
$$\frac{\partial \rho_m}{\partial t} + \nabla \cdot \rho_m \mathbf{V} = 0 \tag{3.8}$$
with $\rho_m = n_e m_e + n_i m_i$ the total mass density and $\mathbf{V} = m_e \mathbf{V}_e + m_i \mathbf{V}_i / (m_e + m_i)$;
- the momentum transport:
$$\rho_m \left(\frac{\partial \mathbf{V}}{\partial t} + (\mathbf{V} \cdot \nabla) \mathbf{V} \right) = \mathbf{J} \times \mathbf{B} - \nabla p \tag{3.9}$$
with p the pressure of the plasma, reduced to a scalar under the assumption that the collision frequency between ions and electrons is high compared to the cyclotron frequency ($\nu_{ei} \gg \Omega_{C,i}$), and $\mathbf{J}$ the current density of the plasma. This reduction can also be done under the assumption that the typical length scales of the system are high compared to the ion Larmor radius;
- the electron equation of motion is replaced by the Ohm's law:
$$\mathbf{E} + \mathbf{V} \times \mathbf{B} = \eta \mathbf{J} \tag{3.10}$$

with η the resistivity reduced to a scalar for the same reason as the pressure;

- the Maxwell's equations for the electric and magnetic fields $\mathbf{E}$ and $\mathbf{B}$, neglecting the displacement current:

$$\nabla \times \mathbf{E} = -\frac{\partial \mathbf{B}}{\partial t} \tag{3.11}$$

$$\nabla \times \mathbf{B} = \mu_0 \mathbf{J} \tag{3.12}$$

Some variations of this set of equations can be found under different assumptions, usually by adding terms to the equations (for example, the Hall term in the Ohm's law). This set of equation needs a closure equation that usually relate the last and first moments (the pressure and the density). For instance, we can use the adiabatic fluid closure relation:

$$\frac{d}{dt}\left[p\rho_m^{-\gamma}\right] = 0 \tag{3.13}$$

with γ the adiabatic index. We can also use the isothermal fluid assumption:

$$\frac{d}{dt}\left[\frac{p}{\rho_m}\right] = 0 \tag{3.14}$$

3.1.3 Hybrid model

Hybrid models mix kinetic and fluid aspects within the same description of a plasma. Hybrid-PIC are a compromise between the precision of a fully kinetic model and the computational efficiency of a fluid description. In hybrid-PIC models the electrons are modeled as a massless fluid while the ions are treated with a kinetic description. Because the electrons have an infinite mobility, they move instantaneously over the characteristic timescales of the ions, which is of the order of the inverse of the ion gyro-frequency. Consequently, the high-frequency, small length scales associated with the electron are removed, and larger time-steps can be taken in the computations. Clearly processes such as the dissipation of energy at the electron scales or high frequency waves such as the electron Langmuir waves are not described by this model. This type of model is very popular in studying the magnetic streaming instability (see Winske and Quest 1986, Wang and Lin 2003), and it is the one we employ in the present study. The details of our model along with the equations are presented in section 3.2.

Another kind of hybrid model is given by coupling a MHD model to a kinetic description for one or more species. When the kinetic particles do not interact with the MHD fluid, we have the so-called "test particle" model. On the contrary, in MHD-PIC, the kinetic particle may interact directly with the fluid (for example via collisions) or couple to the background by generating electromagnetic fields. This type of model has been successfully used in describing the non-resonant mode of the magnetic streaming instability in the case of cosmic-ray acceleration in shocks (with a kinetic description of the cosmic rays and a MHD model for the background plasma, see Bai et al. 2015).

In this work, we use a hybrid code to simulate the interaction of a streaming beam of ions in a plasmas. The next section presents the hypothesis and equations of the model as well as the unit system we use.

3.2 Presentation of the numerical hybrid model

In this section we present the equations employed in the model, the assumptions made, as well as the setup we use for the simulations. As shown in previous works, the instability is essentially kinetic at the scales of the ions, and the use of a kinetic treatment for the ions, but not for the electrons, is well justified. In our hybrid-PIC model, the ions are treated as macroparticles within a PIC framework, and the electrons are treated as a massless fluid. The macroparticles (which we will also refer to as particles hereafter), which are discrete parts of the distribution function and represent a given density of real particles, have a shape function of order 1 (see Birdsall and Fuss 1969 and Lapenta 2012). Which means that their velocity and mass density are linearly interpolated to the grid points where the fields are evaluated. The code is called HECKLE, is fully 3D and MPI parallelized. Particle motions are integrated in time using a Boris pusher and a leap-frog scheme, and the electromagnetic fields are integrated using a predictor-corrector scheme (Harned 1982); the main algorithm is described in Winske and Quest 1986.

Macroparticles experience the classical equations of motion for particles of mass m and charge q:

$$m\frac{d\mathbf{v}_p}{dt} = q\left(\mathbf{E}+\mathbf{v}_p\times\mathbf{B}\right)+\mathbf{F}_{coll} \tag{3.15}$$

$$\frac{d\mathbf{x}_p}{dt} = \mathbf{v}_p \tag{3.16}$$

where $\mathbf{v}_p$ and $\mathbf{x}_p$ denote the particle velocities and position, $\mathbf{E}$ and $\mathbf{B}$ are the electric and magnetic fields, and $\mathbf{F}_{coll}$ is the force due to the collisions. Maxwell equations are used for the induced magnetic field and current density, and are simplified by neglecting the transverse component of the displacement current:

$$\frac{\partial\mathbf{B}}{\partial t} = -\nabla\times\mathbf{E} \tag{3.17}$$

$$\mu_0\mathbf{J} = \nabla\times\mathbf{B} \tag{3.18}$$

where $\mathbf{J}$ is the current density (transverse component). The electric field comes from an Ohm's law where the electrons inertia is neglected since the electrons are considered as a fluid:

$$\mathbf{E} = -\mathbf{V}_i\times\mathbf{B}+\frac{1}{qN_e}\left(\mathbf{J}\times\mathbf{B}-\nabla P_e\right)+\eta\mathbf{J} \tag{3.19}$$

In this expression V_i is the ion fluid velocity, P_e is the scalar electron pressure, N_e is the electron density, equal to the total ion density by imposing quasi-neutrality, and η the resistivity of the plasma. To calculate the electronic pressure, we use an isothermal

closure relation:

$$P_e = N_e k_B T_e \tag{3.20}$$

with T_e the constant and uniform electronic thermal energy.

We define n_0 and B_0 as the initial unperturbed uniform plasma density and magnetic field. The associated Alfvén velocity V_0, gyrofrequency Ω_0 and ion inertial length l_0 are given by:

$$V_0 = \frac{B_0}{\sqrt{\mu_0 n_0 m_p}} \tag{3.21}$$

$$\Omega_0 = \frac{eB_0}{m_p} \tag{3.22}$$

$$l_0 = \frac{V_0}{\Omega_0} = \sqrt{\frac{m_p}{\mu_0 n_0 e^2}} \tag{3.23}$$

where m_p is the proton mass and e the elementary charge

To model Coulomb collisions we use the algorithm developed by Takizuka and Abe 1977, which pairs macro-particles, within a given cell and at each time-step, to calculate the change of velocity via a Monte-Carlo method. The details of this method are given in section 3.5, along with the definition of several new quantities that are used in the calculation of the collisional scattering of macro-particles.

3.3 Collisions in analytical calculations

Plasmas are composed of ions and electrons, and in partially ionized plasmas they can also include neutral species. All these different populations can interact through collisions, which in general occur over very different timescales. Coulomb collisions between charged particle take place because of the microscopic electric force arising from the particle's charge. Collisions in partially ionized plasmas also include those between neutral atoms (or molecules) and ions and electrons; this is often the case in the cold interstellar medium.

Within the framework of kinetic theory, collisions in a plasma are modelled by a collision operator in Vlasov equation. For the distribution function of species a, Vlasov equation is:

$$\frac{\partial f_a}{\partial t} + \mathbf{v} \cdot \frac{\partial f_a}{\partial \mathbf{x}} + \frac{q}{m} (\mathbf{E} + \mathbf{v} \times \mathbf{B}) \cdot \frac{\partial f_a}{\partial \mathbf{v}} = C_a \tag{3.24}$$

The C_a collision operator gives the change in the distribution function of species a due to collisions, and is equal to zero in the collisionless case. The collision operator is the sum of the collisions acting on a given specie by all other species present in the plasma, that is Braginskii 1965:

$$C_a = \sum_b C_{ab}(f_a, f_b) \tag{3.25}$$

The sum is made over all species in the plasma (including a) and $C_{ab}(f_a, f_b)$ is the collision operator of the specie b on the specie a.

Works such as those of Cottrill et al. 2008 or Hao et al. 2009, looked at the effects of collisions on various instabilities using a Vlasov-Krook operator of the form:

$$C_a = -\nu\,(f_a - f_{a,0}) \tag{3.26}$$

with $f_{a,0}$ an equilibrium distribution (usually Maxwellian) of f_a and ν the Krook collision frequency, usually identified with the Coulomb collision frequency. This operator does not capture the full physics of Coulomb collisions and it is essentially a phenomenological operator, however it has the advantage of being much simpler to manipulate in calculations than the Landau operator that we will detail later. Nevertheless, this operator has the defect of not conserving explicitly the charge. Thus more sophisticated variations of this model were developed (see Bhatnagar, Gross, and Krook 1954). In Fried, Kaufman, and Sachs 1966, an operator that conserves explicitly the energy was developed and it was then used in Opher, Morales, and Leboeuf 2002 to calculate susceptibilities in plasmas.

Another collision operator is the Landau operator developed in Braginskii 1965 that we present in section 3.4. This operator considers Coulomb collisions and is much more difficult to manipulate in calculations than a Krook-like operator, hence the need of implementing it in self-consistent computer simulations. Once integrated the Landau operator takes the form:

$$C_{ab} = \frac{4\pi e_a^2 e_b^2 \Lambda}{2m_a^2}\frac{\partial}{\partial v_\alpha}\left(D_{b\alpha\beta}\frac{\partial f_a}{\partial v_\beta} - \frac{m_a}{m_b} f_a \frac{\partial}{\partial v_\beta} D_{b\alpha\beta}\right) \tag{3.27}$$

$$D_{b\alpha\beta} = \int v' f_b' \frac{u^2\delta_{\alpha\beta} - u_\alpha u_\beta}{u^3} d^3v' \tag{3.28}$$

with $D_{b\alpha\beta}$ being the diffusion tensor. This is the Fokker-Planck operator, the first term representing diffusion and the second the dynamical friction. Such operator (in the Landau form) was used in Baalrud, Hegna, and Callen 2009 to show evidences of instability-enhanced collisional frictions, that were observed experimentally in Hershkowitz, Yip, and Severn 2011 and showed good agreement with theory. Another example is the effect of Coulomb collisions on the dispersion relation for the Weibel instability that were investigated by Ryutov et al. 2014 in the context of laser-generated plasma streams.

We have seen that the inclusion of collisions in Vlasov equation may take several forms. Krook operators are the most simple and convenient ones to manipulate in analytical theory but they do not describe with a very good accuracy processes such as Coulomb collisions. Landau operator, in the other hand, has a much more complex form but is more precise in describing collisional processes. It is difficult to include in analytical calculations but can be approximated in self-consistent numerical simulations, and we will use such operator to study the effects of Coulomb collisions on the magnetic streaming instability. We now present some basic results on Coulomb collisions in a plasma and then introduce the collision module developed in the code.

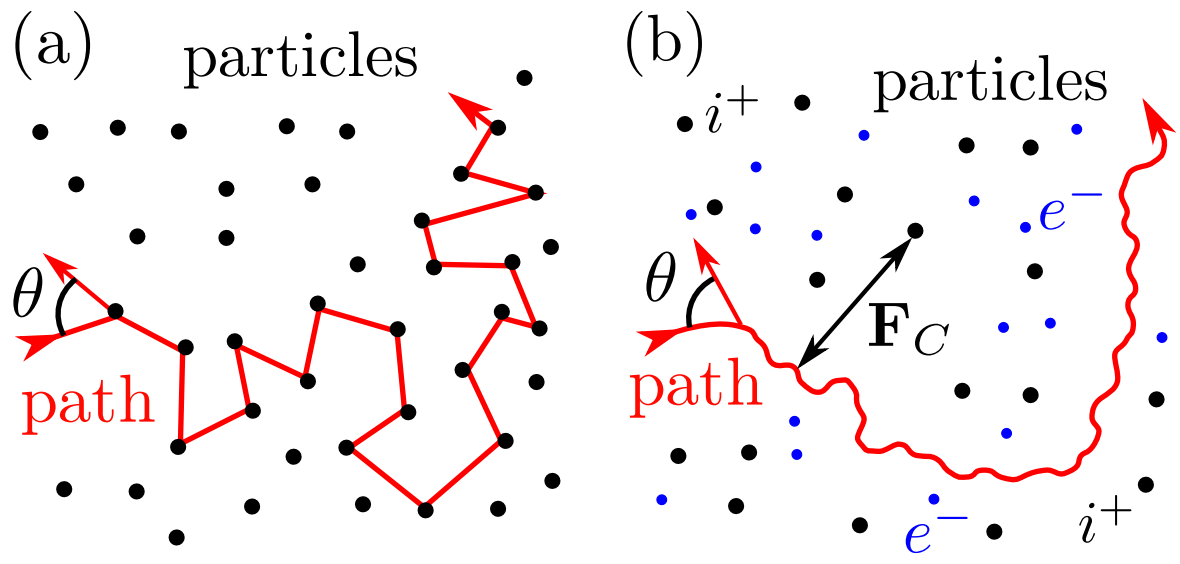

Figure 3.1: **(a)**: drawing of the path (red) of a particle experiencing a scattering angle θ after some collisions with neutrals. **(b)**: drawing of the path of a particle experiencing a scattering due to Coulomb collisions in a plasma.

3.4 Physics of Coulomb collisions

In collisionless plasmas, particle dynamics is driven by the interaction with macroscopic electromagnetic fields that are externally applied or self-induced by the distribution of particle's charge and current density. However, particle-particle interactions (collisions) due to the microscopic electric field generated by their charge are important in many plasmas. Because of their Coulomb nature, these collisions are long-range interactions: a given particle continuously interact with the electric field of many particles (within a Debye sphere) and generally undergoes many small deflections. Indeed close approaches between particles, and thus large-angle scattering are very rare in plasma. This is not the case for neutral collisions, where collisions produce overwhelmingly large-angle deflections. These ideas are schematically represented in Figure 3.1, which shows the path (in red) followed by a particle in these two different cases. Panel **(a)** shows the path followed by a particle experiencing collisions with neutral particles. The collisions are mostly binary (involving only two particles), and over a characteristic mean free path the particle moves along an unperturbed trajectory. On the other hand, panel **(b)** shows the path of a charged particle in a plasma, which is also experiencing a total scattering angle θ after some time. However in this case the Coulomb collisions produce mostly small angle deviations.

In this chapter, we present some elements of physics to describe the collisional processes inside a plasma, starting with the description of a two-body collision, then applying it to a plasma, which leads to define different collision frequencies relevant to the system. A more detailed development of these calculations can be found in Fitzpatrick 2014, and we here present only some of the main steps.

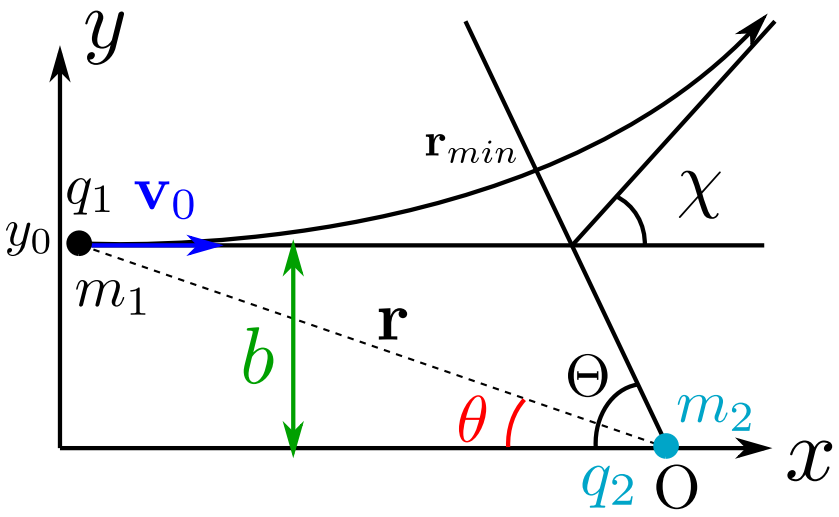

Figure 3.2: Drawing of the scattering of a pair of particles. The particle 1 approaching the particle 2 with the impact parameter b experiences a scattering of angle χ of its initial velocity $\mathbf{v}_0$. The relative velocity experiences a scattering of total angle Θ.

3.4.1 Binary collisions

We consider an elastic collision between two charged particles approaching each other, as shown in figure 3.2. A particle 1 with mass m_1 and charge q_1 approaches with velocity $\mathbf{v}_0$ another particle 2 with m_2 and q_2 that remains fixed at the origin O. The frame of reference is such that the velocity is along the x-axis ($\mathbf{v}_0 = v_0\mathbf{x}$), and the particle 2 is at the origin. After the collision, the particle experiences a scattering of angle χ of its velocity, and meanwhile the relative velocity between the two particles experiences a scattering by an angle Θ.

We define $\mathbf{r} = \mathbf{r}_1 - \mathbf{r}_2$ the relative position vector where $\mathbf{r}_1$ and $\mathbf{r}_2$ are the positions of the particles 1 and 2 and the relative velocity $\dot{\mathbf{r}} = \dot{\mathbf{r}}_1 - \dot{\mathbf{r}}_2$ (we note with a dot the time derivative of a quantity). The initial kinetic energy of the center of mass (when the distance between particles is large enough so there are no interacting forces between them) is associated with the initial value of the relative velocity $\dot{\mathbf{r}} = \mathbf{u}$:

$$E = \frac{1}{2}\mu_{12}u^2 \tag{3.29}$$

$$\mu_{12} = \frac{m_1 m_2}{m_1 + m_2} \tag{3.30}$$

with μ_{12} the reduced mass. The relative position vector experience the electrostatic force:

$$\mu_{12}\ddot{\mathbf{r}} = \frac{q_1 q_2}{4\pi\varepsilon_0}\frac{\mathbf{r}}{|\mathbf{r}|^3} \tag{3.31}$$

and the total energy is the sum of the kinetic energy, the angular momentum energy and the electrostatic energy and writes:

$$E = \frac{1}{2}\mu_{12}\left(\dot{r}^2 + r^2\dot{\theta}^2\right) + \frac{q_1 q_2}{4\pi\varepsilon_0 r} \tag{3.32}$$

Now we define $z = r^{-1}$, and θ as the angle between $\mathbf{r}$ and the x axis at a given time. We can show that the relative velocity also writes:

$$\dot{\mathbf{r}} = -h\frac{dz}{d\theta} \tag{3.33}$$

where $h = |\mathbf{h}| = r^2\theta$ is the modulus of the angular momentum. It follows that the energy can be expressed as:

$$E = \frac{1}{2}\mu_{12}\left(r^2\dot{\theta}\right)^2\left[\left(\frac{dz}{d\theta}\right)^2 + z^2\right] + \frac{q_1 q_2}{4\pi\varepsilon_0}z \tag{3.34}$$

The impact parameter $b = h/u$ is the distance of closest approach of the two particles in the absence of any force (the particle would then go straight). In figure 3.2, it corresponds to the initial y-coordinate y_0 of the particle 1. Equation 3.34 then gives:

$$b^2\left(\frac{dz}{d\theta}\right)^2 = 1 - b^2z^2 - \left(\frac{q_1 q_2}{4\pi\varepsilon_0 E}\right)z \tag{3.35}$$

At closest approach where the relative vector reaches its minimum value $r = r_{min}$ so $z = z_{max} = 1/r_{min}$, we can show that $(dz/d\theta)_{z_{max}} = 0$ which gives:

$$1 - b^2z_{max}^2 - \left(\frac{q_1 q_2}{4\pi\varepsilon_0 E}\right)z_{max} = 0 \tag{3.36}$$

Θ is the total scattering angle of the relative velocity at the end of the collisions. It can be found by integrating the θ angle as:

$$\Theta = \int_0^{z_{max}} \frac{d\theta}{dz}dz = \int_0^{z_{max}} \frac{b}{\sqrt{1 - b^2z^2 - \frac{q_1 q_2 z}{4\pi\varepsilon_0 E}}} \tag{3.37}$$

This integration gives:

$$\Theta = \frac{\pi}{2} - \sin^{-1}\left(\frac{q_1 q_2}{4\pi\varepsilon_0 E b\sqrt{4 + \left(\frac{q_1 q_2}{4\pi\varepsilon_0 E b}\right)^2}}\right) \tag{3.38}$$

The Coulomb force being reversible, by symmetry we can show that:

$$\chi = \pi - 2\Theta \tag{3.39}$$

from which we deduce the expression for the scattering angle of the particle 1:

$$\tan\left(\frac{\chi}{2}\right) = \frac{q_1 q_2}{4\pi\varepsilon_0 \mu_{12} u^2 b} \tag{3.40}$$

3.4.2 Rutherford cross-section and Landau operator

If a particle of species 1 streams with velocity u into a density n_2 of particles of species 2, the probability p_1 for the particle to experience be scattered by an angle $\Omega < \chi < \Omega + d\Omega$ is:

$$p_1(\Omega)d\Omega = n_2 u \frac{d\sigma}{d\Omega} d\Omega \tag{3.41}$$

where $d\sigma/d\Omega$ is the differential scattering cross-section. It can be shown that this differential scattering cross-section is given by:

$$\frac{d\sigma}{d\Omega} = \frac{1}{2}\left(\frac{q_1 q_2}{4\pi\varepsilon_0 \mu_{12} u^2}\right)^2 \frac{1}{\sin^4(\chi/2)} \tag{3.42}$$

We can see that the differential scattering cross-section becomes very large when $\sin(\chi/2)$ becomes small, showing the dominance of small-angle scattering in a plasma. Let's now consider the Boltzmann collision operator between species 1 and 2:

$$C_{12}(f_1 f_2) = \int\int\int u \frac{d\sigma}{d\Omega}\left(f_1' f_2' - f_1 f_2\right) d^3\mathbf{v}_2 d\Omega \tag{3.43}$$

where f_1 and f_2 are the distribution functions before the collision and f_1' and f_2' are the distributions after collision. The fact that small-angle scatterings dominate the Coulomb collisions allows some simplifications for C_{12}. In order to perform the integration, we will need to identify bounds for the scattering angle χ_{min} and χ_{max}, above and below which no collision can occur. This comes to identify bounds for the value of b, b_{min} and b_{max}, as both values are linked by equation 3.40.

The lower limit, b_{min}, corresponds to the maximum scattering χ_{max}. It is given by the closest approach possible between particles, that is the distance at which the initial kinetic energy equals the electrostatic energy. In the case of a two-body collision with relative velocity u, this is:

$$\frac{1}{2}\mu_{12}u^2 = \frac{q_1 q_2}{4\pi\varepsilon_0 b_{min}} \tag{3.44}$$

$$b_{min} = \frac{q_1 q_2}{2\pi\varepsilon_0 \mu_{12} u^2} \tag{3.45}$$

In the case of a distribution function, we can estimate the relative velocity assuming both colliding populations to have the same temperature and by taking the thermal velocity $v_T = \sqrt{k_B T/\mu_{12}}$. In this conditions we write the distance of closest approach as:

$$b_{min} = r_c = \frac{q_1 q_2}{2\pi\varepsilon_0 k_B T} \tag{3.46}$$

For the upper limit, we need to consider the Debye shielding of the charges outside the Debye sphere. In a simple way, at distances above the Debye radius from a given charged particle, the ambient charges have the effect of neutralizing the electric field of this particle. Thus particle 1 will not experience a collision with 2 if it does not get closer than the Debye length:

$$b_{max} = \lambda_D = \sqrt{\frac{\varepsilon_0 k_B T}{n_0 e^2}} \tag{3.47}$$

where T is the thermal energy of the plasma and n_0 its density. We can now define the Coulomb logarithm Λ.

$$\Lambda = \ln \lambda_c = \ln\left(\frac{b_{max}}{b_{min}}\right) = \ln\left(\frac{\lambda_D}{r_c}\right) \tag{3.48}$$

With some calculations and the newly defined Coulomb logarithm, we can now write the Landau collision operator as:

$$C_{12}^L = -\frac{1}{m_1}\frac{\partial}{\partial \mathbf{v}_1}\frac{q_1^2 q_2^2 \Lambda}{8\pi\varepsilon_0}\int\left[\frac{\delta_{jk}}{u} - \frac{u_j u_k}{u^3}\right]\left[\frac{f_1}{m_2}\frac{\partial f_2(v')}{\partial v'_k} - \frac{f_2(v')}{m_1}\frac{\partial f_1}{\partial v_k}\right] \tag{3.49}$$

This is the form of the Landau operator that is implemented in the code through an approximate Monte-Carlo collision model.

3.4.3 Collision frequencies

Collisions between particles are generally characterized by variety of collision frequencies, which we now briefly derive. Let's begin by assuming the population s of mass m_s, density n_s has a Maxwellian distribution function:

$$f_s(\mathbf{v}) = n_s\left(\frac{m_s}{2\pi k_B T_s}\right)^{3/2}\exp\left[-\frac{m_s(\mathbf{v}-\mathbf{V}_s)}{2k_B T_s}\right] \tag{3.50}$$

In the equation above $\mathbf{V}_s$ is the fluid velocity of the population s and T_s the thermal energy of the plasma. If we consider two populations with the same temperature and a relative velocity (say, the population 1 has a drift velocity and the population 2 does not, $\mathbf{V}_2 = 0$), there is a force acting on these populations due to collisional friction that tends to reduce the relative drift. This force $\mathbf{F}_{12}$ acting on the population 1 from the population 2 is:

$$\mathbf{F}_{12} = \int m_1 \mathbf{v} C_{12}^L d^3\mathbf{v} \tag{3.51}$$

After some calculations and under the assumption that the drift speed it smaller than the thermal speed $v_{T,s} = \sqrt{2k_B T/m_s}$, it can be written as:

$$\mathbf{F}_{12} = -\frac{m_1 n_1}{\tau_{12}}\mathbf{V} \tag{3.52}$$

where τ_{12} is the time it requires for the population 2 to decelerate the population 1 through collisional processes. This timescale takes the form:

$$\tau_{12} = \frac{6\sqrt{2}\pi^{3/2}\varepsilon_0^2 m_1 (k_B T)^{3/2}}{\Lambda m_{12}^{1/2} q_1^2 q_2^2 n_2} \tag{3.53}$$

$$m_{12} = \frac{m_1 m_2}{m_1 + m_2} \tag{3.54}$$

$$\nu_{12} = \frac{1}{\tau_{12}} = \frac{\Lambda m_{12}^{1/2} q_1^2 q_2^2 n_2}{6\sqrt{2}\pi^{3/2}\varepsilon_0^2 m_1 (k_B T)^{3/2}} \tag{3.55}$$

τ_{12} also corresponds to the mean time required for a particle 1 to experience a scattering of $\pi/2$ due to collisional interactions with a field of particles 2. As Coulomb interactions only affect charged particles, the different kind of collisions are the ion-ion collision ν_{ii}, the electron-electron collisions ν_{ee}, the ion-electron collisions ν_{ie} and the electron-ion collisions ν_{ei} which are:

$$\nu_{ii} = \frac{\Lambda Z_{i1}^2 Z_{i2}^2 e^4 n_e}{12\sqrt{2}\pi^{3/2}\varepsilon_0^2 m_i^{1/2} (k_B T)^{3/2}} \tag{3.56}$$

$$\nu_{ee} = \frac{\Lambda e^4 n_e}{12\sqrt{2}\pi^{3/2}\varepsilon_0^2 m_e^{1/2} (k_B T)^{3/2}} \tag{3.57}$$

$$\nu_{ie} = \frac{\Lambda Z_i^2 e^4 n_e m_e^{1/2}}{6\sqrt{2}\pi^{3/2}\varepsilon_0^2 m_i (k_B T)^{3/2}} \tag{3.58}$$

$$\nu_{ei} = \frac{\Lambda Z_i^2 e^4 n_e}{6\sqrt{2}\pi^{3/2}\varepsilon_0^2 m_e^{1/2} (k_B T)^{3/2}} \tag{3.59}$$

In general we have the following ordering between all these collision frequencies, provided that Z_i is not too big:

$$\tau_{ee} \sim \tau_{ei} \sim \left(\frac{m_e}{m_i}\right)^{1/2} \tau_{ii} \sim \left(\frac{m_e}{m_i}\right) \tau_{ie} \tag{3.60}$$

$$\nu_{ee} \sim \nu_{ei} \sim \left(\frac{m_i}{m_e}\right)^{1/2} \nu_{ii} \sim \left(\frac{m_i}{m_e}\right) \nu_{ie} \tag{3.61}$$

as can be seen, the time it takes for electrons to scatter between them or for a field of ions to scatter electrons is much shorter than the collision time between the ions, which itself is much shorter than the time it takes for a field of electrons to scatter an ion:

$$\tau_{ee} \sim \tau_{ei} \ll \tau_{ii} \ll \tau_{ie} \tag{3.62}$$

$$\nu_{ie} \ll \nu_{ii} \ll \nu_{ei} \sim \nu_{ee} \tag{3.63}$$

Over the time-scales of ion-ion collisions, the electrons can then be considered as a fluid, with collisions so frequent between the electrons that they are also expected to relax to a Maxwellian distribution faster than any of the processes we are interested in. The

frequency ordering also shows that the scattering time of ions by electrons is much larger than that between ions, justifying the fact that we take only into account the ion-ion collisions.

These times are essentially equilibration times. Trubnikov 1965 gives an ordering for the slowing down times of a flux of particles 1 in a background of particles 2. In the case of a high energy flux, for a kinetic energy much higher than the thermal energy:

$$\frac{E_k}{E_T}\frac{m_2}{m_1} \gg 1 \tag{3.64}$$

the ordering for ions and electrons populations is:

$$\tau_{ee} \sim \tau_{ei} \sim \sqrt{\frac{m_e}{m_i}}\tau_{ii} \sim \sqrt{\frac{m_i}{m_e}}\tau_{ie} \tag{3.65}$$

In this case we have $\tau_{ie} \ll \tau_{ii}$, but this is valid only when $E_{k,i}m_e \gg E_{T,e}m_i$. So for "superfast" ions, the energy exchange is mostly made with electrons. In the case of thermal ions ($E_k \sim E_T$), the ordering becomes the same as in equation 3.60. This section focused on Coulomb collisions. Collisions with neutrals will be addressed in section 3.7.

3.5 Numerical implementation of binary collisions

Several methods have been developed to include Coulomb collisions in PIC/hybrid codes. Two of the most efficient and widely used methods to simulate the Landau operator, were developed by Takizuka and Abe 1977 and Nanbu 1997. These Monte Carlo methods were compared in Wang et al. 2008, who showed Nanbu's method to be slightly more accurate, especially for small time steps. More recently, Dimarco et al. 2015 also presented a method for solving the Vlasov-Landau operator, using spectral methods, and found it to be in good agreement with analytical theory. We also note that for a hybrid model (as in the present study) collisions between the PIC ions and the electron fluid may also be included, for example by using the method detailed in Sherlock 2008. In the present work we implemented the method developed by Takizuka and Abe 1977 in our code Heckle. The essence of the method is based on the random pairing of macroparticles within a given computational cell and then calculating the scattering angle and their new velocities due to their collision. The following sections are devoted to present in detail this method and our implementation of it. We begin by describing the equations for calculating the scattering angle (section 3.5.1), how to apply this scattering to the macroparticles (section 3.5.2), and finally in section 3.5.3 we present the details of a correction developed in Nanbu and Yonemura 1998 to take into account collisions between particles of different statistical weights.

3.5.1 Calculation of the scattering angle

By including the collisions in the hybrid model, we essentially need to solve the modified Vlasov equation (for the ions):

$$\frac{\partial f_\alpha}{\partial t} + \mathbf{v} \cdot \frac{\partial f_\alpha}{\partial \mathbf{x}} + \frac{e}{m_\alpha} (\mathbf{E} + \mathbf{v} \times \mathbf{B}) \cdot \frac{\partial f_\alpha}{\partial \mathbf{v}} = \left(\frac{\delta f_\alpha}{\delta t} \right)_c \tag{3.66}$$

where the right-hand side of the equation represents the effects of collisions. This collision operator is the Landau-Fokker-Planck operator ((see equation 3.49); Landau 1965, Wang et al. 2008), and it is approximated in our hybrid code with the Monte Carlo method developed by Takizuka and Abe 1977.

The first step of the algorithm is to make random pairs of particles within a given computational grid cell, and calculate a scattering angle. As we can deal with several ion populations, we need to distinguish two types of collisions: the collisions inside a given population (intra-specie collisions) and the collisions between particles of different populations (inter-species collisions).

For the intra-species collisions, there are two cases:

- if the cell contains an even number of particles, pairs are made such that each particle are in one and only one pair;
- if there is an odd number N of particles in the cell, we proceed as explained before in the even case for the $N-3$ first particles, and make three pairs out of the three remaining particles, each one being paired with the other two and experiencing with them half-a-collision, that is a collision on half a time step.

For the inter-species collisions, there can be a large difference in the number of particles between the populations in a cell. Let us denote N_1 and N_2 the number of particles of the colliding species 1 and 2, and let's assume $N_1 > N_2$, with $N_1/N_2 = i + r$, where i an integer and $0 \leq r < 1$. We divide the populations into two groups:

- the first group composed of $(i+1)rN_2$ particles 1 and rN_2 particles of specie 2. Each particle 2 is paired with $i+1$ particles of specie 1;
- the second group composed of $i(1-r)N_2$ particles of specie 1 and $(1-r)N_2$ particles of specie 2. Each particle of specie 2 is taken i times in a pair with a particle 1.

Once the pairs of colliding macroparticles have been identified and their relative velocity $\mathbf{u}$ calculated, we can then proceed to determine the scattering angle via a Monte Carlo algorithm. We consider the frame in which the relative velocity before collision is along the z-axis, as shown in figure 3.3. Since the norm of the vector does not change in an elastic collision, we can then identify the post-collision velocity $\mathbf{u}(t+\Delta t)$ using the angles Θ and Φ. The computation of the angle Φ is done by sampling uniform random distribution with $0 < \Phi < 2\pi$. The scattering angle, Θ, of the relative velocity of a pair of particles is calculated from a Gaussian distribution of the variable δ, defined as:

$$\delta \equiv \tan(\Theta/2) \tag{3.67}$$

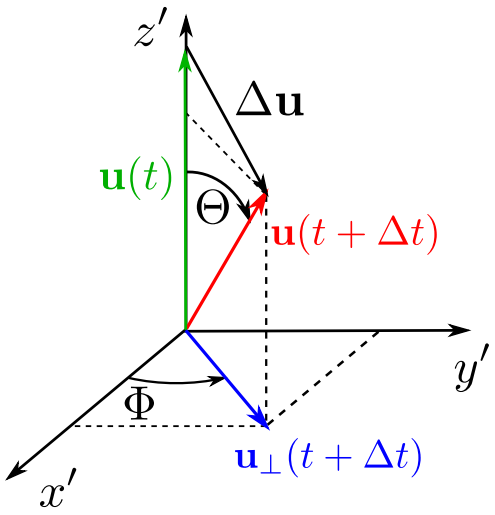

Figure 3.3: Spherical set of coordinate used to define the scattering angle. The initial relative velocity at time t $\mathbf{u}(t)$ is along the z-axis and the post-collision velocity $\mathbf{u}(t+\Delta t)$ is deviated of an angle Θ and located with the angle Φ.

The variable has mean zero and variance:

$$\left\langle \delta^2 \right\rangle = \nu_{\alpha\beta}\Delta t \tag{3.68}$$

with $\nu_{\alpha\beta}$ the collision frequency associated with the pair of macroparticles and Δt the numerical time step of the simulation. Figure 3.4, shows the probability distribution of the variable δ. It describes the collisionality of two macroparticles based on the time step during which they experience the collision and a frequency, which is defined as

$$\nu_{\alpha\beta} = \frac{q_\alpha^2 q_\beta^2 n_L \Lambda}{8\pi\varepsilon_0^2 m_{\alpha\beta}^2 u^3} \tag{3.69}$$

In the equation above one particle of species α with mass m_α and charge q_α collides with a macroparticle of specie β. The other symbols are, Λ the Coulomb logarithm, n_L the lowest density between n_α and n_β and $m_{\alpha\beta} = m_\alpha m_\beta/(m_\alpha + m_\beta)$ the reduced mass. The following relations help calculating the velocity changes using the variable δ:

$$\sin\Theta = \frac{2\delta}{(1+\delta^2)} \tag{3.70}$$

$$1-\cos\Theta = \frac{2\delta^2}{(1+\delta^2)} \tag{3.71}$$

Before presenting the method to calculate the post-collision velocities from the scattering angles (next section) we discuss here the normalization used in Heckle. We remind from section 3.2 that the code uses a set of units that can be fully described by m_p, e, B_0 and n_0. m_p and e are physical constants and B_0 and n_0 are respectively a magnetic field

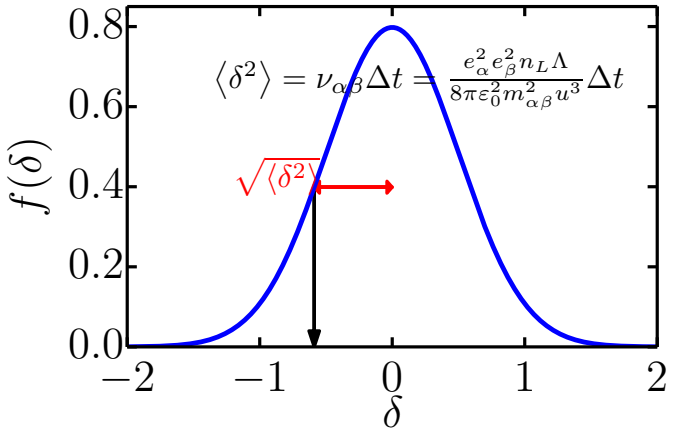

Figure 3.4: Distribution function of the δ parameter. The mean is zero and the variance $\left\langle\delta^2\right\rangle = \nu_{\alpha\beta}\Delta t$.

and a density used for normalization.

The collision force has a simple expression in which the collision frequency is the only needed parameter. From the Rutherford scattering expression given by equation 3.69, this should be straightforwardly implemented in the hybrid PIC code. But as previously detailed, the Heckle code is using dimensionless quantities. However, the expression of the collision frequency involves the permittivity ε_0 that is not known by the dimension system used in Heckle. In other words, the collision frequency can not be reduced to a combination of the units that are the proton mass, the elementary charge, the Alfvén speed and the ion cyclotron frequency. To solve this problem, we feed the algorithm a parameter used to calculate the collision frequency from the other dimensionless quantities manipulated in the code. This parameter is called σ_0 and writes:

$$\frac{\sigma_0}{\Omega_0} = \frac{e^4 n_0}{8\pi\varepsilon_0^2 m_p^2 V_0^3} = \frac{e^4 n_0 \left(\mu_0 m_p n_0\right)^{3/2}}{8\pi\varepsilon_0^2 m_p^2 B_0^3} \tag{3.72}$$

σ_0 is expressed in units of Ω_0 because it is the unit of frequency used in the code. As we can see, fixing σ_0 comes to artificially fixing the value of ε_0 with respect to the unit density and magnetic field. Thus, increasing the σ_0 parameter can mean increasing the density of the plasma we consider or decreasing the magnetic field in the system. There is a similar problem in the definition of the Coulomb logarithm. Indeed, Coulomb logarithm depends on the ratio between the Debye length and the Landau length. Both of these lengths are associated to micro-physical processes involving departure from neutrality and their associated force. Because of the quasineutrality hypothesis, all these effects are not taken into account in the hybrid model. Here again we use a parameter Ψ_0 to calculate

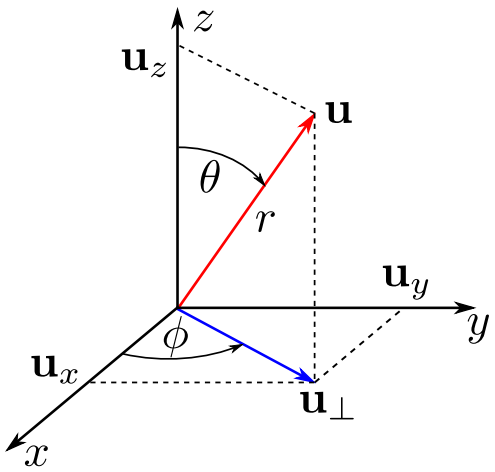

Figure 3.5: The relative velocity $\mathbf{u}$ of the pair of particles in the laboratory frame, located by the angle θ and ϕ in a spherical coordinate set.

the Coulomb logarithm, that is defined as follow:

$$\Psi_0 = \log\left(\frac{4\pi\left(k_B T_0 \varepsilon_0\right)^{3/2}}{e^3\sqrt{n_0}}\right) \tag{3.73}$$

where $k_B T_0 = m_p V_0^2$. We thus need to fix a numerical value for these parameters from the physical values obtained in laboratory plasmas or in the interstellar medium.

The collision frequency is thus calculated using σ_0 and Ψ_0 as:

$$\nu_{\alpha\beta} = \sigma_0 \frac{\tilde{q}_\alpha^2 \tilde{q}_\beta^2 \tilde{n}_L}{\tilde{m}_{\alpha\beta}^2 \tilde{u}^3}\left[\Psi_0 - \log\left(\frac{\tilde{q}_\alpha \tilde{q}_\beta\left(\tilde{m}_\alpha + \tilde{m}_\beta\right)}{\tilde{m}_\beta k_B \tilde{T}_\alpha + \tilde{m}_\alpha k_B \tilde{T}_\beta}\left(\frac{\tilde{n}_\alpha \tilde{q}_\alpha^2}{k_B \tilde{T}_\alpha} + \frac{\tilde{n}_\beta \tilde{q}_\beta^2}{k_B \tilde{T}_\beta}\right)^{1/2}\right)\right] \tag{3.74}$$

where $\tilde{q}_s = q_s/e$, $\tilde{n} = n/n_0$, $\tilde{m}_s = m_s/m_p$, $\tilde{u} = u/V_0$ and $k_B \tilde{T}_s = \tilde{m}_s \tilde{v}_{T,s}^2$ where $\tilde{v}_{T,s} = v_{T,s}/V_0$ is the thermal velocity of the specie s. The term between brackets corresponds to the Coulomb logarithm (Λ in equation 3.69).

3.5.2 Changes of velocities

Following a collision, the relative velocity of a pair of particles $\mathbf{u} = (u_x, u_y, u_z)$ experiences a change of velocity. We define θ and ϕ the spherical angles locating $\mathbf{u}$ in the laboratory frame (as showed in figure 3.5) and Θ and Φ are the spherical scattering angles as previously defined and showed in figure 3.3.

The particles α and β experience a binary collision. Their velocity change is given by:

$$\mathbf{v}'_\alpha = \mathbf{v}_\alpha + \frac{m_{\alpha\beta}}{m_\alpha}\Delta\mathbf{u} \tag{3.75}$$

$$\mathbf{v}'_\beta = \mathbf{v}_\beta - \frac{m_{\alpha\beta}}{m_\beta}\Delta\mathbf{u} \tag{3.76}$$

where $\Delta\mathbf{u} = (\Delta u_x, \Delta u_y, \Delta u_z) = \mathbf{v}_\alpha - \mathbf{v}_\beta$ is calculated in the relative velocity frame with the scattering angles Θ and Φ (see figure 3.3). We can see that the equations explicitly conserves the total momentum. The change in velocity $\Delta\mathbf{u}$ in the initial relative velocity frame can be found using a rotation vector with angles Θ and Φ:

$$\mathbf{u}(t) = u\begin{pmatrix}0\\0\\1\end{pmatrix} \tag{3.77}$$

$$u\begin{pmatrix}\sin\Theta\cos\Phi\\ \sin\Theta\sin\Phi\\ \cos\Theta\end{pmatrix} = \mathbf{u}(t+\Delta t) \tag{3.78}$$

$$\Delta\mathbf{u} = \mathbf{u}(t+\Delta t) - \mathbf{u}(t) = \begin{pmatrix}\sin\Theta\cos\Phi\\ \sin\Theta\sin\Phi\\ (\cos\Theta - 1)\end{pmatrix} \tag{3.79}$$

The relative velocity in the laboratory frame is located with the angles θ and ϕ (see figure 3.5). Thus, to calculate the change of velocity in the laboratory frame we need to apply a rotation matrix to the change of velocity calculated before:

$$\begin{pmatrix}\cos\theta\cos\phi & -\sin\phi & \sin\theta\cos\phi\\ \cos\theta\sin\phi & \cos\phi & \sin\theta\sin\phi\\ -\sin\theta & 0 & \cos\theta\end{pmatrix} u\begin{pmatrix}\sin\Theta\cos\Phi\\ \sin\Theta\sin\Phi\\ (\cos\Theta-1)\end{pmatrix} = \begin{pmatrix}\Delta u_x\\ \Delta u_y\\ \Delta u_z\end{pmatrix} \tag{3.80}$$

with $u = |\mathbf{u}|$. This gives the three components of the change in the relative velocity:

$$\Delta u_x = \cos\phi u\cos\theta\sin\Theta\cos\Phi - \sin\phi u\sin\Theta\sin\Phi - u\sin\theta\cos\phi\,(1-\cos\Theta) \tag{3.81}$$

$$\Delta u_y = \sin\phi u\cos\theta\sin\Theta\cos\Phi + \cos\phi u\sin\Theta\sin\Phi - u\sin\theta\sin\phi\,(1-\cos\Theta) \tag{3.82}$$

$$\Delta u_z = -u\sin\theta\sin\Theta\cos\Phi - u\cos\theta\,(1-\cos\Theta) \tag{3.83}$$

We define the following quantities (see figure 3.5):

$$u_\perp = u\sin\theta \tag{3.84}$$

$$u_x = u_\perp\cos\phi = u\sin\theta\cos\phi \tag{3.85}$$

$$u_y = u_\perp\sin\phi = u\sin\theta\sin\phi \tag{3.86}$$

$$u_z = u\cos\theta \tag{3.87}$$

With $u_\perp = \sqrt{u_x^2 + u_y^2}$ and $u = |\mathbf{u}|$. We get the following expressions for the change of relative velocity in the laboratory frame:

$$\Delta u_x = (u_x/u_\perp)\,u_z\sin\Theta\cos\Phi - (u_y/u_\perp)\,u\sin\Theta\sin\Phi - u_x\,(1-\cos\Theta) \tag{3.88}$$

$$\Delta u_y = (u_y/u_\perp)\,u_z\sin\Theta\cos\Phi + (u_x/u_\perp)\,u\sin\Theta\sin\Phi - u_y\,(1-\cos\Theta) \tag{3.89}$$

$$\Delta u_z = -u_\perp\sin\Theta\cos\Phi - u_z\,(1-\cos\Theta) \tag{3.90}$$

3.5.3 Correction for particle weightings

The algorithm of Takizuka and Abe 1977 that we presented only works for particles of the same statistical weight, $W_{s,i}$, which for the specie s and the particle i, is defined as:

$$n_s = \sum_{i=1...N_s} W_{s,i} \tag{3.91}$$

However, it is often the case that different species have disparate densities (or masses) for example. It is thus more convenient, from a computational perspective, to use different statistical weights for the particles. When two particles involved in a collision have different weights, a correction needs to be made to Takizuka's algorithm. This correction is detailed in Miller and Combi 1994 and Nanbu and Yonemura 1998, and we here present the necessary modification to the method outlined earlier.

The first part of the correction consists in a modification of the δ parameter presented in equation 3.68: for the particles of species α and β with number of macroparticles N_α and N_β and weights W_α and W_β (every particles in a given specie has the same weight), the corrected parameter δ_{corr} is given as follow:

- when $N_\alpha > N_\beta$, δ is multiplied by the factor:

$$\delta_{corr} = \delta \frac{\max(W_\alpha, W_\beta)}{W_\beta}$$

- when $N_\alpha < N_\beta$, δ is multiplied by the factor:

$$\delta_{corr} = \delta \frac{\max(W_\alpha, W_\beta)}{W_\alpha}$$

The second part of the correction is to introduce a probability for the particles to experience a scattering after a collision so that a "heavier" particle experience less scatterings than a "lighter" one:

- for $W_\alpha > W_\beta$, the probability is W_β/W_α for the particle α and 1 for the particle β;
- for $W_\alpha < W_\beta$, the probability is W_α/W_β for the particle β and 1 for the particle α.

We stress that because of this correction, the explicit conservation of energy breaks down. However, energy is still conserved on average for a large number of particles and time steps.

3.6 Benchmarks for the collision module

In order to test the collision module, we carry out a number of benchmarks tests. These correspond to some common physical situation where analytical results or published numerical results exist for comparison. For testing purposes, we use a 0D-model that takes in account only the velocity components of the particles and not their spatial

position. The tests are thus equivalent to the algorithm being applied to a single cell of the computational domain. For the tests, the particles are initialized randomly with a given distribution function, using either a Box and Muller algorithm (used to generate random velocities according to a Maxwellian distribution) or an uniform random number generator (for a step function). In this case, the collision frequency is calculated as well as in the HECKLE code, using a given set of the two parameters σ_0 and Ψ_0. The tests carried out are:

- Temperature anisotropy relaxation;
- Temperature equilibration of two populations;
- Relaxation to a Maxwellian and energy conservation;
- Collisional beam scattering.

For each of these situations we run convergence tests by varying the number of particles and/or the time step.

3.6.1 Temperature anisotropy relaxation

We start with a distribution in velocity that is anisotropic such that $T_x = T_\parallel > T_y = T_z = T_\perp$. The initial temperature difference, $(T_\parallel - T_\perp)/T_\parallel \ll 1$. Collisions are expected to make the system relax to an isotropic distribution ($T_\parallel = T_\perp$). This is shown in figure 3.6 **(a)**, where we can see the temperature in different directions relax to the same value. The temperature difference $\Delta T = \left|T_\perp - T_\parallel\right|$ obeys the following equation (see Trubnikov 1965):

$$\frac{dT_\perp}{dt} = -\nu_T^\alpha (T_\perp - T_\parallel) \tag{3.92}$$

with

$$\nu_T^\alpha = \frac{e_\alpha^2 e_\beta^2 n_\alpha \Lambda}{8\pi^{3/2}\varepsilon_0^2 m_\alpha T^{3/2}} A^{-2}\left[-3 + (A+3)\frac{\arctan\left(A^{1/2}\right)}{A^{1/2}}\right] \tag{3.93}$$

$$A = \left(\frac{T_\perp}{T_\parallel}\right) - 1 \tag{3.94}$$

We now present the numerical results of the relaxation of a distribution with an initial anisotropic temperature and compare it to theoretical predictions. In order to study a substantial statistical sample, we perform 160 runs for each situations and take the mean of the temperatures over all the simulations. Figure 3.6 **(b)** shows the evolution of the temperature anisotropy:

$$\left(\frac{\Delta T(t)}{\Delta T(0)}\right)_{\parallel/\perp} = \frac{T_\parallel(t) - T_\perp(t)}{T_\parallel(0) - T_\perp(0)} \tag{3.95}$$

for different numerical timesteps: $\Delta t\ \sigma_0 = 0.005$, $\Delta t\ \sigma_0 = 0.002$ and $\Delta t\ \sigma_0 = 0.001$. As expected, decreasing the timestep improves the numerical solution, and we find good

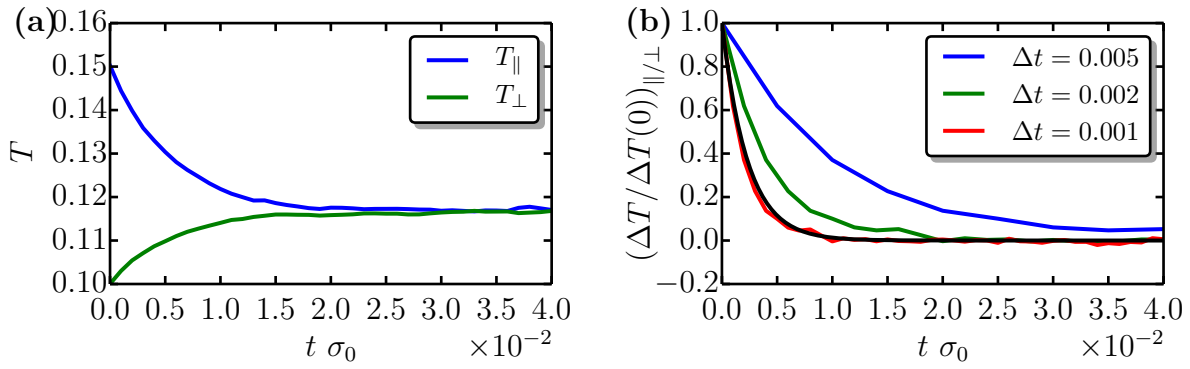

Figure 3.6: **(a)**: evolution of anisotropic temperatures (temperatures parallel and perpendicular $T_\parallel$ and $T_\perp$ to the magnetic field) with time due to collisions. **(b)**: temperature anisotropy ($(\Delta T)_{\parallel/\perp} = T_\parallel - T_\perp$ normalized to its initial value) relaxation for different timesteps $\Delta t\ \sigma_0$. The analytical solution is shown in black.

agreement for $\Delta t\ \sigma_0 = 0.001$. Figure 3.7 **(a)** shows the evolution of the anisotropy for different number of particles: a small number case, with an even and odd number of particles, and a high number case, again with an even and odd number of particles. The evenness of N needs to be tested because this case goes into a different loop in the code, that also needs a benchmark trial. We can see that changing the number of particles in a cell (in that case, multiplied by 8) does not significantly change the solution, only the solution fluctuates a lot in time. This is consistent with the results found in Wang et al. 2008 for the Takizuka and Abe algorithm, and shows that once the number of macroparticles is high enough (meaning that the sampling of the distribution function is good enough), there is no better accuracy on collisional processes when increasing this number.

Finally, in figure 3.7 **(b)** we show the same anisotropic temperature test case, but implemented in the full code, that is including the particle pusher and the electromagnetic field solvers. The blue line corresponds to the case with collisions and the green line is with for the case where collisions are disabled. The numerical solution recovers the analytical prediction when collisions are present, and there is no isotropization when the module is not activated. This shows that the collision module integrates well within the code and that there are no spurious effects.

3.6.2 Temperature equilibration of two populations

We start with two populations 1 and 2 that have a different isotropic temperature. We expect both plasma to relax to a single temperature obeying the equation:

$$\frac{dT_1}{dt} = \nu_\varepsilon^{1/2}\,(T_2 - T_1) \tag{3.96}$$

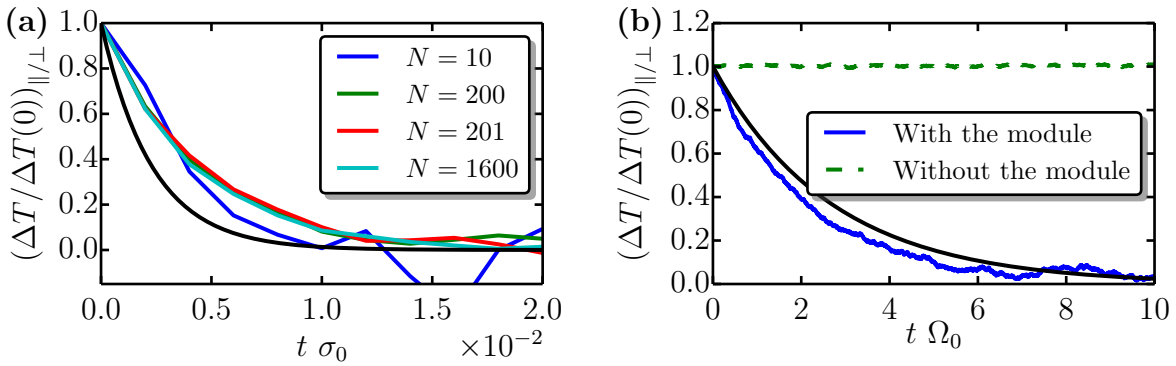

Figure 3.7: **(a)**: temperature anisotropy ($(\Delta T)_{\parallel/\perp} = T_\parallel - T_\perp$ normalized to its initial value) relaxation for different numbers of particles: $N = 200$ (blue), $N = 201$ (green), $N = 1600$ (red), $N = 1601$ (cyan). The timestep is $\Delta t\ \sigma_0 = 10^{-2}$. **(b)**: temperature anisotropy relaxation in the HECKLE code. The black line corresponds to the analytical solution.

with $\nu_\varepsilon^{1/2}$ the thermal relaxation rate defined as:

$$\nu_\varepsilon^{1/2} = \frac{e^4 Z_\alpha^2 Z_\beta^2 \sqrt{m_1 m_2} n_i \ln\Lambda}{8\varepsilon_0^2 (m_1 k_B T_1 + m_2 k_B T_2)^{3/2}} \tag{3.97}$$

Z_s is the charge state of the specie: $q_s = Z_s e$.

As done previously, we vary the time step and the number of particles, and compare with the theoretical solution. We take the average of the temperature over 160 simulations. For these simulations, we take two populations, one corresponding to the electrons and the other to the ions, with a mass ratio of $m_2/m_1 = 10$, and having opposite charges. The initial temperatures are $T_1 = 0.1$ and $T_2 = 0.075$.

Figure 3.8 **(a)** plots the relaxation of a temperature difference:

$$\left(\frac{\Delta T(t)}{\Delta T(0)}\right)_{1/2} = \frac{T_1(t) - T_2(t)}{T_1(0) - T_2(0)} \tag{3.98}$$

for different timestep, when both populations have the same number of particles $N_1 = N_2 = 1000$, the black line is the theoretical expectation. As we decrease the timestep, the module recovers well the theoretical solution for a $\Delta t\ \sigma_0 = 0.0001$.

Figure 3.8 **(b)** shows the thermalization for $\Delta t\ \sigma_0 = 10^{-3}$ and different number of particles, with still an equal number of particles for both species, $N_1 = N_2$. This shows that the number of particles does not change the numerical solution. Again, as in the previous section, this means that once there are a sufficient number of macroparticles experiencing collisions, there is no accuracy to gain by increasing it. We can also see that the number of needed particles to achieve sufficient precision is not very high (less than 100 in the case of figure 3.8 **(b)**) and such number is anyway needed to observe the magnetic streaming with a sufficient accuracy.

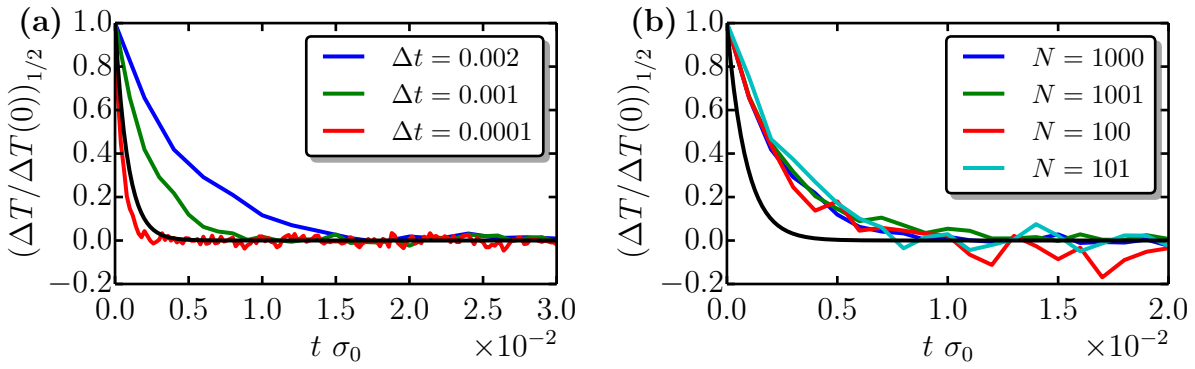

Figure 3.8: **(a)**: relaxation of a temperature difference $(T_1 - T_2)\,/\,(T_1(0) - T_2(0))$ with time for different timesteps: $\Delta t\ \sigma_0 = 0.002$ (blue line), $\Delta t\ \sigma_0 = 10^{-3}$ (green line) and $\Delta t\ \sigma_0 = 10^{-4}$ (red line), the analytical solution being plotted in black. $N_1 = N_2 = 1000$. **(b)**: relaxation of a temperature difference with time for different number of particles with $N_1 = N_2$: $N = 1000$ (blue line), $N = 1001$ (green line), $N = 100$ (red line), $N = 101$ (blue line). Here $\Delta t\ \sigma_0 = 10^{-3}$.

We now test the correction of the collision algorithm due to the use of different particles weightings. Figure 3.9 **(a)** shows the temperature difference as a function of time for $\Delta t\ \sigma_0 = 10^{-3}$ and different particle weight for the species 2. This means that for the same number of particles for the specie 1, $N_1 = 1000$, we vary the number of particles of the specie 2 with the same physical density. The statistical weight W of the macroparticles will then vary, with $W_1 < W_2$ when $N_1 > N_2$, and $W_1 > W_2$ when $N_1 < N_2$. It is clear from the figure that solution is not affected by the change in particle weighting and that the correction works well for this case. Figure 3.9 **(b)** plots the thermalization of two populations in the HECKLE code with and without the collisions. Again, the temperature difference relaxes only in the presence of collisions and it is not present when those are off.

3.6.3 Relaxation to a Maxwellian and energy conservation

In this test, we verify the relaxation of a non-Maxwellian particle distribution towards a Maxwellian distribution. We initialize a single population with a step function velocity distribution function. It is a constant distribution for $-a < v < a$ and zero elsewhere, with $a = \sqrt{3k_BT/m}$ and T being the equivalent temperature of the population. Figure 3.10 shows the evolution of the distribution function with time ($t\ \sigma_0 = 0, 2, 100$), starting with a step function. We can see that the initial distribution relaxes to a Maxwellian distribution (the black curve). If we calculate the total energy in the system ($\sum_p m_p v_p^2/2$) at every time step, we can check the conservation of energy by the algorithm.

Figure 3.11 shows the evolution of the total kinetic energy of the particles with time, calculated from the standard deviation of the distribution function at each time, $\sum_p \left\langle v_p^2 \right\rangle$, for different number of particles in the simulation. The energy is conserved in average, but large statistical fluctuations are seen for a low number of macroparticles. These fluctuations get less important as we increase the number of particles N in the simulation.

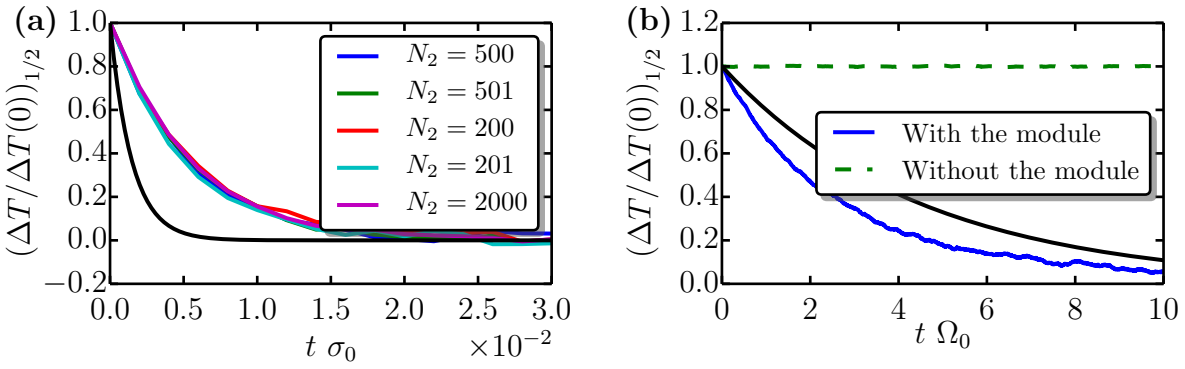

Figure 3.9: **(a)**: relaxation of a temperature difference ($((\Delta T)_{1/2} = T_1 - T_2$ normalized to its initial value)) for different particle weights W. Here $\Delta t\ \sigma_0 = 10^{-3}$ and $N_1 = 1000$. **(b)**: temperature relaxation in the HECKLE code with (blue) and without (green) the collision enabled. The black line corresponds to the analytical solution.

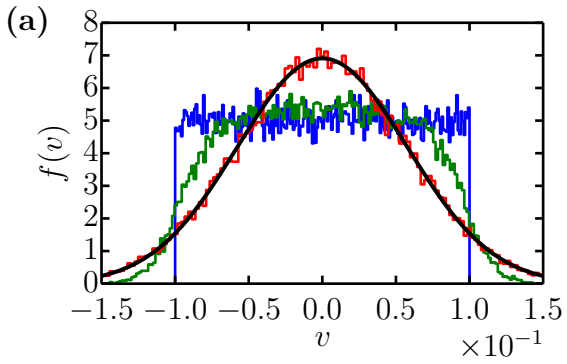

Figure 3.10: Relaxation of a step distribution function to a Maxwellian. In this figure $\Delta t\ \sigma_0 = 10^{-6}$ and $N = 50000$ to get a sufficient statistical sampling of the initial distribution. The curves are for times $t = 0$ (blue), $t\ \sigma_0 = 2$ (green) and $t\ \sigma_0 = 100$ (red). The black line is the corresponding Gaussian function.

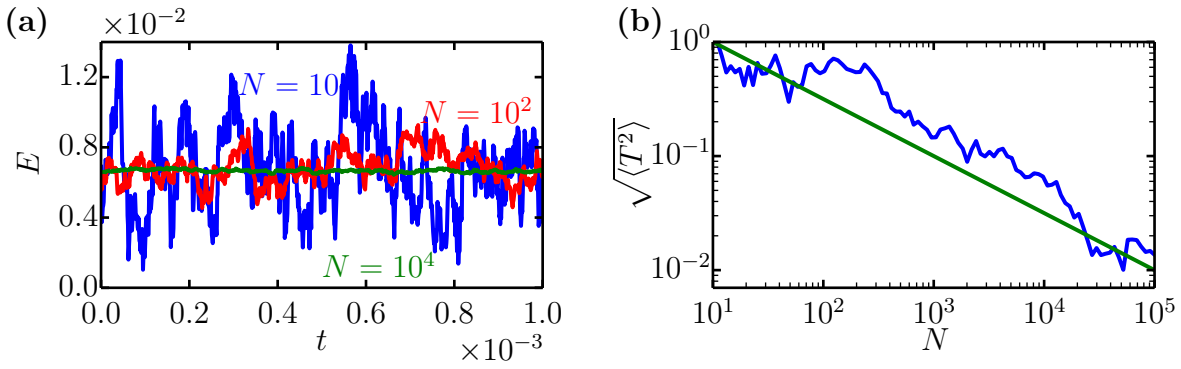

Figure 3.11: **(a)**: random variations of the energy during the relaxation of a step function to a Maxwellian for different number of macroparticles: $N = 10, 100, 10^4$. **(b)**: evolution of the variance of the noise in the energy produced by the relaxation to a Maxwellian with the number of used particles $\sqrt{\langle E^2 \rangle}$. The theoretical line is plotted in green.

We can measure how important these variations are by calculating the standard deviation of the energy $\sqrt{\langle E^2 \rangle}$ for a given simulation. Provided that the error on the relative velocity changes, is a random variable with a normal distribution, the standard deviation of the distribution of the variances of this variable (that we note $\sqrt{\langle E^2 \rangle}$) has the dependence $\sqrt{\langle E^2 \rangle} \propto 1/\sqrt{N}$ according to the central limit theorem. This means that as we increase the number of particles the fluctuation of the total energy decrease in amplitude. This is indeed the case, as shown in figure 3.11 **(b)**, $\sqrt{\langle E^2 \rangle}$ as a function of N (blue curve) and the $-1/2$ power law dependence (green line) predicted by the theory, together with the numerical results.

3.6.4 Collisional beam scattering

When a test particle of speed v_0 goes through a background plasma it experiences a scattering and a slowing down due to the collisions (see section 3.4). This slowing down is analytically expressed as:

$$v_{\parallel}(t) = v_0 e^{-\nu_{\parallel} t} \tag{3.99}$$

with the following expressions for the collisional slowing down (see Trubnikov 1965):

$$\nu_{\parallel} = -\left(1 + \frac{m_e}{m_i}\right)\nu_0 \tag{3.100}$$

$$\nu_0 = \frac{e^4 Z*^2 n_i \ln\Lambda}{4\pi\varepsilon_0^2 m_e^2 v_e^3} \tag{3.101}$$

Here we run zero-dimensional simulation of a beam of electrons going through a background of ions with velocity $v_0 = 10$ with $m_i/m_e = 10$. Similar results are obtained with an ion beam. Figure 3.12 shows the evolution of the electron parallel (blue) and perpendicular (red) velocities and the ion parallel velocity (green) when the electrons initially have a drift velocity. The theoretical solution for the electron parallel velocity is shown in

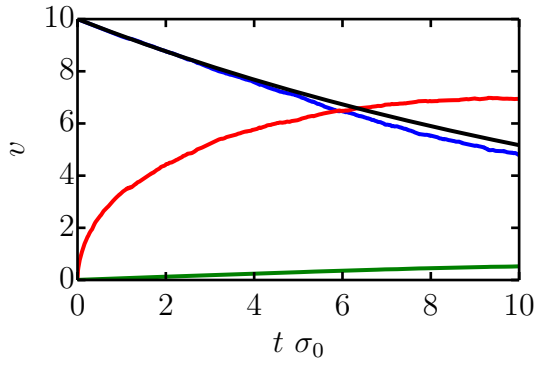

Figure 3.12: Evolution of the particle test velocity parallel (blue) and perpendicular (red) components to the initial velocity and the background parallel velocity (green) due to collisions. The black line corresponds to the theoretical solution for the slowing down of the beam.

black, and we can see that is corresponds well to the numerical solution, especially at early times. We can see that the collisions have the effects of scattering the beam, transferring the initial directed energy into perpendicular energy. The ion are accelerated, although only slightly because of their high inertia, and the total momentum is conserved.

In summary, we have tested the numerical model for the collisions on a variety of test cases. The results correspond well to the analytical predictions. More precisely, the numerical solution tends to converge to the theoretical one when increasing the time resolution. We find that using a timestep of about $\Delta t\ \Omega_0 \approx 10^{-3}$ is enough to achieve a good resolution for the collisions. We found that the number of particles necessary to achieve a good accuracy of the collisional processes (less than 50) is much less than the number of particles necessary to properly describe the instability processes. There is thus no limit in that way coming from the introduction of collisions in the simulations.

3.7 Collisions with neutrals

In addition to Coulomb collisions, charged particles in a plasma can interact with some neutrals when the plasma is not fully ionized. In that case, as opposite to the Coulomb collision, the electrostatic force is not involved and the physics of the collision is quite different. A particle can interact with a neutral when experiencing a hard-sphere kind of collision with it, as it happens all the time and even dominates the dynamics in neutral gases. In that case, the deviation angle θ only depends on the impact parameter b (see section 3.4) and on the radius of the sphere a only if $b < a$ as (see Rax 2005):

$$\cos\frac{\theta}{2} = \frac{b}{a} \tag{3.102}$$

If we consider mainly interactions with atoms, the typical cross section for this type of collisions is of the order of the section of an atom, the Bohr cross section $\sigma_B = \pi a_0^2$ where

$a_0 = 0.529.10^{-10}$ m is the Bohr radius of the hydrogen atom. This collision is similar to the one experienced by two billiard balls and the scattering angle is calculated geometrically.

In weakly ionized plasmas, the collision frequency between a charged particle a and neutral is:

$$\nu_a = n_0 \sigma_s^{a/0} \left(\frac{k_B T_a}{m_a} \right)^{1/2} \tag{3.103}$$

with n_0 the neutral density, $\sigma_s^{a/0}$ the cross section of the order of $\sigma_s^{a/0} \approx 5.10^{-17}\text{cm}^{-2}$. $(k_B T_a/m_a)^{1/2}$ is the thermal velocity of the charged population, and needs to be higher than the thermal velocity of the neutrals: $(k_B T_a/m_a)^{1/2} > (k_B T_0/m_0)^{1/2}$.

Beside the scattering that happens during a collision with a neutral particle, some other processes occur such as the ionization of the particle, its excitation, or a charge exchange between the two particles. To account for the charge exchange, Nanbu and Kitatani 1995 developed a model of ion-neutral collision and checked its validity for a number of different populations. These collisions are inelastic because the total kinetic energy is not conserved, some of it being used up in atomic processes, such as excitation. Interactions with neutrals are often included in simulations of cold plasmas such as in electric discharges Vahedi and Surendra 1995.

3.8 Numerical setup

In section 3.2 we have presented the hybrid-PIC code Heckle, the collision module was then detailed in section 3.5 and tested in section 3.6. In this sections, we introduce the numerical set up used in the simulations whose results are presented in the rest of thesis.

We simulate two homogeneous Maxwellian ion populations (the **main** plasma, referred to with the subscript "m", and the **beam** , referred to with the subscript "b") on a 1D computational domain. Winske and Quest 1986 performed a comparison between 1D and 2D simulations of this instability and showed that a 1D description is adequate to study this type of electromagnetic instability when limiting to parallel modes. Indeed Wang and Lin 2003 showed similar results are obtained with 2D simulations.

The first component, the main plasma, has zero mean velocity, density $n_m = n_0$ and thermal energy T_m, and the other component, the beam has a mean velocity V_b, a density n_b and a thermal energy T_b. The computational domain has periodic boundary conditions. Most of the simulation are performed with hydrogen ions, so that $m_s = m_p$ and $q_s = e$.

The domain is set along the x-direction and has grid step $\Delta x = 1 l_0$. We performed simulations with a domain length of $L = 1000 l_0$ or $L = 10^4 l_0$. This gives a spatial Fourier domain ranging from $k_{min}\ l_0 = 2\pi/(2L) = 2\pi.10^{-3}$ or $k_{min}\ l_0 = 2\pi/(2L) = 2\pi.10^{-4}$ to $k_{max}\ l_0 = 2\pi/(2\Delta x) = \pi$, which covers the most unstable wavenumbers (Wang and Lin 2003). Because of the CFL condition on particles and electromagnetic fields, we use a timestep $\Delta t = 0.001\Omega_0^{-1}$, which provides a good balance between accuracy and computational time. There are approximately one hundred particles per cell and per component initially. The initial magnetic field $\mathbf{B}_0$ is in the x-direction. The setup allow us to study

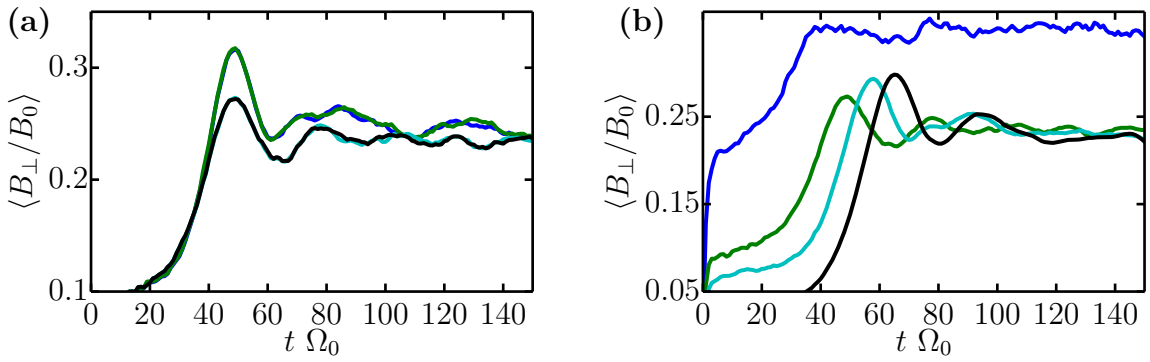

Figure 3.13: Convergence test of an unstable case while varying **(a)**: the timestep Δt and **(b)**: the number of macroparticles per cell N. **(a)**: $\Delta t\ \Omega_0 = 10^{-2}$ (blue), $\Delta t\ \Omega_0 = 2.10^{-2}$ (green), $\Delta t\ \Omega_0 = 10^{-3}$ (cyan) and $\Delta t\ \Omega_0 = 2.10^{-4}$ (black), with $\Delta x = l_0$ and $N = 50$. **(b)**: $N = 10$ (blue), $N = 50$ (green), $N = 100$ (cyan) and $N = 500$ (black), with $\Delta x = l_0$ and $\Delta t\ \Omega_0 = 10^{-3}$.

modes propagating parallel to the ambient magnetic field ($\mathbf{k} \times \mathbf{B} = 0$), which have been shown to be the fastest growing modes (see Wang and Lin 2003). We have also run an extensive set of simulations with increasing spatial and temporal resolution, as well as a larger number of particles per cell, to establish the optimum range of parameters.

Figure 3.13 displays the evolution of a simple case of instability that will be presented in chapter 4 when varying the timestep (panel **(a)**) and the number of particle (panel **(b)**). We can see that when changing the timestep, there is a jump before $\Delta t\ \Omega_0 = 10^{-3}$. Before this value, the solution is unchanged by the timestep, then changes at this value to remain also the same with higher time resolution. When changing the number of particles, the solution is noisy and very different for $N = 10$ compared to the other cases. When $N \geq 50$, the value of the growth rate as well as the magnetic saturation does not change, only the initial noise is lower when increasing N, making the instability develop later in time. Figure 3.14 shows the same case when varying the grid step Δx. We can see that the solution converges when $\Delta x \leq l_0$, and the saturation as well as the growth rate is the same for higher spatial resolution. For $\Delta x > l_0$, the solution becomes more different when increasing the grid step, with a lower level of saturation and growth rate. This means that for these values, the waves are not properly resolved and the instability is not correctly described. When decreasing Δx, the initial noise is also lower but this can be explained by the fact that there are more cells in the domain, thus more macroparticles, and this refers to the explanation of figure 3.13 **(b)**. We can see that the optimal values for these numerical parameters that we will use is $\Delta t\ \Omega_0 = 10^{-3}$, $N = 100$ and $\Delta x = l_0$.

For the collisional cases, only the value of the collision frequency (parameter σ_0) is varied, the Ψ_0 parameter is kept to 25, which is representative of many plasmas. Because of the presence of the log, this parameter is a very weak function of n_0 and T_0, and does not change appreciably the expression of the collision frequency. For example, in the solar wind, where $n_0 \approx 100 cm^{-3}$ and $B_0 \approx 10^{-9} T$, we have $\Psi_0 \approx 15$. In laboratory experiments, where $n_0 \approx 10^{23} m^{-3}$ and $B_0 \approx 20 T$, we have $\Psi_0 \approx 17$. To apply the simulation results to

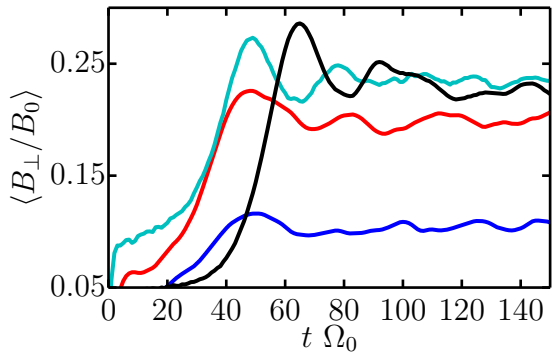

Figure 3.14: Convergence test of an unstable case while varying the grid step Δx: $\Delta x = 10 l_0$ (blue), $\Delta x = 5 l_0$ (red), $\Delta x = 1 l_0$ (cyan) and $\Delta x = 0.1 l_0$ (black) with $\Delta t\ \Omega_0 = 10^{-3}$ and $N = 50$.

environments with a lower or higher Coulomb logarithm, requires a small multiplicative factor to be applied to the general collision frequency.

Bibliography

Birdsall, C. K. and A. B. Langdon (1991). *Plasma Physics via Computer Simulation* (cit. on p. 33).

Lapenta, G. (2012). "Particle simulations of space weather". In: *Journal of Computational Physics* 231, pp. 795–821 (cit. on pp. 33, 36).

Krall, N. A. and A. W. Trivelpiece (1973). *Principles of plasma physics* (cit. on p. 34).

Winske, D. and K. B. Quest (1986). "Electromagnetic ion beam instabilities - Comparison of oneand two-dimensional simulations". In: *Journal of Geophysics Research* 91, pp. 8789–8797 (cit. on pp. 35, 36, 59).

Wang, X. Y. and Y. Lin (2003). "Generation of nonlinear Alfvén and magnetosonic waves by beam-plasma interaction". In: *Physics of Plasmas* 10, pp. 3528–3538 (cit. on pp. 35, 59, 60).

Bai, X.-N. et al. (2015). "Magnetohydrodynamic-particle-in-cell Method for Coupling Cosmic Rays with a Thermal Plasma: Application to Non-relativistic Shocks". In: *Astrophysical Journal* 809, 55, p. 55 (cit. on p. 35).

Birdsall, C. K. and D. Fuss (1969). "Clouds-in-clouds, clouds-in-cells physics for many-body plasma simulation". In: *Journal of Computational Physics* 3, pp. 494–511 (cit. on p. 36).

Harned, D. S. (1982). "Quasineutral hybrid simulation of macroscopic plasma phenomena". In: *Journal of Computational Physics* 47, pp. 452–462 (cit. on p. 36).

Takizuka, T. and H. Abe (1977). "A binary collision model for plasma simulation with a particle code". In: *Journal of Computational Physics* 25, pp. 205–219 (cit. on pp. 37, 45, 46, 51).

Braginskii, S. I. (1965). "Transport Processes in a Plasma". In: *Reviews of Plasma Physics* 1, p. 205 (cit. on pp. 37, 38).

Cottrill, L. A. et al. (2008). "Kinetic and collisional effects on the linear evolution of fast ignition relevant beam instabilities". In: *Physics of Plasmas* 15.8, 082108, p. 082108 (cit. on p. 38).

Hao, B. et al. (2009). "Relativistic collisional current-filamentation instability and two-stream instability in dense plasma". In: *Physical Review E* 79.4, 046409, p. 046409 (cit. on p. 38).

Bhatnagar, P. L., E. P. Gross, and M. Krook (1954). "A Model for Collision Processes in Gases. I. Small Amplitude Processes in Charged and Neutral One-Component Systems". In: *Physical Review* 94, pp. 511–525 (cit. on p. 38).

Fried, B. D., A. N. Kaufman, and D. L. Sachs (1966). "Low-Frequency Spatial Response of a Collisional Electron Plasma". In: *Physics of Fluids* 9, pp. 292–298 (cit. on p. 38).

Opher, M., G. J. Morales, and J. N. Leboeuf (2002). "Krook collisional models of the kinetic susceptibility of plasmas". In: *Physical Review E* 66.1, 016407, p. 016407 (cit. on p. 38).

Baalrud, S. D., C. C. Hegna, and J. D. Callen (2009). "Instability-Enhanced Collisional Friction Can Determine the Bohm Criterion in Multiple-Ion-Species Plasmas". In: *Physical Review Letters* 103.20, 205002, p. 205002 (cit. on p. 38).

Hershkowitz, N., C.-S. Yip, and G. D. Severn (2011). "Experimental test of instability enhanced collisional friction for determining ion loss in two ion species plasmas a)". In: *Physics of Plasmas* 18.5, 057102, p. 057102 (cit. on p. 38).

Ryutov, D. D. et al. (2014). "Collisional effects in the ion Weibel instability for two counter-propagating plasma streams". In: *Physics of Plasmas* 21.3, 032701, p. 032701 (cit. on p. 38).

Fitzpatrick, R. (2014). *Plasma Physics: An Introduction*. CRC Press. ISBN: 9781466594272. URL: https://books.google.fr/books?id=5HbSBQAAQBAJ (cit. on p. 39).

Trubnikov, B. A. (1965). "Particle Interactions in a Fully Ionized Plasma". In: *Reviews of Plasma Physics* 1, p. 105 (cit. on pp. 45, 52, 57).

Nanbu, K. (1997). "Theory of cumulative small-angle collisions in plasmas". In: *Physical Review E* 55, pp. 4642–4652 (cit. on p. 45).

Wang, C. et al. (2008). "Particle simulation of Coulomb collisions: Comparing the methods of Takizuka & Abe and Nanbu". In: *Journal of Computational Physics* 227, pp. 4308–4329 (cit. on pp. 45, 46, 53).

Dimarco, G. et al. (2015). "Numerical methods for plasma physics in collisional regimes". In: *Journal of Plasma Physics* 81.1, 305810106, p. 013006 (cit. on p. 45).

Sherlock, M. (2008). "A Monte-Carlo method for coulomb collisions in hybrid plasma models". In: *Journal of Computational Physics* 227, pp. 2286–2292 (cit. on p. 45).

Nanbu, K. and S. Yonemura (1998). "Weighted Particles in Coulomb Collision Simulations Based on the Theory of a Cumulative Scattering Angle". In: *Journal of Computational Physics* 145, pp. 639–654 (cit. on pp. 45, 51).

Landau (1965). "The transport equation in the case of Coulomb Interactions". In: *Collected Papers of L.D. Landau*. Ed. by D. TER HAAR. Pergamon, pp. 163 –170. ISBN: 978-0-08-010586-4. URL: http://www.sciencedirect.com/science/article/pii/B9780080105864500298 (cit. on p. 46).

Miller, R. H. and M. R. Combi (1994). "A Coulomb collision algorithm for weighted particle simulations". In: *Geophysical Research Letters* 21, pp. 1735–1738 (cit. on p. 51).

Rax, J. M. (2005). *Physique des plasmas - Cours et applications: Cours et applications*. Physique. Dunod. ISBN: 9782100527878. URL: http://books.google.fr/books?id=NIxAWzy4T9oC (cit. on p. 58).

Nanbu, K. and Y. Kitatani (1995). "An ion-neutral species collision model for particle simulation of glow discharge". In: *Journal of Physics D Applied Physics* 28, pp. 324–330 (cit. on p. 59).

Vahedi, V. and M. Surendra (1995). "A Monte Carlo collision model for the particle-in-cell method: applications to argon and oxygen discharges". In: *Computer Physics Communications* 87, pp. 179–198 (cit. on p. 59).

Chapter 4

Collisionless magnetic streaming instability

> Reality is that which, when you stop believing in it, doesn't go away.
>
> Philip K. Dick - I Hope I Shall Arrive Soon (1985), Philip K. Dick.

Contents

As explained in chapter chapter 2, instabilities can arise in magnetized plasmas when different plasma populations are streaming through each other. These instabilities feed on the beam kinetic energy to drive the non-linear growth of electromagnetic perturbations, resulting in enhanced wave activity and heating of the plasma.

In this chapter, we first present an introduction to previous studies about the magnetic streaming instability, then we present numerical results of the magnetic streaming instability in different cases. Section 4.2 will present numerical results for the resonant cases, section 4.3 will address the non-resonant case, section 4.4 will investigate a case with a mix of two competing modes. Section 4.5 investigates the effects of the plasma temperature on the instability and in section 4.6 we study the influence of the particle mass. Finally in section 4.7 we discuss the results presented in the chapter.

4.1 Introduction

Previous studies on magnetic streaming instability showed the effects of the instability through both analytical and numerical work. See for example Gary 1991 for a review of the analytical works and Gary 1993 for a detailed calculation of the linear theory for all the configurations of streaming instabilities: electrostatic and electromagnetic modes, propagation parallel and perpendicular to the ambient magnetic field, electronic and ionic modes. Winske and Leroy 1984 performed a comparison between numerical simulations and analytical results, and Wang and Lin 2003 focused on the separation of the evolution of the instability into different phases and their specificities, using computer simulations similar to those presented here. During the early stage of the instability, described by the linear theory (section 2.6.1 that gives some of these results), a perturbation in the magnetic field B_1 grows exponentially as $B_1(t) \propto \exp^{\gamma t}$ with γ the growth rate. During this period, the particles of the beam experience pitch-angle scattering, that transforms particle velocity parallel to the magnetic field into perpendicular velocity. A quasi-linear theory has been developed that gives some informations about the energy exchanges rates during this stage of the instability. After the linear stage, the perturbed magnetic field saturates reaching a maximum, and then stabilizes to lower amplitude waves.

4.1.1 Linear and quasilinear theory

Linear theory as presented in section 2.7 deals with the early stage of the instability and gives information about the excited wavelengths k and the growth rate of the instability $\gamma(k)$ by solving the dispersion relation (equation 2.18). For reference, figures 2.4 and 2.6 show the solution of this equation under different conditions. Although a range of k is unstable (with a $\gamma > 0$), there is for each mode a specific wavenumber k_{max} that maximizes the growth rate given by γ_{max}. Winske and Leroy 1984 provides simple approximated expressions for γ_{max} and k_{max}. The analytical results show the presence of three different unstable modes, corresponding to different kind of MHD waves and having specific polarization and direction of propagation. We will use the terminology

first employed by Gary 1991 to distinguish these modes. There are two resonant modes, that are either right-hand polarized (right-hand resonant, RHR) or left-hand polarized (left-hand resonant, LHR). These are presented in details in section 4.2.2) and section 4.2.3 respectively.

The other mode is non-resonant (NR) (section 4.3) and it is also described as "fluid-like" in some of the literature. It originates from the force between the current driven by the beam and the magnetic field (see Bell 2004). Depending on the physical plasma conditions, these modes can either coexist and compete or one of the modes may dominate the dynamics.

While the linear theory was found by keeping only the first order terms in the linearization of the Vlasov equation, quasilinear theory (or second order theory, developed in Gary and Feldman 1978) keeps the second order terms for the perturbed quantities and focuses on the evolution of spatially averaged quantities (such as temperature, momentum, etc). Quasi-linear theory provides expressions of the momentum $\mathbf{p}_s$ and energy E_s exchanges (with $s = m, b, e, f$ for respectively the main, the beam, the electrons and the electromagnetic field) and it is valid under the same conditions as linear theory. Results of quasi-linear theory were compared with computer simulation, for example by Gary and Tokar 1985. In addition Winske and Leroy 1984 gives simple expressions of some results of this theory for the RHR and the NR modes in the cold plasma approximation. In the following we summarize some of these results. We note p_s the plasma momentum, E_s the total energy, $E_{\parallel,s}$ the energy in the direction parallel to the magnetic field and $E_{\perp,s}$ the perpendicular energy for a given species s.

For the RHR mode the beam momentum is transferred mostly to the main plasma, and not to the waves or to the electrons ($\dot{\mathbf{p}}_m \approx -\dot{\mathbf{p}}_b$). Also, the beam loses little energy during the quasilinear phase, instead the energy goes primarily in the perpendicular direction ($\dot{\mathbf{E}}_{b,\parallel} \approx -\dot{\mathbf{E}}_{b,\perp}$), which corresponds to a pitch-angle scattering, and the energy gained by the main plasma also goes mainly in the perpendicular direction ($\dot{\mathbf{E}}_m \approx \dot{\mathbf{E}}_{m,\perp}$ as $\dot{\mathbf{E}}_{m,\parallel} \approx 0$)

For the NR mode, the beam momentum also goes to the momentum of the main plasma ($\dot{\mathbf{p}}_m \approx -\dot{\mathbf{p}}_b$), but its kinetic energy is largely transferred to the parallel direction ($\dot{\mathbf{E}}_{b,\parallel} \neq -\dot{\mathbf{E}}_{b,\perp}$), which means there is little or no pitch-angle scattering for the NR mode. The main plasma, as in the RHR case, is energized in the perpendicular direction ($\dot{\mathbf{E}}_m \approx \dot{\mathbf{E}}_{m,\perp}$) and the amount of energy going into the main plasma is comparable to the amount of energy that drive the growth of the electromagnetic fields ($\dot{\mathbf{E}}_m \approx \dot{\mathbf{E}}_f$). Winske and Leroy 1984 also showed that the NR mode is less able to disrupt the beam for a given wave amplitude, and that the compression of the plasma due to the instability is expected to be more important in the NR mode than in the RHR.

4.1.2 Previous numerical results

Linear and quasi-linear theory provide very little or no information on the saturation of the instability and its non-linear evolution. To move beyond linear and quasi-linear theory, it is therefore necessary to solve the full time-dependent Vlasov equation numerically. There are several ways to solve the Vlasov equation numerically. One of the most widely used methods is the Particle-In-Cell approach (see 3.1.1 and Lapenta 2012), which consists in solving the Vlasov equation for discrete parts of the distribution function, rep-

resented by so-called "macroparticles". For them one then solves the equations of motion, corresponding to the second and third terms of the Vlasov equation. The electromagnetic fields are then updated on the grid using the information inferred from the "macroparticle" position.

Works such as Winske and Leroy 1984, Onsager, Winske, and Thomsen 1991 or Wang and Lin 2003 performed numerical simulations with hybrid codes (such as the one presented in section 3.2) to compare the linear phase with theoretical predictions, such as the instability growth rate or the wavelengths of maximum growth. As predicted, an initial perturbation, which can be either provoked by numerical noise due to the finite number of macroparticles, or imposed, grows exponentially at the values of k close to the ones given by the dispersion relation.

Akimoto et al. 1993 performed a comparative study of the nonlinear effects of the RHR and the NR modes using computer simulations and found that after the linear growth, the perturbation saturates at a certain level B_{max}, then relaxes to a lower level of perturbation in a steady-state. During this saturation, electromagnetic fields become high enough for the energy to be exchanged with the particles and the beam then experiences a strong slowing down as well as a heating. This chapter presents our own numerical results for different plasma conditions.

4.1.3 Method to separate the polarizations

As there are cases where several modes can coexist, sometimes with very similar growth rates (see figure 2.6), we need a way to distinguish and possibly study the effects of each mode separately. Each mode has either a different polarization or a different direction of propagation (sense of rotation of the magnetic field in time) than the other modes, so separating the polarizations can allow us to identify these modes. To separate differently polarized transverse waves, we use a method developed in Terasawa et al. 1986 that we present in this section.

In the following, we consider an electromagnetic wave travelling along a mean magnetic field $\mathbf{B}_0$ that is set along the x axis ($\mathbf{B}_0 = B_0\mathbf{x}$), with transverse magnetic field components B_y and B_z. According to the terminology used in Gary 1991, we call *magnetic helicity* (hereafter just *helicity*) the sense of rotation of the transverse magnetic field in space at a given time (the "twist" of the magnetic field) and *polarization* the sense of rotation in time at a given point. We thus distinguish the positive helicity with:

$$\frac{B_y}{B_z} = \imath \tag{4.1}$$

and the negative helicity with:

$$\frac{B_y}{B_z} = -\imath \tag{4.2}$$

However helicity and polarization are not independent and can be linked through the direction of propagation of the wave for linear modes: two waves with the same polarization, but propagating in opposite directions will have opposite helicities. Similarly, two wave propagating in the same direction but with different polarization will also have

	$v_\phi > 0$ ($k_\parallel > 0$)	$v_\phi < 0$ ($k_\parallel < 0$)
Positive helicity	right pol.	left pol.
Negative helicity	left pol.	right pol.

Table 4.1: Summary of the polarizations relative to the helicities and directions of propagation.

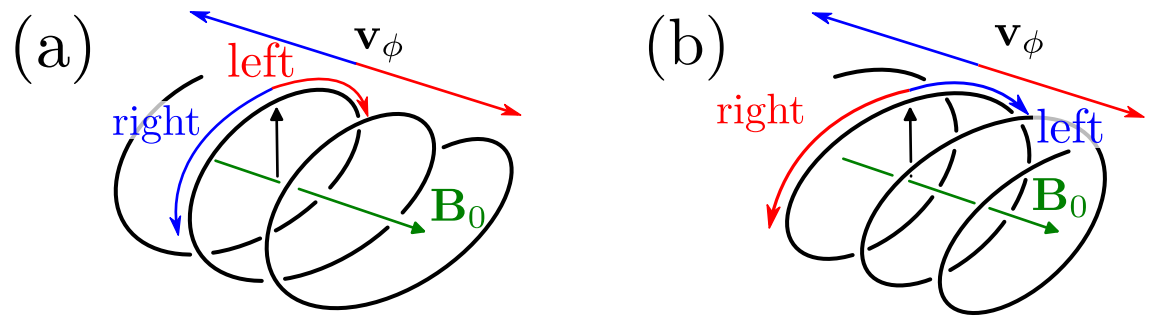

Figure 4.1: **(a)**: draw of a negative helicity: when propagating in the positive direction (phase value $v_\phi > 0$, red) it gives a left polarization, and when propagating in the negative direction (phase value $v_\phi < 0$, blue) a right polarization. **(b)**: draw of a positive helicity: when propagating in the positive direction (phase value $v_\phi > 0$, red) it gives a right polarization, and when propagating in the negative direction (phase value $v_\phi < 0$, blue) a left polarization.

different helicities. This is illustrated in figure 4.1. Figure 4.1 panel **(a)** shows in black a wave with negative helicity. When propagating in the positive direction (with a positive phase speed $v_\phi > 0$) it induces a left polarization (shown in red), and when propagating in the negative direction ($v_\phi < 0$, shown in blue) it induces a right polarization. Similarly, figure 4.1 panel **(b)** shows that a wave with positive helicity, that induces a right polarization when $v_\phi > 0$ (red) and a left polarization when $v_\phi < 0$ (blue). Table 4.1 summarizes these relationships. In the following sections, the real part of the frequency will always be positive ($\omega > 0$) so that when $v_\phi = \omega/k_\parallel > 0$ then $k_\parallel > 0$ and consequently when $v_\phi < 0$ then $k_\parallel < 0$. We now describe in more details the method we have used to separate the different helicities at a given time.

For a transverse wave propagating in the x direction ($\mathbf{k} = k_x\mathbf{x}$), the perturbation is in general a combination of right-hand and left-hand polarized waves. From 4.1 and 4.2 we write the expressions of the complex magnetic profiles associated with the positive (B^+) and negative (B^-) helicities:

$$B^+(x) = \frac{B_y(x) + \imath B_z(x)}{2} \tag{4.3}$$

$$B^-(x) = \frac{B_y(x) - \imath B_z(x)}{2} \tag{4.4}$$

and since $e^{-\imath kx} = \cos(kx) - \imath\sin(kx)$ we get:

$$\begin{aligned}
\hat{B}(k) &= \int B(x)e^{-\imath kx}dx && (4.5)\\
&= \int B(x)\left[\cos(kx) - \imath\sin(kx)\right]dx && (4.6)\\
&= \left(\int B(x)\cos(kx)dx\right) - \imath\left(\int B(x)\sin(kx)dx\right) && (4.7)\\
&= \hat{B}^c(k) - \imath\hat{B}^s(k) && (4.8)
\end{aligned}$$

where $\hat{B}$ is the Fourier transform of the B component of the magnetic field, and $\hat{B}^c$ and $\hat{B}^s$ are respectively the cosine and sine transforms of the magnetic profile B. From these equations we get:

$$\begin{aligned}
\hat{B}^+(k) &= \frac{\hat{B}_y(k) + \imath\hat{B}_z(k)}{2} && (4.9)\\
&= \frac{1}{2}\left[\left(B_y^c(k) - \imath B_y^s(k)\right) + \imath\left(B_z^c(k) - \imath B_z^s(k)\right)\right] && (4.10)\\
&= \frac{1}{2}\left[\left(B_y^c(k) + B_z^s(k)\right) + \imath\left(B_z^c(k) - B_y^s\right)\right] && (4.11)
\end{aligned}$$

where $B_y^s(k)$, $B_y^c(k)$, $B_z^s(k)$ and $B_z^c(k)$ are the sine (s upper-script) and cosine (c upper-script) transforms of both transverse components ($B_y(x)$ and $B_z(x)$) of the magnetic field profile. The same goes for the negative helicity so that:

$$\begin{aligned}
B^+(k) &= \frac{1}{2}\left[\left(B_y^c(k) + B_z^s(k)\right) + \imath\left(B_z^c(k) - B_y^s(k)\right)\right] && (4.12)\\
B^-(k) &= \frac{1}{2}\left[\left(B_y^c(k) - B_z^s(k)\right) + \imath\left(B_z^c(k) + B_y^s(k)\right)\right] && (4.13)
\end{aligned}$$

which is the method developed in Terasawa et al. 1986 used to separate the helicities. We then use the Fourier modes to recreate both profile profiles containing either only positive or negative helicity:

$$\begin{aligned}
B^+(x) &= \sum_{k=0}^{k_{max}}\left[B^r(k)e^{\imath kx}\right] && (4.14)\\
B^-(x) &= \sum_{k=0}^{k_{max}}\left[B^l(k)e^{-\imath kx}\right] && (4.15)
\end{aligned}$$

The real and imaginary parts of these expressions then correspond to respectively the B_y and B_z components of the profiles:

$$B_y^+(x) = \mathrm{Re}\left(B^+(x)\right) \tag{4.16}$$
$$B_z^+(x) = \mathrm{Im}\left(B^+(x)\right) \tag{4.17}$$
$$B_y^-(x) = \mathrm{Re}\left(B^-(x)\right) \tag{4.18}$$
$$B_z^-(x) = \mathrm{Im}\left(B^-(x)\right) \tag{4.19}$$

Since we deal with electromagnetic waves having different characteristics (polarization and direction of propagation), we will be able to separate the effects of each mode on the waves using this method. In particular, we will be able to separate two modes propagating in the same direction and have opposite polarizations, or the same polarization but different direction of propagation. However we will not be able to separate modes that have opposite polarizations and opposite directions of propagation at the same time, since they correspond to the same helicity. As there is no way of separating the effects of the modes on the particles (such as the compression of the waves, or the energy exchanges), it remains interesting to study cases where each mode largely dominates.

4.2 Numerical results for the resonant modes

In this chapter, we will present the results of numerical simulations performed within the framework of a collisionless plasma. These results will be compared to and will also help to better understand the simulation results presented in the next chapter where ion-ion collisions are included. We initialize the computational domain with parameters such that one of the modes (RHR, LHR or NR) dominates so it can be studied alone, and also present a simulation with a coexistence of the RHR and the NR modes. These parameters are summarized in table 4.2. For each mode, a comparison with linear theory is presented and the main features of the modes are explained. In particular, we will identify the k_{max} and γ_{max} for each mode and compare it to linear theory. The theoretical values are taken from the analytical expressions given in Winske and Gary 1986, the dispersion relation in the cold plasma approximation (Winske and Gary 1986) and the dispersion relation in the general case.

4.2.1 Introduction to resonant modes

Resonant modes originate from the cyclotron resonance between the particles of the beam and the waves propagating in the main plasma. As explained in 2.6.2 and Schure et al. 2012, the driving force of this instability comes from the first-order component of the current density $\mathbf{j}_1 \times \mathbf{B}_0$. Tsurutani and Lakhina 1997 gives an illustrated explanation of the resonant process with application to solar wind particles in the earth magnetic field. For a given drift velocity of the beam, there are two different possible resonances which have opposite polarization, depending if the wave propagates faster or slower than the bulk velocity of the beam, according to the Doppler shift applied to the frequency: $\omega - kv_{\parallel} = \omega*$

case	n_b/n_m	V_b/V_0	$v_{T,b}/V_0$	$v_{T,m}/V_0$	m_m/m_p	m_b/m_p	β_b	β_m
RHR (4.2.2)	0.01	10	1	1	1	1	0.02	2
LHR (4.2.3)	0.01	10	60	1	1	1	72	2
NR (4.3)	0.016	57	1	1	1	1	0.032	2
mixed (4.4)	0.1	10	1	1	1	1	0.2	2
mixed (4.5.1)	0.1	10	0.1 - 10	1	1	1		2
mixed (4.5.2)	0.1	10	1	0.1 - 10	1	1	0.2	
mixed (4.6)	0.1	10	1	1	1 - 20	1	0.2	2
mixed (4.6)	0.1	10	1	1	1	1 - 20	0.2	2

Table 4.2: Parameters used for the different cases in the collisionless study. Here $v_{T,s} = \sqrt{\beta_s B^2/(2n_s m_s)}$.

where ω and k are the frequency and wavenumber of the wave in a given frame, $v_\parallel$ the particle velocity component parallel to k in this frame and $\omega*$, is the frequency experienced by this particle. A wave with positive helicity propagating slower than the beam will be experienced as propagating backward by the particles of the beam, and therefore they will see it as left polarized (as explained in figure 4.1 **(b)**). In the opposite case, a wave with negative helicity and phase speed higher than the beam velocity will by seen as left polarized by the particles of the beam (see figure 4.1 **(a)**). In both cases, the particles experience a left polarization, and since it corresponds to the cyclotron motion of the ions around the magnetic field, they are able to resonate with the waves.

The dispersion relation 2.14 gives a condition involving waves and particles that must be fulfilled for the resonance to take place:

$$\omega - k_\parallel v_\parallel \pm \Omega_C = 0 \tag{4.20}$$

where ω and $k_\parallel$ are respectively the frequency and the wave vector parallel to the magnetic field, $v_\parallel$ the speed of a particle and Ω_C the cyclotron frequency, with the frequency of the wave being negligible compared to the cyclotron frequency ($\omega \ll \Omega_C$). This condition states that the frequency experienced by the particle in its frame considering the Doppler correction ($\omega - k_\parallel v_\parallel$) must be equal to the cyclotron frequency. The sign $\pm$ depends on the polarization of the mode, giving birth to two modes that are oppositely polarized (the right and left-hand modes). These two modes produce waves that travel in the same direction of the beam: $\mathbf{k}.\mathbf{B} > 0 \Rightarrow k_\parallel > 0$. The following sections will describe the right (subsection 4.2.2) and left (subsection 4.2.3) resonant mode, focusing on their specificities.

4.2.2 Right-hand resonant mode

We present here results for the RHR mode. This mode produces right-hand polarized waves that propagate in the same direction as the beam. It comes from a cyclotron resonance between the waves and the particles of the beam, and arises when the beam is relatively cold, meaning, its thermal speed is much lower than its drive speed: $v_{T,b} \ll V_b$. This is shown schematically in figure 4.2, for a typical initial distribution function $f(v_\parallel)$,

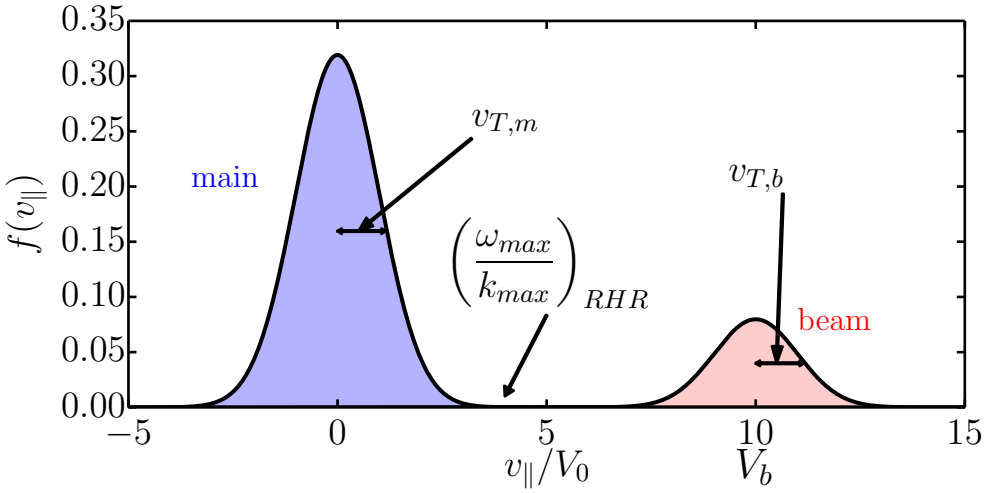

Figure 4.2: Distribution function $f(v_\parallel)$ associated to the RHR mode, integrated over the space and the perpendicular velocities. The blue population is the main plasma and the red one, shifted of a velocity V_b is the beam. The beam is relatively cold, with $v_T \ll V_b$.

which has been averaged over space and the velocity perpendicular to the initial magnetic field. In the figure, the beam is shown in red and the main plasma is in blue. This mode follows the right-hand resonance condition (+ sign) written in equation 4.20 and corresponds to magnetosonic branch of the dispersion relation when there is no drift. It dominates for very low densities of the beam.

A particle is able to resonate with a right-hand polarized wave when it moves in a frame where the magnetic field is rotating in the same direction and at the same frequency as its cyclotron motion. In that case, the plasma dispersion function in the cold case (equation 2.21) has a singularity when the resonance condition is satisfied. The resonance condition, when considering waves propagating along the initial magnetic field, is given by:

$$\omega - k_\parallel v_\parallel + \Omega_C = 0 \tag{4.21}$$

where ω and k the frequency and wave number of the wave and $v_\parallel$ the velocity of the resonating particle parallel to the magnetic field. The electromagnetic field experienced by the particle is thus the phase speed of the wave Doppler shifted by the cyclotron frequency which writes:

$$\frac{\omega + \Omega_C}{k_\parallel} = v_\parallel \tag{4.22}$$

and we can calculate the actual phase speed of the resonating wave as:

$$\frac{\omega}{k} = v_\parallel - \frac{\Omega_C}{k} = v_\parallel - \frac{\Omega_C}{k} < v_\parallel \tag{4.23}$$

We can check that, as explained before, the wave propagates more slowly than the particle it resonates with. We consider a situation in which this mode largely dominates, as

presented in section 2.7.1. The simulation parameters are $n_b/n_m = f = 0.01$ and $V_b/V_0 = 10$, and the thermal speeds are the Alfvén speed for both species: $v_{T,m}/V_0 \approx v_{T,b}/V_0 \approx 1$. In figure 2.4 we can identify the values of ω and k that maximize γ (respectively ω_{max} and k_{max} that give γ_{max}), which are the characteristics of the wave resonating with the maximum of beam particles:

$$k_{max}\, l_i \approx 0.11 \tag{4.24}$$

$$\frac{\omega_{max}}{\Omega_C} \approx 0.3 \tag{4.25}$$

$$\frac{\omega_{max}}{k_{max}} \approx 2.7 V_A \tag{4.26}$$

$$\frac{\omega_{max} + \Omega_C}{k_{max}} \approx 11.8 V_A \approx V_b \tag{4.27}$$

As we can see, the phase speed of the wave with a shift due to cyclotron motion approximately corresponds to the fluid velocity of the beam V_b. This could be expected as the maximum growth rate γ_{max} happens for the wave resonating with the bulk of particle distribution: the particles found in the center of the beam distribution function with a parallel velocity close to the beam fluid velocity $v_\parallel \approx V_b$.

We now present typical simulation results for this mode. Figure 4.3 **(a)** shows the spatial profile of magnetic field perpendicular to $\mathbf{B}_0$ (B_y) at different times. From the first panel, we can see that the magnetic perturbation "noise" see at $\sim 5\ \Omega_0^{-1}$ rapidly grows and saturate by $\sim 40\Omega_0^{-1}$, to stabilize at later time as lower amplitude waves from around $t = 80\Omega_0^{-1}$. The magnetic perturbation is also shown in Figure 4.4 which represents in 3D both components of the transverse perturbation at different times, separated using the method described before, with the positive helicity in blue and the negative in red. We can see that the perturbation has essentially a positive helicity, which, as expected for this mode, is consistent with the resonance process explained in section 4.2. We note that negative helicity perturbations, on the other hand, remain at the same level as the initial noise. Indeed no other mode is expected to develop for the those plasma conditions, consistently with the dispersion relation in 2.4.

Figure 4.3 **(b)** shows the profiles of the beam (red) and main (blue) plasma relative densities at the same times as the magnetic profiles. We can see that the beam density presents large fluctuations, following the same evolution as the magnetic field with relative density perturbations up to $\delta n_b/n_b \approx 0.4$. The main plasma remains essentially unperturbed, with $\delta n_m/n_m < 0.05$. Figure 4.5 shows the deformation of the distribution functions (initially Maxwellian at $t = 0$, on the top panel), and more precisely the integral over the computational domain of the distribution function $f(\mathbf{x}, \mathbf{v}, t)$, giving the function $f(v_\parallel, v_\perp, t)$ where $v_\parallel$ and $v_\perp$ are the parallel and perpendicular components of the velocity with respect to the local magnetic field.The beam's particles experience pitch-angle scattering that mostly transfers parallel velocity into perpendicular velocity, creating a strong anisotropy for the beam. Pitch-angle scattering is a process that diffuses the pitch angle of the particle μ, defined as the scalar product between the particle velocity and the local magnetic field $\mu = (\mathbf{v} \cdot \mathbf{B})/(|\mathbf{v}||\mathbf{B}|) = \cos\theta$ where θ is the pitch-angle. After a while, during the steady-state, the beam forms a shell-like distribution which tends to a zero

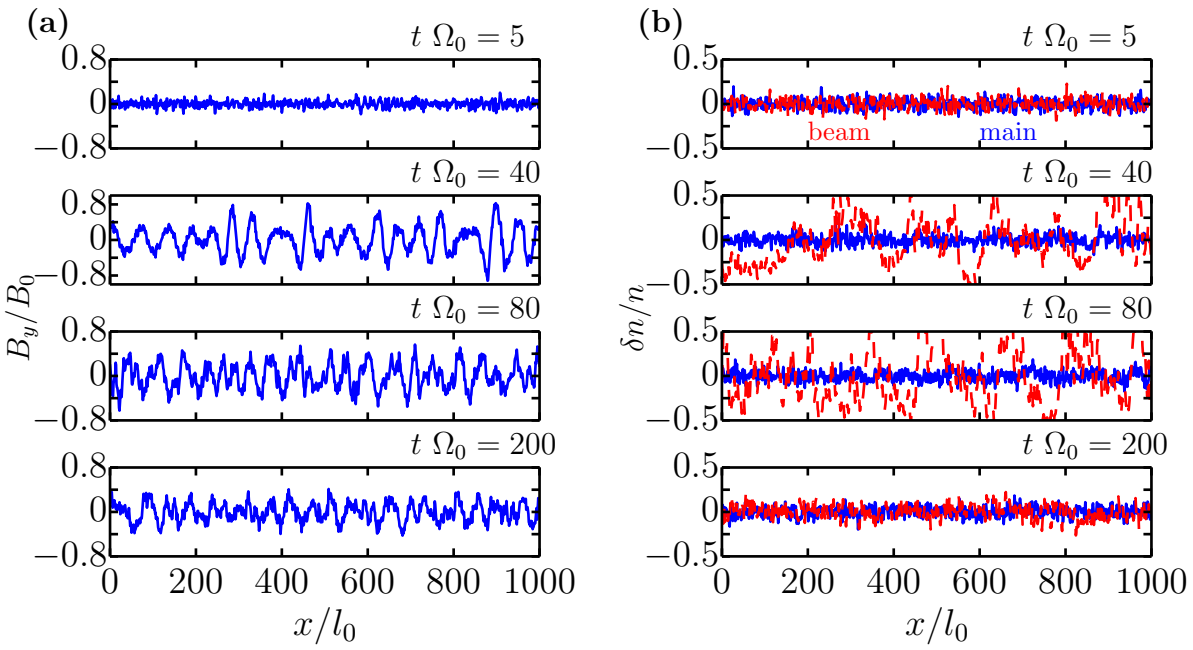

Figure 4.3: **(a)**: magnetic perturbation of one of the components perpendicular to the initial magnetic field (B_y) profiles at different times (start of the instability $t\ \Omega_0 = 5$, end of linear stage $t\ \Omega_0 = 40$, end of the second phase $t\ \Omega_0 = 80$, last stage $t\ \Omega_0 = 200$). **(b)**: relative density ($\delta n/n$) perturbation profiles for the main plasma (blue) and the beam (red) at the same times as panel **(a)**.

mean velocity. We can observe that the beam doesn't populate the center of the plane where the main plasma is (an effect which we have not understood yet), and that the main plasma distribution experiences little change during the instability. Indeed we see no heating and no development of anisotropy for the main plasma, which suggests that there is very little energy exchanged between both populations, at least in the absence of collisions.

4.2.2.1 Time evolution of the instability

We can identify more precisely the different phases of the evolution of the instability. Figure 4.6 **(a)** shows the the magnetic perturbation perpendicular to the initial magnetic field $B_\perp$ averaged over the domain as a function of time. We distinguish three different phases for the evolution of the perturbation:

1. The first stage (from $t = 0$ to $t\ \Omega_0 = 32$) is the *linear phase*, where linear theory applies. During this phase, the ions of the beam experience a cyclotron resonance with some of the waves and are then able to exchange energy with them. The initial magnetic field perturbations, which are due to the noise created by the finite number of macroparticles, grow exponentially with a rate γ, and saturate to a maximum level B_{max} before reaching a steady level of fluctuation amplitude. According to linear theory, a range of wave numbers, k, are unstable and experience exponential

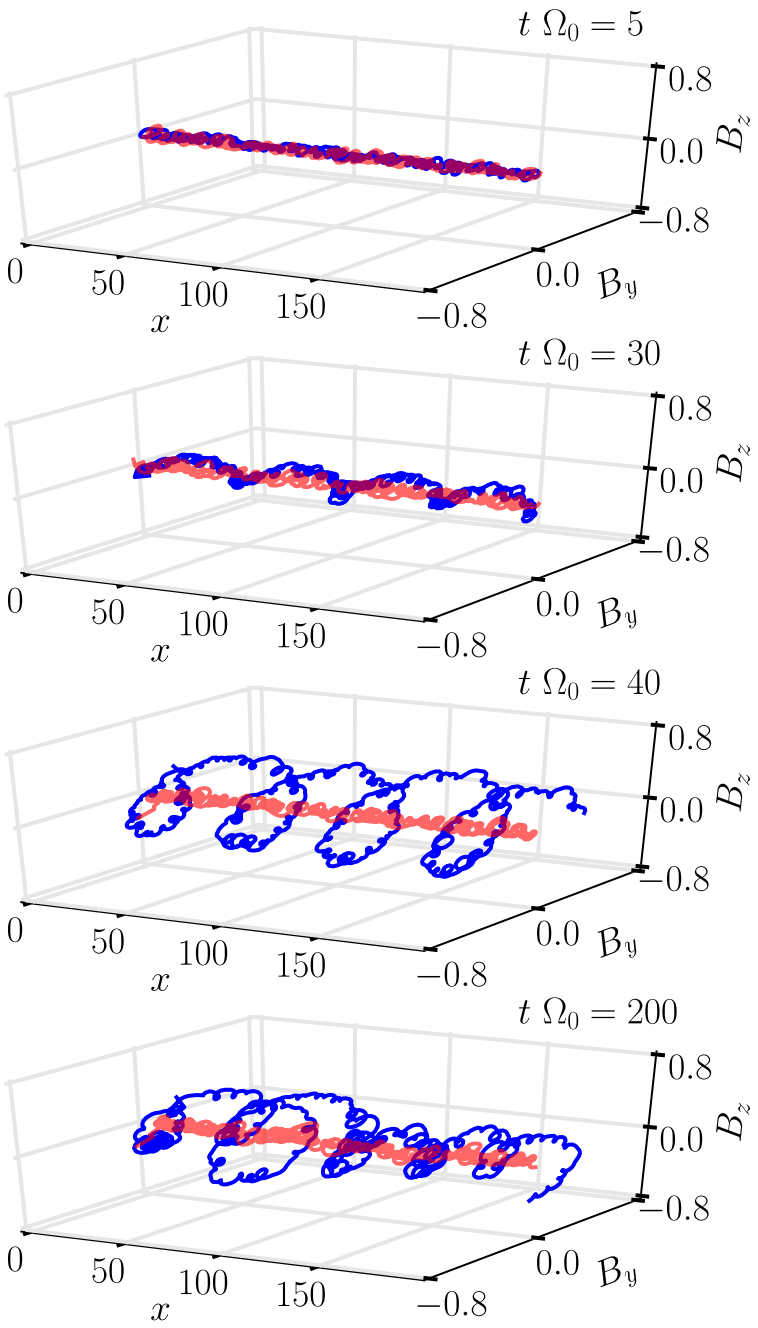

Figure 4.4: Perturbed magnetic field components (B_y, B_z) as a function of x for the positive (blue) and negative (red) helicities (the blue line thus corresponds to the RHR mode), for the times: start of the instability ($t\ \Omega_0 = 5$), linear phase ($t\ \Omega_0 = 30$), saturation ($t\ \Omega_0 = 40$), steady-state ($t\ \Omega_0 = 200$).

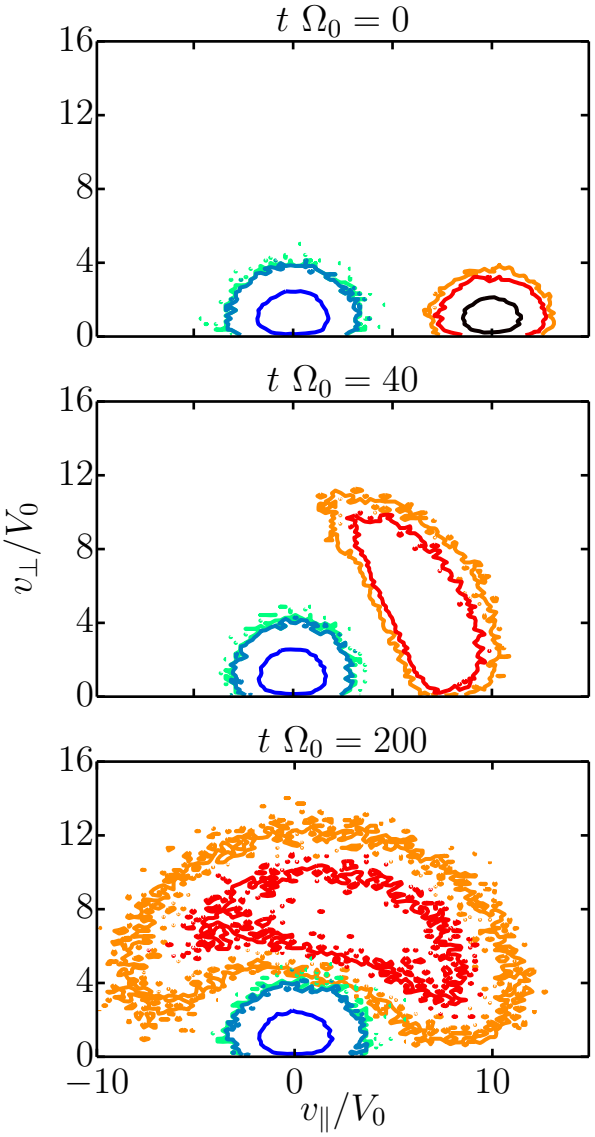

Figure 4.5: Contours of the distribution function integrated over the domain $f(v_\parallel, v_\perp)$ in the plane $v_\parallel/v_\perp$, velocities parallel and perpendicular to the local magnetic field for the RHR case. The blue color scale is the main plasma and the red one corresponds to the beam. The different panels correspond to different stages of the instability: the initial state ($t\ \Omega_0 = 0$), the end of linear phase ($t\ \Omega_0 = 40$) and steady-state ($t\ \Omega_0 = 200$).

growth. In the resonant case, this range is narrow and shows a k_{max} with a maximum growth rate γ_{max}. As shown in Winske and Leroy 1984, the expected growth rate for the resonant mode can be estimated by:

$$\frac{\gamma_{max}^{RHR}}{\Omega_0} = \left(\frac{f}{2}\right)^{1/3} \tag{4.28}$$

$$\frac{k_{max}^{RHR}}{l_0} = \frac{V_0}{V_b} \tag{4.29}$$

This gives $\gamma_{R,max}^{(th)}/\Omega_0 \approx 0.17$ for a cold plasma, which is close to the value obtained from the numerical simulations $\gamma_R^{(num)}/\Omega_0 \approx 0.10$. The numerical growth rate $\gamma^{(num)}$ is calculated from the evolution of the magnetic perturbation as

$$\gamma^{(num)} = \frac{\log(B(t_2)/B(t_1))}{t_2 - t_1} \tag{4.30}$$

where t_1 and t_2 are the start and end of the linear phase. Figure 4.6 **(b)** shows Fourier transforms of the profiles presented in figure 4.6 **(a)**. The magnetic spectral energy densities ($(B_y(k)/B_0)^2$) are shown for several times. The initial energy (blue line) is seen to evolve (red line) to favour wavenumbers close to the fastest growing value predicted by linear theory $k_{\max}\ c/\omega_p = 0.10$. We note that the energy at late times, well after the linear phase (green curve), indicates that the perturbed magnetic energy is still mostly concentrated in waves with wavenumbers close to k_{max} and then it rapidly decreases for shorter wavelengths.

2. The second phase of the instability, which roughly corresponds to the interval $t\ \Omega_0 = 32$ to $t\ \Omega_0 = 80$) includes the saturation of the perturbation to its maximum value $B_{max} = \delta B_\perp / B_0 \approx 0.42$ and the initial relaxation towards the third phase. During this phase the peak in energy observed in the spectral energy decreases by about a factor ten to about the level seen in figure 4.6 **(b)** for later times.

3. In the last phase (after $t\ \Omega_0 = 80$) the amplitude of the perturbed magnetic field decreases until the end of the simulation. During this phase, the beam particles keep populating the region around the main plasma empty of beam particles.

4.2.2.2 Energy budget

We now look in more details at the temporal evolution of the different energies present in the system. Before presenting the results, we give their definitions:

(i) magnetic energy

$$E_B(t) = \frac{1}{2\mu_0}\left[\int B(\mathbf{x},t)d^3x\right]^2 \tag{4.31}$$

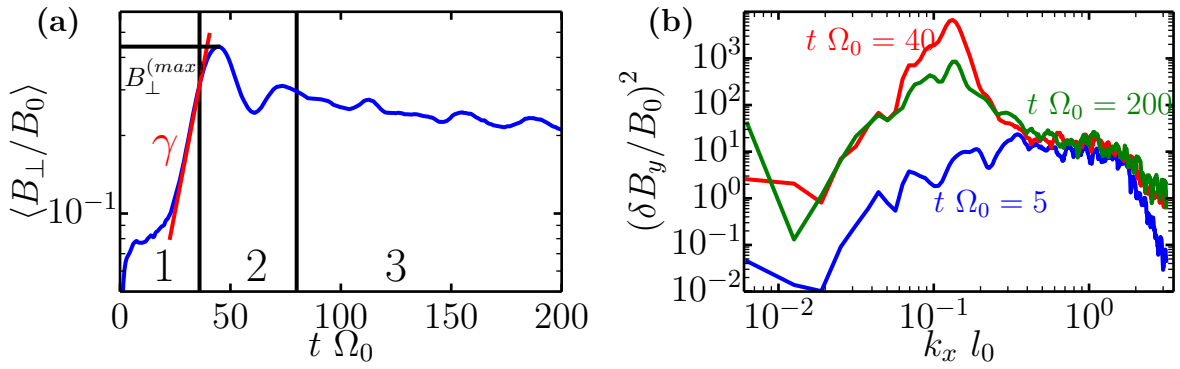

Figure 4.6: **(a)**: evolution of the magnetic perturbation $B_\perp/B_0$ with time with the separation of the three stages of the instability: 1 - the linear stage, 2 - the saturation, 3 - the asymptotic stage. We can see the value of the saturation B_{max} and the slope in the linear stage (in red) that corresponds to the linear growth rate γ. **(b)**: Fourier transforms of the magnetic profiles of figure 4.3 **(a)** (spectral energy densities, $(\delta B_y(k_x)/B_0)^2$. The lines are smoothed with a Gaussian profile which variance increases linearly with the value of k.

(ii) kinetic energy of species s

$$E_{k,s} = \frac{m_s}{2}\left[\int \mathbf{v} f_s(\mathbf{x},\mathbf{v},t)\, d^3v d^3x\right]^2 \tag{4.32}$$

(iii) thermal energy of species s

$$\begin{aligned} E_{T,s} &= \frac{m_s}{2}\int (\mathbf{v}-\mathbf{V}_s)^2 f_s(\mathbf{x},\mathbf{v},t)\, d^3v d^3x && (4.33)\\ &= E_{T,\parallel,s} + E_{T,\perp,s} && (4.34)\\ &= k_B T_s = k_B T_{\parallel,s} + k_B T_{\perp,s} && (4.35) \end{aligned}$$

(iv) parallel component of the thermal energy

$$\begin{aligned} E_{T,\parallel,s} &= \frac{m_s}{2}\int [(\mathbf{v}-\mathbf{V}_s)\cdot\mathbf{b}]^2 f_s(\mathbf{x},\mathbf{v},t)\, d^3v d^3x && (4.36)\\ &= \frac{m_s}{2}\int \left(\mathbf{v}_\parallel - \mathbf{V}_{\parallel,s}\right)^2 f_s(\mathbf{x},\mathbf{v},t)\, d^3v d^3x && (4.37) \end{aligned}$$

(v) perpendicular component of the thermal energy

$$\begin{aligned} E_{T,\perp,s} &= \frac{m_s}{2}\int [(\mathbf{v}-\mathbf{V}_s)\cdot(\mathbf{I}-\mathbf{b})]^2 f_s(\mathbf{x},\mathbf{v},t)\, d^3v d^3x && (4.38)\\ &= \frac{m_s}{2}\int \left(\mathbf{v}_\perp - \mathbf{V}_{\perp,s}\right)^2 f_s(\mathbf{x},\mathbf{v},t)\, d^3v d^3x && (4.39) \end{aligned}$$

where $\mathbf{b} = \mathbf{B}/|\mathbf{B}|$ is the unit vector directed along the local magnetic field, and $v_\parallel$ and $v_\perp$ are the velocities respectively parallel and perpendicular to $\mathbf{b}$. Figure 4.7 panel **(a)**

shows these energies as a function of time. We stress, that the total energy is conserved accurately throughout the simulation (less than $10^{-2}\%$ of total energy loss).

As we can see, the beam speed decreases strongly, giving its kinetic energy to the thermal energy of the beam for the most part and to the magnetic field. The energy first goes into the waves, then contributes to heat the beam after the linear phase through wave-particle interactions. A few percent of the beam energy goes into the heating of the background plasma as already observed in figure 4.5 where no significant deformation of the main distribution function is observed. This agrees with quasilinear theory (see Winske and Leroy 1984) which predicts that there is very little energy lost by the beam. This is mainly transferring velocity parallel to the magnetic field to the perpendicular direction (see section 4.1.1, $\dot{\mathbf{E}}_{b,\parallel} \approx -\dot{\mathbf{E}}_{b,\perp}$). At late times, well after saturation, the beam and main plasmas relax to the same kinetic energy. However, because of its larger density, the main plasma undergoes little acceleration and remains almost stationary. The drift velocity essentially corresponds to the beam velocity, and it is $\approx 3V_0$, and this value corresponds to a threshold according to Winske and Leroy 1984, which found that the RHR growth rate drops between $3 > V_b/V_0 > 2$ and that the mode becomes stable under $V_b = 2V_0$ (this is valid for a density ratio $f = 0.1$, but the same study shows that the growth rate does not depend much on this quantity in that case).

Looking more closely at the anisotropy in the distribution function induced by the RHR mode, figure 4.7 **(b)** shows the evolution of the temperature anisotropy $T_{\parallel,s}/T_{\perp,s}$ for the main plasma (blue) and the beam (red). For the main plasma a small anisotropy ($T_\perp > T_\parallel$) appears at a time corresponding to the growth of the magnetic field perturbation. This is consistent with the predictions of quasilinear theory that the main ions are energized preferentially in the perpendicular direction. The anisotropy however quickly disappears at later times. The beam, on the contrary, rapidly develops a much more pronounced anisotropy (with $T_\parallel/T_\perp \approx 0.2$), which is the symptom of the pitch-angle scattering. The particles form a shell in the velocity space, and the relaxation of this anisotropy takes very long; indeed $T_{\parallel,s}/T_{\perp,s}$ is still less than one at the end of the simulations. As we shall see later, the inclusion of collisions will tend to reduce the temperature anisotropy and relax the shell-like distribution function to a Maxwellian.

4.2.2.3 Results for two dimensional simulations

In order to compare the 1D and 2D cases, we ran simulations with the same physical parameters and compare the results. The 2D simulations have the same numerical parameters as for the 1D case, except the domain has length 1000×100. Figure 4.8 displays the evolution of the different energies for the 1D case (dashed lines) and the 2D case (solid lines). We can see that in 2D, the heating of the beam is almost identical to the 1D case, and that the heating of the main is slightly higher, although not in a very significant way. The magnetic field shows the same features in both cases, even if the saturation is a bit lower in the 2D case and happens a bit later. In the slowing of the beam, we can see that the 2D case does not show the plateau we observe in the 1D case, but the general trend and timescales of the development of the instability remain the same in th 1 and 2D cases. This is consistent with the work of Winske and Gary 1986, which shows that

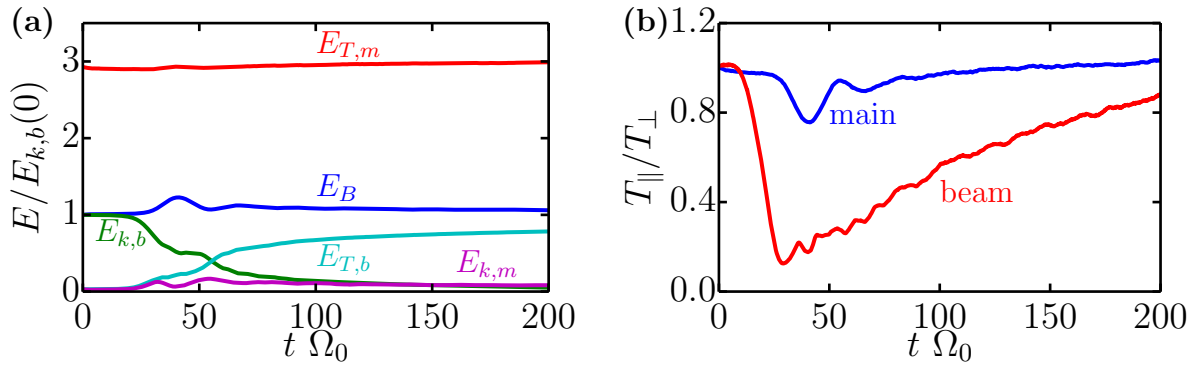

Figure 4.7: **(a)**: evolution of the different energies with time (magnetic energy E_B (blue), main plasma kinetic $E_{k,m}$ (magenta) and thermal $E_{T,m}$ (red) energies and beam kinetic $E_{k,b}$ (green) and thermal $E_{T,b}$ (cyan) energies) normalized with the initial beam kinetic energy $E_{k,b}$. **(b)**: evolution of the temperature anisotropies ($T_\parallel/T_\perp$ with $T_\parallel$ the temperature parallel to the local magnetic field and $T_\perp$ the perpendicular temperature) with time for the RHR case. The blue line corresponds to the main plasma and the red line is the beam.

2D simulations give the same results as the 1D when studying parallel propagating modes.

In conclusion, we studied the RHR mode and found that the simulation results agree well with linear and quasi-linear theory, and previous numerical work. The general development of the instability is similar for LHR and NR modes, and we shall focus in the next section on the peculiarities of those modes and their comparison to the RHR mode presented here.

4.2.3 Left-hand resonant mode

According to linear theory, particles of the beam can resonate and drive unstable left-hand polarized waves that propagate in the same direction as the beam (Rogers, Gary, and Winske 1985, Gary and Tokar 1985). In the absence of a beam these are Alfvén waves. Because the resulting waves are left-hand polarized, it is possible to separate the effects of both RHR and LHR modes on the magnetic field as explained in 4: since they have similar direction of propagation but opposite polarization, they have opposite helicities.

Contrary to the RHR mode, the LHR mode occurs for very hot beams, meaning that the beam thermal velocity is very high compared to its drift velocity $v_{T,b} \gg V_b$. This is shown schematically in figure 4.9, which shows the beam (red) and main (blue) plasmas distribution functions in the direction parallel to the initial magnetic field. Under these conditions, a non negligible portion of the beam particles are able to resonate with left-hand polarized waves. This mode is relevant for the interstellar medium for instance (as explained in Wentzel 1974, where the confinement of low energy cosmic rays in the galaxy at long timescales is investigated by considering their cyclotron resonance with waves), where even the low energy drifting cosmic rays can be very energetic. The LHR mode is described by the minus sign in the general resonance condition 4.20, which gives:

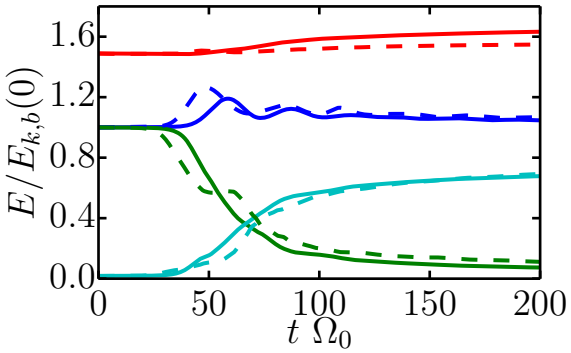

Figure 4.8: Evolution of the energies (magnetic energy E_B in blue, main plasma thermal $E_{T,m}$ (red) energy and beam kinetic $E_{k,b}$ (green) and thermal $E_{T,b}$ (cyan) energies) in 1D (dashed) and 2D (plain lines). The energies are normalized to the initial beam kinetic energy $E_{k,b}(0)$.

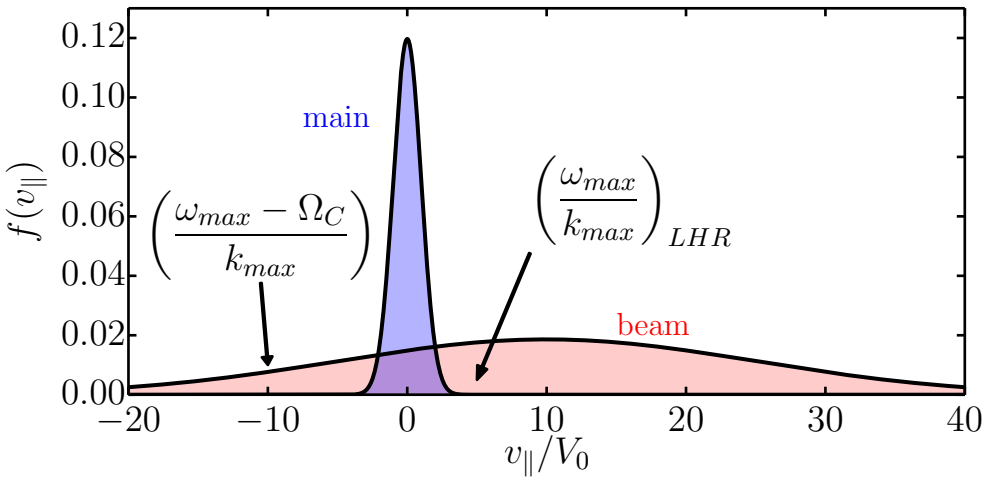

Figure 4.9: Distribution function $f(v_\parallel)$ associated to the LHR mode, integrated over the space and the velocities perpendicular to the magnetic field. The blue population is the main plasma and the red one, shifted of a velocity V_b is the beam. Here the beam is very hot, with $v_{T,b} \gg V_b$.

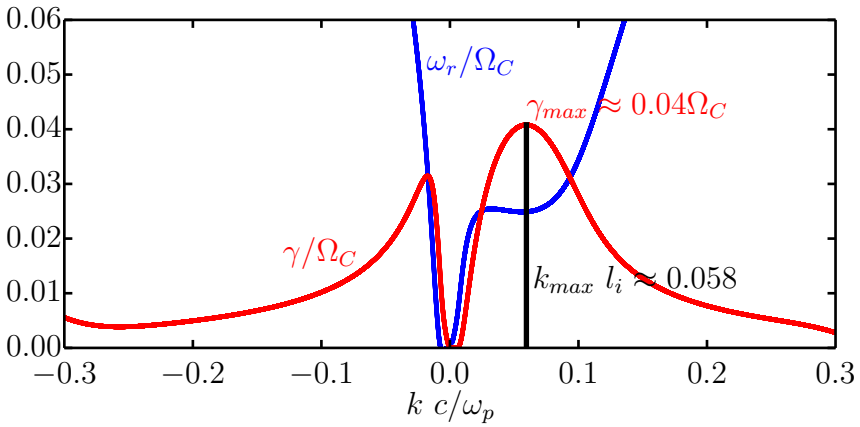

Figure 4.10: A dispersion graph ($\omega(k)$) relevant for the LHR mode with the conditions $f = 0.01$, $V_b = 10$ and $v_{T,b} = 60\ V_0$, with the real wave frequency ω_r in blue and the growth rate γ in red. It is a case we will use in section 4.2.3.

$$\omega - k_\parallel v_\parallel - \Omega_C = 0 \tag{4.40}$$

$$\frac{\omega - \Omega_C}{k_\parallel} = v_\parallel \tag{4.41}$$

$$\frac{\omega}{k} = v_\parallel - \frac{\Omega_C}{k} = v_\parallel + \frac{\Omega_C}{k} > v_\parallel \tag{4.42}$$

where ω and k the frequency and wave number of the wave and $v_\parallel$ the velocity of the resonating particle parallel to the magnetic field. We can see that the resonant wave has a phase speed higher than the velocity of the particles it resonates with. Figure 4.10 shows the dispersion graph found solving equation 2.18 with the minus sign, with the growth rate in red and the real frequency in blue, for a case where the LHR mode is present, with $f = 0.01$, $V_b = 10V_0$ and $v_{T,b} = 60V_0$. It give the characteristic of the fastest growing mode ω_{max} and k_{max}.

$$k_{max}\ l_i \approx 0.058 \tag{4.43}$$

$$\frac{\omega_{max}}{\Omega_C} \approx 0.03 \tag{4.44}$$

$$\frac{\omega_{max}}{k_{max}} \approx 0.517\ V_A \tag{4.45}$$

$$\frac{\omega_{max} - \Omega_C}{k_{max}} \approx -16.7\ V_A < 0 \tag{4.46}$$

As we are considering low frequency waves with $\omega < \Omega_C$, we have $\frac{\omega - \Omega_C}{k} < 0$ which means that the resonating particles travel backward with respect to the beam, and that

is why the beam has to be very hot to excite this mode: by increasing the variance of its distribution function we increase the population in $v_\parallel < 0$ and thus the amount of particles able to have a resonance with a negative helicity. In this case we see that the resonating waves can mostly interact with particles of the beam, and the growth rate of the LHR mode is increased by increasing the temperature of this population.

To study this mode, we run a simulation with $v_{T,b} \gg V_b$ ($v_{T,b} = 60V_0$), and the other parameters ($f = 0.01$, $V_b = 10V_0$ and $v_{T,m} = 1$) similar to the RHR mode. Under such conditions, both right and left-hand resonant modes are potentially present, however the left-hand has the fastest growth and dominates. In order to extract the evolution of the left-hand mode alone, we separate the polarizations with the method developed in Terasawa et al. 1986 and presented in section 4. For this case we expect the wavelengths to be larger that for the other modes according to figure 4.10, so we use a longer computational domain: $L/l_0 = 10^4$.

Figure 4.11 **(a)** shows the evolution of the magnetic field perturbation averaged over the domain for the left-hand $\langle B_L \rangle$ (negative helicity, in red) right-hand $\langle B_R \rangle$ (positive helicity, in blue) and the sum for both helicities $\langle B_L + B_R \rangle$ (black). For the plasma conditions modelled, it is indeed the left-hand mode that drives the growth of the magnetic field. At late times the asymptotic value of the perturbation is similar for both left-hand and right-hand polarized waves. We stress however, that there is no evidence that the right-hand polarized perturbation are produced by the growth of the RHR mode. We find that the theoretical k_{max} and γ_{max} taken from the dispersion graph are $k^{th}_{max} l_0 \approx 0.058$ and $\gamma^{th}_{max} \approx 0.042\ \Omega_0$ and the numerical ones obtained from the simulations and plotted in figure 4.11 **(b)** are $k^{num}_{max}\ l_0 \approx 0.043$ and $\gamma^{num}_{max} \approx 0.022\ \Omega_0$.

Figure 4.12 shows the relative density profiles ($\delta n/n$ where n is averaged over the domain) at several times. We find no evidence of significant compression during the simulations, which is consistent with the expectation that the LHR mode produces Alfvén waves, that are non-compressional.

If we take a look at the energies, figures 4.13 **(a)** shows the evolution of the variations of the different energies to their initial value as a function of time ($\langle E(t) \rangle - \langle E(0) \rangle$ averaged over the domain). As in figure 4.7, we can see that the beam kinetic energy decreases and is transferred to the other energies. The kinetic energy is associated with a drift speed of the beam ($E_{k,b} = 1/2 n_b m_b V_b^2$) and as in the RHR case, the final value of this velocity is $V_b = 3V_0$. We can also see that the kinetic energy of the beam is mainly transferred during the linear phase to the thermal energy of the beam. The main plasma, however, gains energy at a constant rate, through interactions with the produced waves. The energy gained from the main first comes from the beam kinetic energy, then after the linear stage it comes from the beam thermal energy that slowly decreases.

Figure 4.13 **(b)** plots the evolutions of both main (blue) and beam (red) temperature anisotropies that develops during the instability. We can see that the beam develops a very small anisotropy with $T_\parallel > T_\perp$, which is unlike the RHR case where the anisotropy favoured the perpendicular temperature. This shows that the pitch-angle scattering effect is less pronounced than in the RHR case. On the other hand, the main plasma experiences an anisotropy that has two stages. In the first stage, during the development of the instability, the perpendicular temperature increases, creating an anisotropy that is comparable to the RHR mode at the same level of anisotropy ($T_\parallel/T_\perp \approx 0.8$). After the

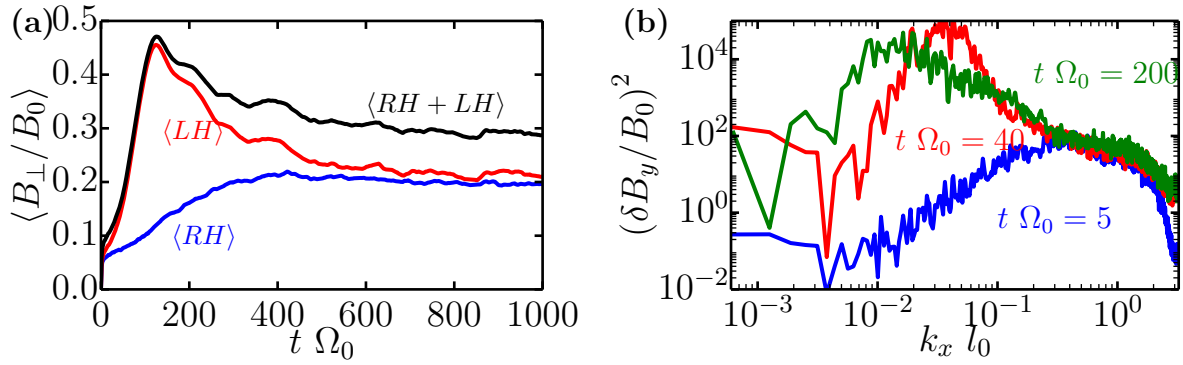

Figure 4.11: **(a)**: evolution of the magnetic perturbation with time in the LHR mode, with both helicities separated: the red line corresponds to the LHR mode (negative helicity) and the blue line is the positive helicity, both are averaged over the whole domain. The black line is the average of the sum of both modes (it does not correspond to the sum of the other two lines). **(b)**: magnetic spectral energy at different times for the left-hand instability (start of the instability $t\ \Omega_0 = 5$, end of linear stage $t\ \Omega_0 = 40$ and final phase $t\ \Omega_0 = 200$). The lines are smoothed with a Gaussian profile which variance increases linearly with the value of k.

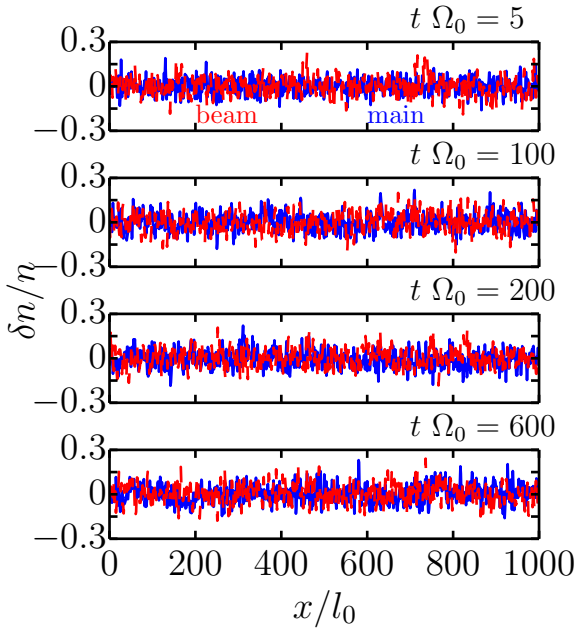

Figure 4.12: Relative density ($\delta n/n$) perturbation profiles for the LHR case at different times (start of the instability $t\ \Omega_0 = 5$, end of linear stage $t\ \Omega_0 = 100$, end of the second phase $t\ \Omega_0 = 200$, third stage $t\ \Omega_0 = 600$). The blue line corresponds to the main plasma and the red one is the beam density.

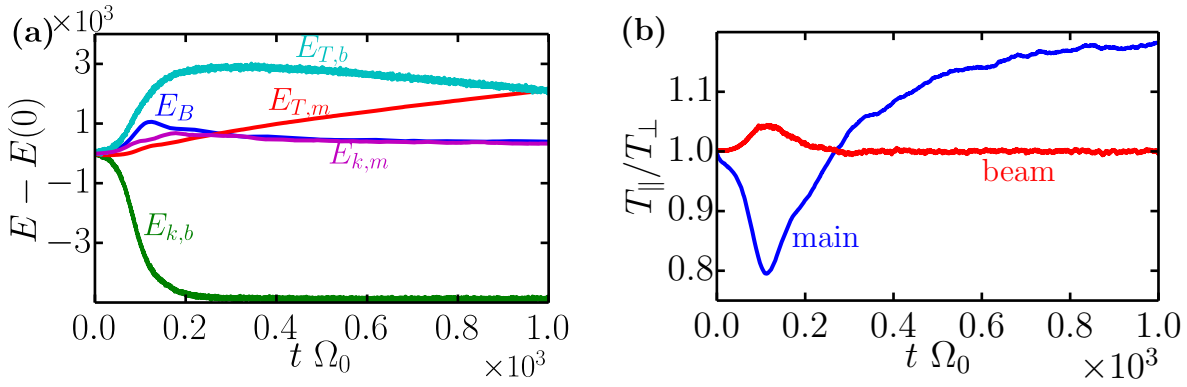

Figure 4.13: **(a)**: evolution of the different energy gains/losses (time variation of the energy minus its initial value $E(t) - E(0)$) with time (magnetic energy E_B (blue), main plasma kinetic (magenta) and thermal (red) energy $E_{k,m}$ and $E_{T,m}$ and the beam kinetic (green) and thermal (cyan) energy $E_{k,b}$ and $E_{T,b}$). **(b)**: evolution of the temperature anisotropies ($T_\parallel/T_\perp$ with $T_\parallel$ the temperature parallel to the local magnetic field and $T_\perp$ the perpendicular temperature) for the LHR case. Again the blue line corresponds to the main plasma and the red line is the beam.

relaxation of this anisotropy $T_\perp > T_\parallel$, which also corresponds to the relaxation of the magnetic perturbation, this anisotropy reverses and the temperature parallel to the magnetic field increase during the last stage to reach asymptotically a value of about $T_\parallel/T_\perp \approx 1.2$. This could come from a mode that is driven unstable by the anisotropy of the main, but this should be investigated in more details in order to identify the process responsible for the increase of the parallel temperature after the development of the LHR mode.

4.3 Numerical results for the non-resonant mode

The final parallel mode predicted by theory is a non-resonant one. It produces right-hand polarized waves that propagate in the direction opposite to the beam. This mode is known to be driven by the current induced by the beam from Bell 2004, which studied this mode in the context of cosmic rays in supernovae remnants shocks. In that case, the cosmic rays play the role of the beam and the shock makes the background, and the mode is driven by the current induced by the cosmic rays $\mathbf{j}_{CR}$ through the Lorentz force $\mathbf{j}_{CR} \times \mathbf{B}$. The reaction of this force makes the magnetic field grow, which increases the driving force of the instability.

In contrast to the resonant case, this mode does not need a full kinetic description to be studied and can be approached using an fluid model, as was done in Bell et al. 2013 that derived the instability using a modified version of the MHD equations. Amato and Blasi 2009 made the calculation using a kinetic model and found consistent results (growth rate, wavelength) with the mode in Bell 2004. In the framework of the MHD, the instability can be understood with a simple explanation involving the Lorentz force acting on the background plasma, as explained in Schure et al. 2012 and illustrated in Zirakashvili, Ptuskin, and Völk 2008 and in figure 2.3.

Indeed, for a polarized perturbation, let us consider a cylindrical coordinate set $\left(\hat{\rho},\hat{\theta},\hat{\mathbf{z}}\right)$. A zeroth order current carried by a beam of ions in a background goes in the positive z direction $\mathbf{j}=j\hat{\mathbf{z}}$, and a first-order magnetic perturbation (perpendicular to the zeroth-order magnetic field) is oriented along the θ direction $\mathbf{B}_1=B_1\hat{\theta}$. This magnetic perturbation can either have a positive or negative helicity, respectively $\mathbf{B}_\perp=-|B_\perp|\hat{\theta}$ and $\mathbf{B}_\perp=|B_\perp|\hat{\theta}$, keeping in mind that this is a simplified model and that the magnetic field is usually a combination of these two helicities. In that case the Lorentz force $\mathbf{F}_L$ is the force created by the magnetic field acting on the beam of ions $\mathbf{F}_{\mathbf{B}\to\mathbf{j}}$ and writes: $\mathbf{F}_L=\mathbf{F}_{\mathbf{B}\to\mathbf{j}}=\mathbf{j}\times\mathbf{B}_1=jB_1\left(\hat{\mathbf{z}}\times\hat{\theta}\right)=-jB_1\hat{\rho}$. Bai et al. 2015, who made this calculation within a fluid framework, showed that this force $\mathbf{F}_L$ results in a reaction force acting on the background $\mathbf{F}_{\mathbf{j}\to\mathbf{B}}=-\mathbf{F}_{\mathbf{B}\to\mathbf{j}}=-\mathbf{F}_L$ that writes $\mathbf{F}_{\mathbf{j}\to\mathbf{B}}=jB_1\hat{\rho}$. For a positive helicity ($\mathbf{B}_\perp=-|B_\perp|\hat{\theta}$) we get $\mathbf{F}^R_{\mathbf{j}\to\mathbf{B}}=-jB_1\hat{\rho}$ and for a negative helicity ($\mathbf{B}_\perp=|B_\perp|\hat{\theta}$) $\mathbf{F}^L_{\mathbf{j}\to\mathbf{B}}=jB_1\hat{\rho}$. We can see that this reaction to the Lorentz force has an unstable effect only on negative helicities as it expands the magnetic field. According to 4.1 **(a)**, this corresponds to a right polarization when the wave propagates in the negative direction, which is consistent to Gary 1991 and the Bell instability.

The non-resonant mode can compete and then dominate the resonant mode for faster or denser beams, that is, for a higher kinetic energy of the beam. The cases where current induced by the beam is high, is relevant for example in astrophysical shocks Bell et al. 2013. We present here some results of simulations where this mode dominates. The parameters chosen are a density ratio $n_b/n_m=0.016$, a beam fluid velocity $V_b/V_0=57$ and "cold" beam with a thermal speed of the order of the Alfvén speed. The evolution of the instability follows the same phases as for the two resonant modes, with a linear phase where magnetic field perturbations grow exponentially, the non-linear saturation of the mode and the relaxation to an asymptotic constant value of magnetic field perturbation, which for the conditions modelled is of the order of the initial magnetic field ($\delta B/B_0\sim 1$). Regarding the growth rates and the fastest growing wave numbers, linear theory (see Winske and Leroy 1984) gives the simplified expressions, valid for $f\ll 1$, $fV_b<1$ and $fV_b^2\gg 1$:

$$\frac{\gamma^{NR}_{max}}{\Omega_0} = \frac{1}{2}\frac{f}{(1-f)^{3/2}}\frac{V_b}{V_0} \tag{4.47}$$

$$\frac{k^{NR}_{max}}{l_0} = \frac{-fV_b}{2V_0(1-f)} \tag{4.48}$$

From the simulations, we find $\gamma\approx 0.22\ \Omega_0$ which compares well with the approximate theoretical value $\gamma^{(th)}_{max}\approx 0.46\ \Omega_0$; similarly $\left(B_y(k)/N_0\right)^2$ shows that the fastest growing wave number is $|k_{max}|\ l_0=0.40$ at $t\ \Omega_0=10$, the theoretical one being $k^{(th)}_{max}\ l_0\approx -0.46$. The perturbation reaches a maximum of $B_\perp^{(max)}\approx 4.57B_0$. Figure 4.14 shows the magnetic perturbation for a field line in 3D for both negative (red) and positive (blue) helicities at different times. As expected this shows a strong dominance of the negative helicity until the later stages, where both modes are then of comparable amplitude.

We now focus on the energy exchanges between the different components of the plasma and the magnetic field. Figure 4.15 **(a)** shows the evolutions of the different energies

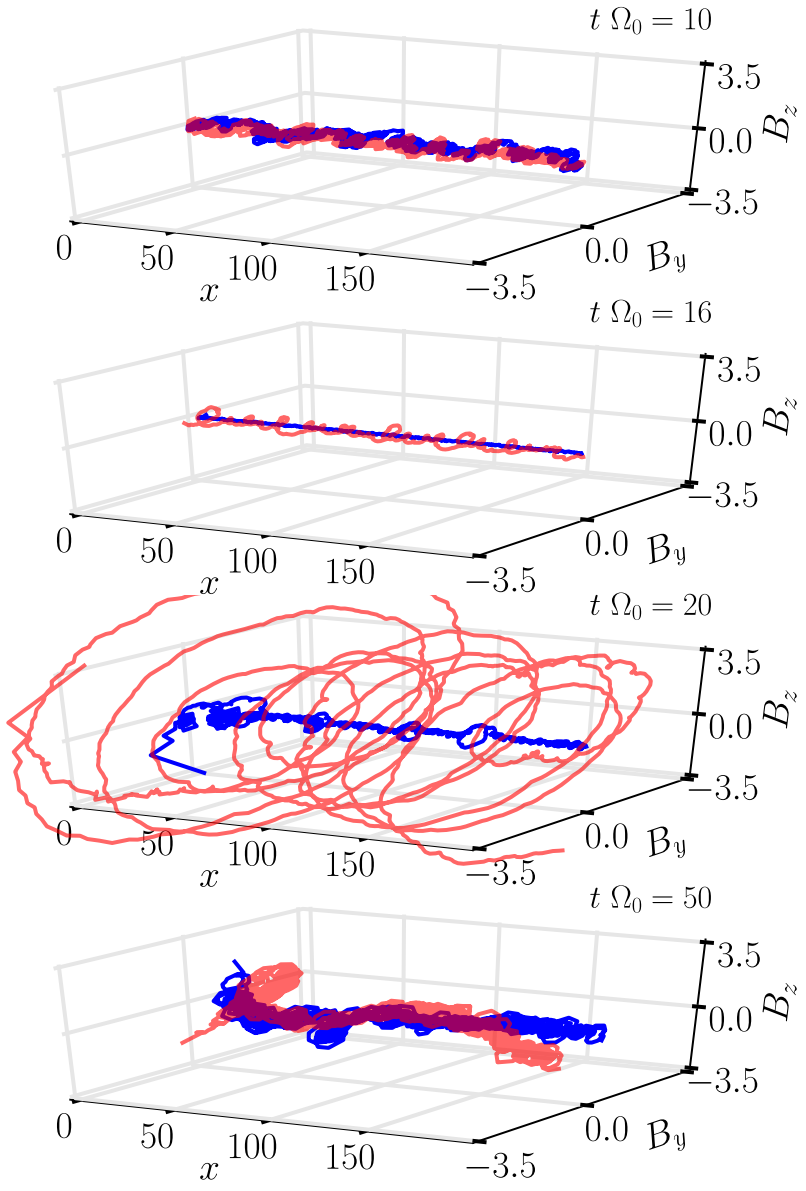

Figure 4.14: Perturbed magnetic field components (B_y, B_z) as a function of x for the positive (blue) and negative (red) helicities (the red line thus corresponds to the NR mode), for the times: start of the instability ($t\,\Omega_0 = 5$), linear phase ($t\,\Omega_0 = 10$), saturation ($t\,\Omega_0 = 20$), final stage ($t\,\Omega_0 = 200$).

normalized to the initial beam kinetic energy. During the linear phase, the energy goes primarily into the thermal energy of the main plasma and the magnetic field. This agrees with quasilinear theory which predicts that the total energy gained by the main plasma and the magnetic field are comparable. The latter is seen to quickly relax to a level close to the its initial value. We find that, as well as in the RHR mode, the beam experiences large density fluctuations of the order of $\delta n_b/n_b \approx 0.6$. This is consistent with the quasilinear result in Winske and Leroy 1984, which says that the beam is less disrupted in the NR case for a given amplitude of the waves, and consequently that a similar compression of the beam requires a higher level of magnetic perturbation. The beam density perturbation ($\delta n_b/n_b \approx 0.6$) is comparable to the one found in the RHR case ($\delta n_b/n_b \approx 0.4$), but the level of magnetic perturbation is much higher in the NR case (about $B_\perp^{(max)} \approx 4.7 B_0$ against $B_\perp^{(max)} < 0.45 B_0$ in the RHR case).

We also find that heating of the main plasma is associated with large fluctuations of its density $\delta n_m/n_m \approx 0.5$. This behaviour is different from the RHR mode, where the density perturbations of the main plasma was negligible. This can be explained considering that the amplitude of the produced waves is much higher in the NR case (about $B_\perp^{(max)} \approx 4.7 B_0$) than in the RHR case ($B_\perp^{(max)} < 0.45 B_0$, so ten times lower). Goldstein 1978 studied a coupling process in which such Alfvén wave decays by producing daughter waves, of which one is electrostatic (hence, compressional). A higher level of magnetic perturbation would then result in the production of a higher level compressional waves, explaining the level of observed density perturbation. The heating of the main plasma is much higher than in the RHR case, with most of the initial beam kinetic energy going into $E_{T,m}$. We note that the beam and the main plasmas remain out of thermal equilibrium: the energy density ratio in the last phase is $E_{T,b}/E_{T,m} \approx 0.33$, and if both populations were at thermal equilibrium we would expect it to be the the same as the density ratio $f = 0.016$. In the collisional case, we expect this characteristic to disappear and the system to relax to thermal equilibrium.

Figure 4.15 **(b)** plots the temperature anisotropy, $T_\parallel/T_\perp$, as a function of time for the beam (red) and the main plasma (blue). It shows a strong anisotropy ($T_\perp \approx 5 T_\parallel$) for both the beam and the main plasma, that was not present in the resonant cases. Again, this result agrees with quasilinear theory in the fact that the main ions take the energy mainly in the perpendicular direction (hence the strong anisotropy). However, as seen previously, the anisotropy around $t\,\Omega_0 = 16$ is not truly relevant as the distribution is too far from a maxwellian. To sum it up, the NR mode is present for more energetic beams and generates negative helicity waves, that are able to disturb a lot more the main plasma than the resonant modes by inducing density perturbations and strong anisotropy.

We are now interested in the effects of the NR mode on the particle distribution function. Figure 4.16, plots the distribution function of the beam (red scale) and the main plasma (blue scale) in the plane $v_\parallel$-$v_\perp$ at different times. In the first panel ($t\,\Omega_0 = 10$) of the figure, we can see that the beam experiences strong pitch-angle scattering, only transferring very little (less than 2%) of its kinetic energy to the main plasma and to the waves. When the magnetic field starts to grow ($t\,\Omega_0 = 15$), the beam kinetic energy decreases sharply and the main plasma experiences a strong heating as seen in figure 4.15, which is consistent with the quasilinear theory as developed in Winske and Leroy

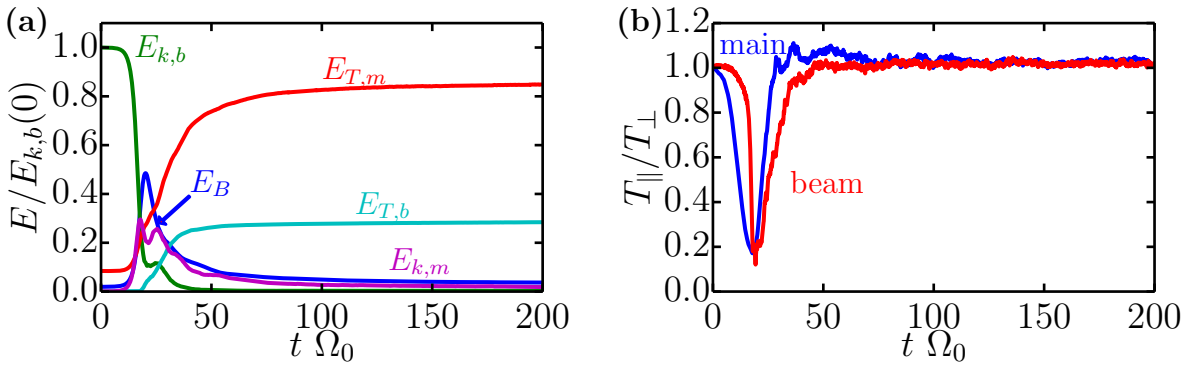

Figure 4.15: **(a)**: evolution of the different energies with time for the NR case (magnetic energy E_B (blue), main plasma kinetic (magenta) and thermal (red) energy $E_{k,m}$ and $E_{T,m}$ and the beam kinetic (green) and thermal (cyan) energy $E_{k,b}$ and $E_{T,b}$) normalized with the initial beam kinetic energy $E_{k,b}(0)$. **(b)**: evolution of the temperature anisotropies ($T_\parallel/T_\perp$ with $T_\parallel$ the temperature parallel to the local magnetic field and $T_\perp$ the perpendicular temperature) for the NR case. Again the blue line corresponds to the main plasma and the red line is the beam.

1984 under some approximations (cold plasmas), which gives that in the NR mode, the beam undergoes a deceleration as its loss of energy mainly comes from its parallel energy. However the quantities in that paper are not clearly defined, which makes their results difficult to interpret.

By $t\ \Omega_0 \approx 16$ (figure 4.16 second panel), the distribution of the beam shows inhomogeneities due to particle bunching induced by the strong electromagnetic fluctuations that are generated by the instability itself. During this stage, we need to keep in mind that the beam distribution is too far from a Maxwellian for the notion of temperature to be truly relevant. At the same time, the main plasma develops a strong temperature anisotropy with most of the energy going in the direction perpendicular to the magnetic field ($T_\parallel/T_\perp < 1$), as observed in figure 4.15 **(b)**. Between $t\ \Omega_0 = 16$ and $t\ \Omega_0 = 20$ (second and third panels), this inhomogeneous structure completely collapses and both the beam and the main distributions reach their most anisotropic form, while a strong energy exchange occurs between the beam and the main plasma. In the last panel (at $t\ \Omega_0 = 50$), the beam forms a bean-like distribution, with the center of the $(v_\parallel, v_\perp)$ space empty of particles as for the RHR mode (see figure 4.5) and the main plasma relaxes to an isotropic Maxwellian.

4.4 Mixed case

Some of the results and peculiarities of each mode presented in the previous sections (such as the quantities of energy exchanged) can be linked to the differences in the initial kinetic energy of the beam. This, as well as other parameters, were changed to be in a plasma regime where each mode could be studied separately. However it is also useful to study these modes under the same conditions in order to compare their effects more

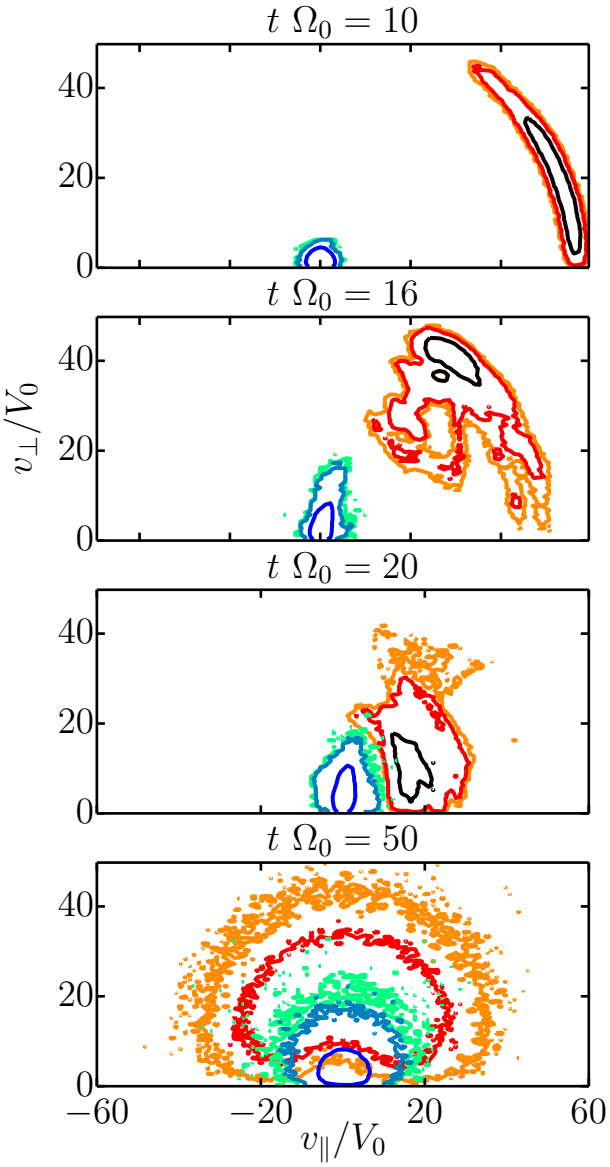

Figure 4.16: Contours of the distribution function integrated over the spatial domain $f(v_\parallel, v_\perp)$ in the plane $v_\parallel/v_\perp$, velocities parallel and perpendicular to the local magnetic field for the NR case. The blue color scale is the main plasma and the red one corresponds to the beam. The different panels correspond to different stages of the instability: the end of linear phase ($t\ \Omega_0 = 10$), the saturation ($t\ \Omega_0 = 20$) and final state ($t\ \Omega_0 = 50$).

directly. In addition, in many realistic plasma we expect different modes to coexist and compete. We present here a case where the RHR and the NR modes have approximately the same growth rates. The simulations are done with a ratio of beam to main density $f = n_b/n_m = 0.1$, $V_b = 10$ and both thermal velocities of the order of the Alvfén speed. The dispersion relation relevant for this case is presented in figure 2.6 for the cold plasma case.

Figure 4.17 shows the evolution in time of the magnetic perturbation in the mixed case for both RHR (positive helicity, blue) and NR (negative helicity, red) cases, with the sum of both modes in black and the total magnetic perturbation in green. As we can see, the total magnetic perturbation corresponds well to the sum of both modes, as expected. We can see that both modes grow to approximately the same level of perturbation and have similar growth rates. The RHR mode takes a slightly longer than the non-resonant mode to start growing. Again we find good agreement with linear theory for the cold plasma case, which gives $k_{max}^{(th)} l_0 \approx 0.14$ and $\gamma_{max}^{(th)} \approx 0.38\Omega_0$, while the numerically measured are $k_{max}^{(num)} l_0 \approx 0.18$ and $\gamma^{(num)} \approx 0.31\Omega_0$ for the RHR mode, which shows a good agreement for both k and γ. We can see that, while the growth rate does not depend much on the density (increasing the density by 10 only increases γ by 2 or 3), the resonant wavenumber is barely affected, which confirms that k mainly depends on V_b for the RHR case (see Winske and Leroy 1984). For the NR mode we get $k_{max}^{(th)} l_0 \approx -0.54$ and $\gamma_{max}^{(th)} \approx 0.44\Omega_0$ while the numerically measured are $k_{max}^{(num)} l_0 \approx 0.38$ and $\gamma^{(num)} \approx 0.20\Omega_0$. We verify that both RHR and NR modes have similar growth rates, and the magnetic energy is expected to develop at both $k_{max}^{(RHR)}$ and $k_{max}^{(NR)}$. All these values along with the other cases (sections 4.2 and 4.3) are summarized in table 4.3.

There is a delay between the saturation of the two modes, so the magnetic spectral energy shows alternatively a maximum at $k_{max}^{(NR)}$ and then $k_{max}^{(RHR)}$. During a first phase the total magnetic perturbation is mostly due to the NR mode. In the last stage, the situation in inverse since the NR stabilizes at a level less important than the RHR mode (the NR stabilizes at a level half the one of the RHR mode), the perturbation then comes mainly from the resonant mode. Indeed the RHR saturates at $B_\perp^{(max)} \approx 1.17B_0$ and has a perturbation level of $B_\perp^{(end)} \approx 0.61B_0$ in the final stage (which makes a ratio of $B_\perp^{(max)}/B_\perp^{(end)} \approx 2$), while for the NR mode the magnetic perturbation goes from $B_\perp^{(max)} \approx 1.32B_0$ to $B_\perp^{(end)} \approx 0.21B_0$ (which makes a ratio of $B_\perp^{(max)}/B_\perp^{(end)} \approx 6.3$). This means that the waves produced by the NR mode (with negative helicity) are better reabsorbed by the plasma than the waves produced by the RHR mode (with positive helicity) during the final stage.

Figure 4.17 **(b)** plots the evolution of the energies with time for the mixed case, normalized with the initial beam kinetic energy. Again we observe that the beam kinetic energy almost goes to zero after the second phase, and that most of the energy goes into the heating of both the beam and main ions. As in the NR case, the populations are not at thermal equilibrium, but here the heating of the beam is higher in that case. As we saw the NR mode induces a stronger heating of the main, associated with a compression, and a sharper slowing down of the beam. The heating of the main that we observe in figure 4.17 **(b)** is thus due to the NR mode. On the other hand, the RHR have been shown

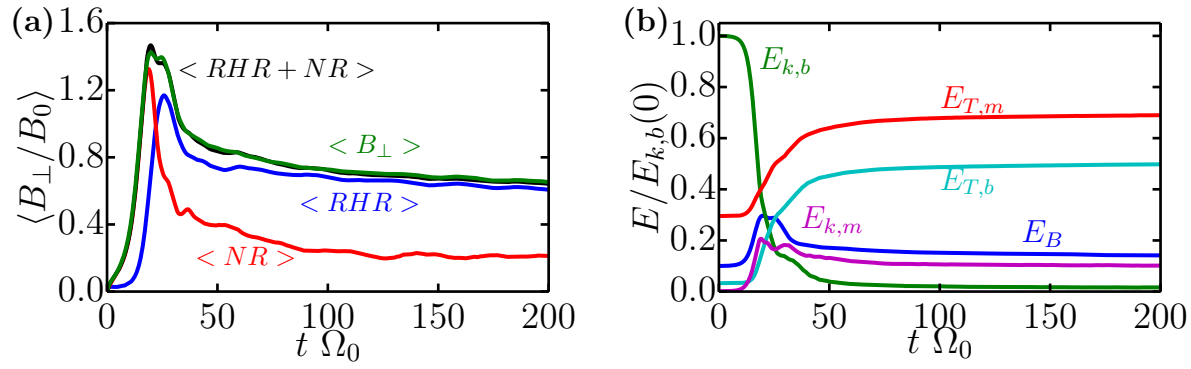

Figure 4.17: **(a)**: evolution of the total magnetic perturbation (green), the decomposition to the RHR (blue), the NR (red), the sum of the two modes (black) for the mixed case. **(b)**: evolution of the different energies with time for the mixed case (magnetic energy E_B (blue), main plasma kinetic (magenta) and thermal (red) energy $E_{k,m}$ and $E_{T,m}$ and the beam kinetic (green) and thermal (cyan) energy $E_{k,b}$ and $E_{T,b}$) normalized with the initial beam kinetic energy.

to be more effective in converting the beam kinetic energy into beam thermal energy: in the RHR case (figure 4.7 **(a)**), 80% of $E_{k,b}$ is transferred in $E_{T,b}$ while in the NR case (figure 4.15), only 30% of $E_{k,b}$ went in $E_{k,b}$. So the smaller gap between $E_{T,m}$ and $E_{T,b}$ in figure 4.17 **(b)** compared to figure 4.15 is imputable to the RHR mode. As well, the waves generated by the RHR have more energy in the final stage than those associated with the NR mode.

4.5 Influence of the plasma temperatures on the instability

We are now interested in the impact of the plasma temperature on the development of the instability. As we already saw, the LHR mode is only present when the beam is very hot compared to its drift speed ($v_{T,b} \gg V_b$). To study the effects of the main and beam temperature on the RHR and the NR, we use the mixed case presented in section 4.4 and run simulations varying either $v_{T,m}$ or $v_{T,b}$. Subsection 4.5.1 presents the effects of the beam temperature and 4.5.2 shows the influence of the main temperature on the instability.

4.5.1 Effects of the beam temperature

As explained in section 4.2.3, increasing the temperature of the beam can lead to the development of a LHR mode for sufficiently high temperatures. In this section we are interested in studying how the beam temperature affects the evolution of the RHR and the NR modes only. Therefore, we chose initial conditions ($v_{T,b} < V_b$) such that the growth rate of the LHR mode remains very low; the thermal velocity of the main plasma is kept at $v_{T,m} = V_0$. Figure 4.18 **(a)** shows the maximum value of the magnetic perturbation

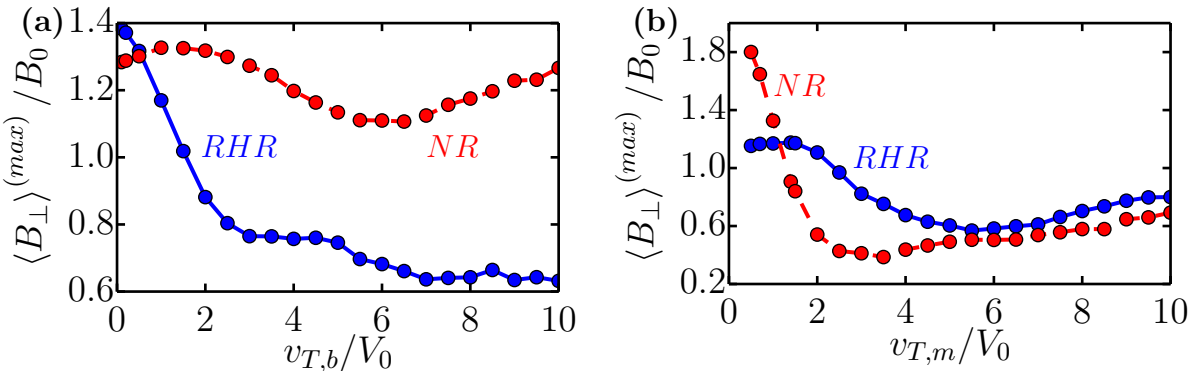

Figure 4.18: Level of magnetic saturation $\langle B_\perp \rangle^{(max)}/B_0$ as a function of the the beam thermal velocity $v_{T,b} = \sqrt{\beta_b B_0^2/2n_b m_b}$ (panel **(a)**) and $v_{T,m} = \sqrt{\beta_m B_0^2/2n_m m_m}$ (panel **(b)**) for the mixed cas, the RHR (positive helicity, blue) and NR (negative helicity, red) modes being separated. Each dot correspond to a simulation with a given thermal velocity.

$\langle B_\perp \rangle^{(max)}/B_0$ of both RHR (blue) and NR (red) modes as a function of the beam thermal velocity. Their contribution is separated as previously explained in 4.1.3. Our simulations show that for the values of $v_{T,b}$ simulated here, the level of magnetic field perturbations generated by the RHR mode decreases with increasing beam temperature, and levels off at about half of the value for a nearly zero-temperature beam.

This behaviour can be understood by considering the spread of the beam distribution function when increasing its temperature. The variance of the beam distribution $(v_{T,b}^2)$ gets higher so the bulk of the distribution becomes less populated, and less particle fulfill the resonance condition $\omega - kv_\parallel + \Omega_C = 0$ as seen in 4.2.2. Since the energy exchange comes from this resonance, less particles are able to resonate, which means less energy going into the magnetic field.

On the contrary, we can see that the maximum level of magnetic field perturbations driven by the non-resonant mode is largely unchanged by the increasing beam temperature. This is consistent with the mode being driven by the unperturbed component of the current that is generated by the beam (see Schure et al. 2012) and which is unaffected by its temperature.

4.5.2 Effects of the main temperatue

We are now interested in the influence of the main plasma temperature on the instability. Unlike the case described in the previous section, where increasing the beam temperature can lead to the development of the LHR mode, increasing the main plasma temperature does not excite a new unstable mode. For the simulations presented here the initial beam thermal velocity is kept constant $v_{T,b} = V_0$ and only the RH and NR modes are present. Figure 4.18 **(b)** plots the level of saturation $B_\perp^{(max)}$ generated by the RHR (blue) and the NR (red) modes as a function of the main plasma thermal velocity. The effects of the modes are separated as detailed in section 4.1.3.

We observe that the maximum level of the perturbed magnetic field decreases for NR mode with increasing main plasma temperature, while the RHR mode is barely affected (its saturation goes from $\langle B_\perp \rangle^{(max)}/B_0 \approx 1.1$ at $v_{T,m} = V_0$ to $\langle B_\perp \rangle^{(max)}/B_0 \approx 0.8$ at $v_{T,m} = 10V_0$). The non-resonant mode is quickly damped as we increase the main temperature and goes from $\langle B_\perp \rangle^{(max)}/B_0 \approx 1.8$ at $v_{T,m} = V_0$ to $\langle B_\perp \rangle^{(max)}/B_0 < 0.4$ at $v_{T,m} = 3V_0$. This gives us a clue about the process involved in the growth of this mode. Indeed, as we increase the thermal velocity of the main plasma, we also increase the plasma parameter β_m which is the ratio between the thermal pressure to the magnetic pressure. Thus we increase the pressure it applies to the rest of the plasma. As the instability develops, the magnetic field starts to grow and distort. This results shows that the main pressure opposes this distortion of the magnetic field, probably by applying a counter force that keeps the magnetic pressure from increasing too much, hence the development of the NR mode is reduced. This effect is thus not relevant to the case seen in the previous section and can mostly be seen when changing the temperature of the main component. This effect needs further investigation, for example in 2D or 3D simulations, to evaluate the validity of this explanation.

4.6 Influence of the particle mass on the instability

As in section 2.8 we are interested in the effects of heavier ions on the evolution of the instability. Winske and Gary 1986 studied the influence of the mass of the beam particles m_b on the growth rate of both RHR and NR instabilities, and showed that the RHR mode have a smaller growth rate when increasing m_b while the NR growth rate is unaffected. This is also shown in figure 2.7 **(b)**. As in the earlier section, and in order to study the effects of the ion mass on both modes simultaneously, we simulate here the mixed RHR and NR case with a density ratio $f = 0.1$, a drift velocity $V_b = 10V_0$ and thermal velocities of $v_{T,b} = v_{T,m} = V_0$ (the parameters are found in table 4.2).

Figure 4.19 **(a)** plots the growth rate γ as a function of main ion mass m_m, for the RHR (blue) and NR (red) modes. The growth rate is calculated from the simulated data as $\gamma = \log(B_\perp(t_2)/B_\perp(t_1))/(t_2 - t_1)$ where t_2 and t_1 and the times bounding the linear phase. The first important result is that the NR mode experiences a strong decrease of its growth rate when increasing the mass of the ions of the main plasma ($\gamma^{(NR)} < 0.05\Omega_0$ when $m_m > 5m_p$), which is consistent with figure 2.7 **(a)**. However, the RHR growth rate also decreases when increasing m_m, and although the difference is not so significant as for the NR mode, it is not negligible (from $\gamma^{(RHR)} \approx 0.3\Omega_0$ when $m_m = m_p$ to $\gamma^{(RHR)} \approx 0.2\Omega_0$ when $m_m = 15 - 20m_p$) and does not appear in figure 2.7 **(a)**. This decrease in the NR growth rate can be seen as an inertial effect. Indeed, in Bell et al. 2013 the mode is reproduced using a modified version of the momentum MHD equation:

$$\rho \frac{du}{dt} = -\nabla P - \frac{1}{\mu_0}\mathbf{B} \times (\nabla \times \mathbf{B}) - \mathbf{j}_b \times \mathbf{B} \tag{4.49}$$

In this equation, u is the fluid velocity of the background plasma, ρ is the mass density and $\mathbf{j}_b \times \mathbf{B}$ is the added term that drives the NR mode and generated by the current of the beam. We can see that for a given force per unit volume $\mathbf{j}_b \times \mathbf{B}$, an increase of

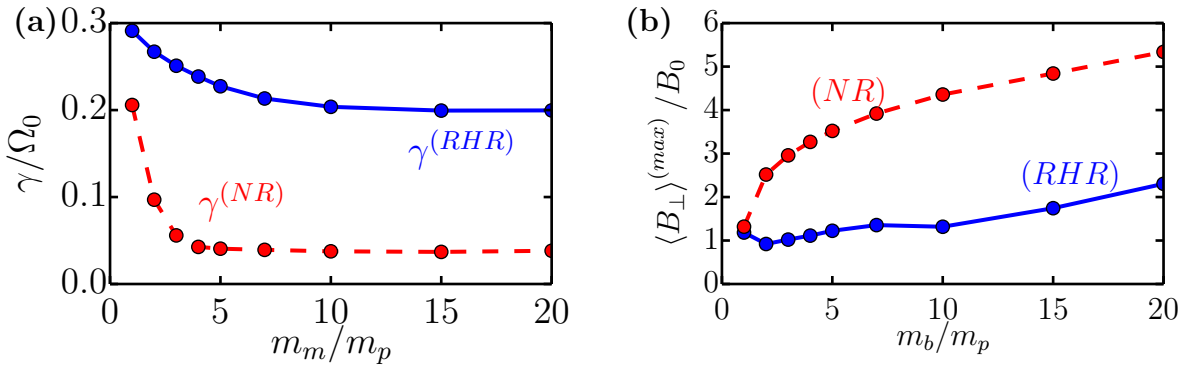

Figure 4.19: Instability growth rate γ as a function of the main mass m_m (panel **(a)**) and the beam mass m_b (panel **(b)**) for the RHR (blue) and the NR (red) modes. Each dot corresponds to a simulation with the corresponding mass. In this case we have $f = 0.1$, $V_b = 10V_0$ and the initial thermal velocities are kept to $1V_0$.

the mass density leads to a decrease of the acceleration of the plasma. This means that the instability has more difficulties to develop when the mass of the fluid to accelerate is higher. Thus the instability needs more energy to disturb the system so the mass acts as a stabilizer of the system.

Figure 4.19 **(b)** plots the magnetic saturation value as a function of the beam particle mass. It shows, an increase of both modes energy, especially for the NR case. This could be explained at first by the fact that the beam contains more kinetic energy when it is heavier. We know from Winske and Leroy 1984 an estimate for the level of magnetic saturation using the quasilinear theory:

$$\left(\frac{B_\perp}{B_0}\right)^{(max)} \propto f^{1/2}\frac{V_b}{V_0} \propto \sqrt{E_{k,b}(0)} \tag{4.50}$$

In this equation, we see that the magnetic saturation is proportional to the square root of the beam kinetic energy. This study was done for proton plasmas, so with $m_m = m_b = m_p$. When increasing the mass of the beam, we increase its kinetic energy and thus the energy available to distribute to the system, and in particular to the electromagnetic waves. This dependence should be investigated further to check the link between the NR saturation and the beam particle mass.

4.7 Discussion

We have presented the main features of the three different modes that are generated by the ion-ion magnetic streaming instability in the collisionless case. The evolution of the plasma can be described by three phases: the linear stage of the instability, its saturation and the relaxation towards a steady level of wave activity. During the first phase, we observe a pitch-angle scattering of the particles of the beam, where these particles lose little energy and are mostly scattered, transferring their velocity parallel to the magnetic field to the perpendicular component, and forming a shell distribution in the velocity space

around the main plasma. The energy is then redistributed to both the beam and the main plasma in the form of thermal energy. The mechanism of the instability is summarized in figure 4.20 where we can see the beam (red) kinetic energy used to enhance electromagnetic waves (**B**), and then this energy being partially returned to both plasmas in the form of thermal energy through wave-particle interactions. We can see that the waves act as a bridge for the kinetic energy of the beam to be redistributed to the ions, increasing the entropy of the system.

In conclusion, we have also identified several modes: the right-hand resonant, the left-hand resonant and the non-resonant modes. By looking at the polarization, we are able to distinguish these different modes. The dominance or coexistence of the modes depend on the density ratio between the beam and the main and on the drift speed of the beam. Each mode corresponds to a different kind of waves, and they do not disturb the densities the same way. The efficiency to transfer energy to both the beam and the main is also a characteristic of each mode. We were able to compare some theoretical results, from both linear and quasilinear theory, with the numerical observations from the simulations. The agreement were found to be good and is summarized in table 4.3.

In this chapter, we identified some main features of the magnetic streaming instability in the collisionless regime:

- three different modes can develop. Depending on the plasma conditions, they can either compete or dominate;
- the development of the instability is independent of the mode and follows a three-stage evolution, with the linear stage, the saturation and the asymptotic relaxation to a stable situation;
- the pitch-angle scattering is present in both RHR and NR modes but less so in the LHR;
- the RHR mode can be separated from the NR or the LHR modes as they generate waves with different helicities;
- the resonant modes are effective at heating the beam, while the NR is more effective at heating the main plasma;
- the RHR mode is strongly affected by the beam temperature and its energy decreases when increasing the beam thermal velocity;
- the NR mode shows a strong influence of the main temperature: when increasing the main pressure, this has the effect of decreasing the development of the NR mode.

All results shown in this section are for the case of a collisionless plasma. In the next chapter we will present simulation results including Coulomb collisions (using the module described in section 3.5) and discuss their effect on the development of the instability.

	k_{max}^{expr}	k_{max}^{cold}	k_{max}^{hot}	k_{max}^{num}	γ_{max}^{expr}	γ_{max}^{cold}	γ_{max}^{hot}	γ_{max}^{num}
RHR case	0.10	0.11	0.11	0.11	0.17	0.17	0.16	0.10
LHR case	X	X	0.06	0.04	X	X	0.04	0.02
NR case	-0.46	-0.45		0.40	0.47	0.43		0.22
Mix case (RHR)	0.10	0.14	0.14	0.18	0.37	0.38	0.37	0.31
Mix case (NR)	-0.56	-0.54		0.38	0.59	0.44		0.20

Table 4.3: Summary of the values of the maximum growth rate γ_{max} and associated wavenumber k_{max} obtained with the different theories and the numerical values. The expressions in Winske and Leroy 1984 give k_{max}^{expr} and γ_{max}^{expr}, the solution of the dispersion relation gives k_{max}^{cold} and γ_{max}^{cold} for cold plasmas and k_{max}^{hot} and γ_{max}^{hot} in the general case, and the numerical simulations give k_{max}^{num} and γ_{max}^{num}.

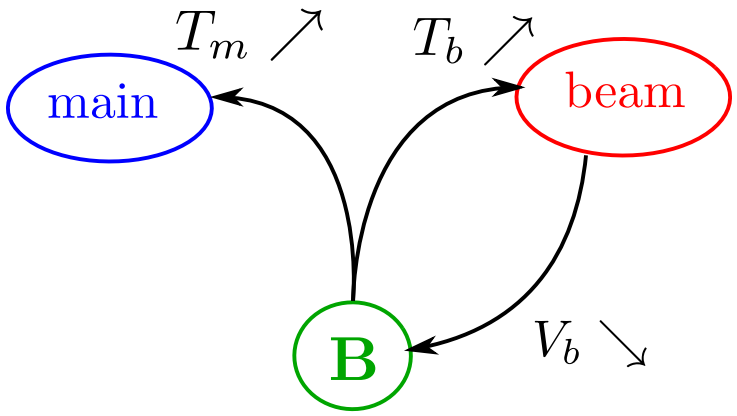

Figure 4.20: Schematic view of the behaviour of the instability. The circled red and blue populations represent respectively the beam and the main plasma, the **B** represents the magnetic field. The arrows represent the energy exchanges associated with the effects on the plasma (slowing down of the beam $V_b \searrow$, increase of the beam or main temperature $T \nearrow$).

Bibliography

Gary, S. P. (1991). "Electromagnetic ion/ion instabilities and their consequences in space plasmas - A review". In: *Space Science Reviews* 56, pp. 373–415 (cit. on pp. 66–68, 87).

— (1993). *Theory of Space Plasma Microinstabilities*, p. 193 (cit. on p. 66).

Winske, D. and M. M. Leroy (1984). "Diffuse ions produced by electromagnetic ion beam instabilities". In: *Journal of Geophysics Research* 89, pp. 2673–2688 (cit. on pp. 66–68, 78, 80, 87, 89, 92, 96, 98).

Wang, X. Y. and Y. Lin (2003). "Generation of nonlinear Alfvén and magnetosonic waves by beam-plasma interaction". In: *Physics of Plasmas* 10, pp. 3528–3538 (cit. on pp. 66, 68).

Bell, A. R. (2004). "Turbulent amplification of magnetic field and diffusive shock acceleration of cosmic rays". In: *Monthly Notices of the RAS* 353, pp. 550–558 (cit. on pp. 67, 86).

Gary, S. P. and W. C. Feldman (1978). "A second-order theory for k parallel B sub 0 electromagnetic instabilities". In: *Physics of Fluids* 21, pp. 72–80 (cit. on p. 67).

Gary, S. P. and R. L. Tokar (1985). "The second-order theory of electromagnetic hot ion beam instabilities". In: *Journal of Geophysics Research* 90, pp. 65–72 (cit. on pp. 67, 81).

Lapenta, G. (2012). "Particle simulations of space weather". In: *Journal of Computational Physics* 231, pp. 795–821 (cit. on p. 67).

Onsager, T. G., D. Winske, and M. F. Thomsen (1991). "Interaction of a finite-length ion beam with a background plasma - Reflected ions at the quasi-parallel bow shock". In: *Journal of Geophysics Research* 96, pp. 1775–1788 (cit. on p. 68).

Akimoto, K. et al. (1993). "Nonlinear evolution of electromagnetic ion beam instabilities". In: *Journal of Geophysics Research* 98, pp. 1419–1433 (cit. on p. 68).

Terasawa, T. et al. (1986). "Decay instability of finite-amplitude circularly polarized Alfven waves - A numerical simulation of stimulated Brillouin scattering". In: *Journal of Geophysics Research* 91, pp. 4171–4187 (cit. on pp. 68, 70, 84).

Winske, D. and S. P. Gary (1986). "Electromagnetic instabilities driven by cool heavy ion beams". In: *Journal of Geophysics Research* 91, pp. 6825–6832 (cit. on pp. 71, 80, 95).

Schure, K. M. et al. (2012). "Diffusive Shock Acceleration and Magnetic Field Amplification". In: *Space Science Reviews* 173, pp. 491–519 (cit. on pp. 71, 86, 94).

Tsurutani, B. T. and G. S. Lakhina (1997). "Some basic concepts of wave-particle interactions in collisionless plasmas". In: *Reviews of Geophysics* 35, pp. 491–501 (cit. on p. 71).

Rogers, B., S. P. Gary, and D. Winske (1985). "Electromagnetic hot ion beam instabilities - Quasi-linear theory and simulation". In: *Journal of Geophysics Research* 90, pp. 9494–9502 (cit. on p. 81).

Wentzel, D. G. (1974). "Cosmic-ray propagation in the Galaxy - Collective effects". In: *Annual Review of Astronomy and Astrophysics* 12, pp. 71–96 (cit. on p. 81).

Bell, A. R. et al. (2013). "Cosmic-ray acceleration and escape from supernova remnants". In: *Monthly Notices of the RAS* 431, pp. 415–429 (cit. on pp. 86, 87, 95).

Amato, E. and P. Blasi (2009). "A kinetic approach to cosmic-ray-induced streaming instability at supernova shocks". In: *Monthly Notices of the RAS* 392, pp. 1591–1600 (cit. on p. 86).

Zirakashvili, V. N., V. S. Ptuskin, and H. J. Völk (2008). "Modeling Bell's Nonresonant Cosmic-Ray Instability". In: *Astrophysical Journal* 678, pp. 255–261 (cit. on p. 86).

Bai, X.-N. et al. (2015). "Magnetohydrodynamic-particle-in-cell Method for Coupling Cosmic Rays with a Thermal Plasma: Application to Non-relativistic Shocks". In: *Astrophysical Journal* 809, 55, p. 55 (cit. on p. 87).

Goldstein, M. L. (1978). "An instability of finite amplitude circularly polarized Alfven waves". In: *Astrophysical Journal* 219, pp. 700–704 (cit. on p. 89).

Chapter 5

Collisional magnetic streaming instability

> Science is a way of trying not to fool yourself. The first principle is that you must not fool yourself, and you are the easiest person to fool.
>
> Richard Feynman - Lecture at the Galileo Symposium in Italy, (1964), Richard Feynman.

Contents

case	n_b/n_m	V_b/V_0	$v_{T,b}/V_0$	$v_{T,m}/V_0$	σ_0/Ω_0	β_b	β_m
RHR (5.2)	0.01	10	1	1	$0-0.6$	0.02	2
NR (5.3.1)	0.016	57	1	1	$0-300$	0.032	2
mixed (5.3.2)	0.1	10	1	1	$0-2$	0.2	2
RHR (5.6.1)	0.01	10	1	1	$0-10^8$	0.02	2
NR (5.6.2)	0.016	57	1	1	$0-100$	0.032	2

Table 5.1: Parameters used for the different cases. Here $v_{T,s} = \sqrt{\beta_s B^2/(2n_s m_s)}$

Chapter 4 presented numerical results of the streaming instability in the collisionless case. Energy exchanges then occurred only through the interaction between particles and the associated self-consistent, macroscopic electromagnetic fields. In this chapter we focus on the effects of Coulomb collision between the ions of the plasmas. In such a case, particles can directly exchange energy between themselves through short-range electric fields.

In this chapter, we present the results of simulations performed for plasma conditions as those used presented in chapter 4, but including ion-ion collisions. In section 5.1 we present general considerations about the effects of collisions on the instability, with an explanation of the methods we use. Results of the RHR case in the collisional case are presented in section 5.2, with detailed comparisons with the collisionless case. The specific cases of the NR and mixed cases are presented in section 5.3. In section 5.4 we describe the influence of the different types of collisions on the instability. Section 5.5 deals with the effects of varying the collision frequency on the different modes. In section 5.6 we present two specific phenomena that are present in the RHR and NR cases in the collisional case. Finally in section 5.7 we summarize and discuss the results of this chapter.

5.1 Introduction to the collisional magnetic streaming instability

In the streaming instability, two population are at play: the main plasma, indicated by the subscript m, and the beam plasma, indicated by the subscript b. In general, we can distinguish three kinds of collision, depending on the nature of the colliding particles (i.e, the populations involved). Their associated collision frequency are: (i) collisions between particles of the beam (beam-beam collisions with a frequency ν_{bb}); (ii) collisions between particles of the main plasma (main-main collisions with a frequency ν_{mm}); (iii) collisions between particles of the main and the beam (main-beam collisions with frequency ν_{mb}). The two former types of collision are "intra-species" collisions, while the latter is "inter-species" collisions. As we saw in equation 3.69, the collision frequency depends on the relative speed between the particles. From Fitzpatrick 2014 and section 3.4.3, we can give an ordering between these collision frequencies. Because we deal with cold plasmas, with

the initial relative drift speed much higher than the initial thermal velocities ($V_{b,0} \gg v_{t,0}$, with 0 the initial value of the collision frequency), we have the initial frequency of the main-beam collisions much lower than the other two frequencies. Moreover, the initial beam-beam collision frequency is lower than the main-main frequency because they have the same thermal velocity but the beam is less dense. Thus we have:

$$\nu_{mb,0} \ll \nu_{bb,0} \ll \nu_{mm,0} \tag{5.1}$$

The collisions being binary and calculated from a Monte-Carlo method, any anisotropy will relax for a sufficiently high value of the σ_0 parameter, which we introduced in equation 3.72. As a result, the temperature anisotropies observed in figure 4.7 where the perpendicular temperature of the beams gets larger than the parallel one should be decreased or quenched because of collisions. Further, the energy gap observed in 4.7 between the beam and the main plasma, where the beam is heated much more than the main, should relax to a Maxwellian distribution as illustrated in figure 3.8 and 3.10. The relative velocity between populations should then fade out with time. The associated collision timescales depend on the value of the σ_0 parameter.

Ion-ion collisions are included in the code with the Monte-Carlo algorithm presented in 3.5. The level of collisionality between ions is controlled in the code by the two parameters σ_0 and Ψ_0. We remind here their expressions:

$$\sigma_0 = \frac{e^4 n_0}{8\pi\varepsilon_0^2 m_p^2 V_0^3} \tag{5.2}$$

$$\Psi_0 = \log\left(\frac{4\pi\left(k_B T_0 \varepsilon_0\right)^{3/2}}{e^3 n_0^{1/2}}\right) \tag{5.3}$$

In this equation, n_0 is the uniform initial density of the system and $k_B T_0 = m_p V_0^2$. The collision frequency between two particles linearly depends on σ_0: the larger σ_0, the larger the collision frequency for a given pair of particles.

The Ψ_0 parameter is needed in the calculation of the Coulomb logarithm: the larger Ψ_0, the larger the collision frequency for a given pair of particles. Since it is a logarithmic dependence, we do not expect Ψ_0 to vary much so we keep it at a constant value of $\Psi_0 = 25$. This value is close to the one relevant in the Earth bow shock for example (for a magnetic field $B_0 \approx 10$ nT and a density of about $n_0 \approx 10^7 m^{-3}$ we get $\Psi_0 \approx 27$). For laser experiments, where $B_0 \approx 20$ T and $n_0 \approx 10^{23} m^{-3}$ we get $\Psi_0 \approx 17$, which is a smaller value but not significantly enough to make a big difference.

As well as in chapter 4, we start with a detailed study of a case where the RHR largely dominates and compare it to the collisionless case. Then we will present the specific features observed in the NR case.

5.2 Effects of the collisions on the right-hand resonant mode

We now consider the RHR case, which for the collisionless case was detailed in section 4.2.2. The density ratio is $f = 0.01$, the bulk speed of the beam is $V_b = 10V_0$ and the thermal velocities are $v_{T,m} = v_{T,b} = V_0$. All parameters used in this chapter are summarized in table 5.1. The associated theoretical growth rate is $\gamma_{max}^{(th)} \approx 0.17\ \Omega_0$ and the numerical one is $\gamma^{(num)} \approx 0.096\ \Omega_0$ at $k_{max} l_0 \approx 0.11$ as presented in section 4.2.2. We use the same parameters in the collisional case with $\sigma_0 = 0.2\ \Omega_0$. Under those conditions, the RHR mode is the only one that can develops. Figure 5.1 **(a)** shows the evolution of the normalized magnetic perturbation, $B_\perp(t)/B_0$, as a function of time. It presents the comparison of for collisionless (dashed line) and collisional cases. One can observe that in the collisional case, the magnetic field reaches a lower saturation level ($B_\perp^{(max)}/ \approx 0.16 B_0$) than in the collisionless case ($B_\perp^{(max)} \approx 0.44\ B_0$). In addition, the magnetic energy associated with the waves in the final stage is smaller by a factor of 2 in the collisional case, compared to the collisionless one. The slope of $B_\perp(t)$ is also lowered in the collisional case, meaning that the growth rate is also slower.

Figure 5.1 **(b)** displays the evolution of the density perturbation $\delta n(t)/n_0$ for the collisionless and collisional cases. For both cases density fluctuations of the main population are negligible. However, in the collisional case, the level of density fluctuations for the beam plasma is lowered by a factor of three in the saturation phase of the instability: $\delta n_b^{(max)} \approx 0.14\ n_0$ in the collisional case, while $\delta n_b^{(max)} \approx 0.40\ n_0$ in the collisionless case.

This can be understood by considering that the waves created by the RH mode are compressional, thus the smaller the magnetic fluctuations (in the collisional case) the smaller the density fluctuation. Nevertheless, at late times, the density fluctuations of the beam decrease to their lowest observable value, and are the same for both modes. The level being a consequence of the fluctuation of the number of particles per cell. Importantly, the level of magnetic fluctuations is different and relatively constant for both modes, meaning that the nature of the waves is changing from a compressional mode to a non-compressional one. This is one of the main result of Wang and Lin 2003 who put forward the idea that the RHR mode associated to the streaming instability, converts to Alfven-like waves in the asymptotic phase.

Figure 5.2 depicts the distribution functions in the $\left(v_\parallel, v_\perp\right)$ space, at $t\ \Omega_0 = 10$, $t\ \Omega_0 = 40$ and $t\ \Omega_0 = 100$, from top to bottom. At $t\ \Omega_0 = 10$ (during the linear growth of the instability), the pitch angle scattering is at play as in the collisionless case, but a strong diffusion in velocity space is observed, resulting in heating of the beam coupled to a decrease of its bulk velocity. As a direct consequence of collisions, the energy gap observed in figure 4.5 in the collisionless case is filled, essentially by the particles of the beam.

We now focus on the effects of collisions on the fastest growing wave-numbers. Figure 5.3 shows the spatial Fourier spectral energy density of the magnetic perturbation for the RHR case at the end of the linear stage ($t\ \Omega_0 = 40$), for $\sigma_0 = 0$ (dashed) and $\sigma_0 = 0.2\ \Omega_0$ (plain). This is the time when the magnetic energy reaches a maximum for both cases (see figure 5.1). Both curves exhibit a peak at approximately the same $k_{max} l_0 \approx 0.11$,

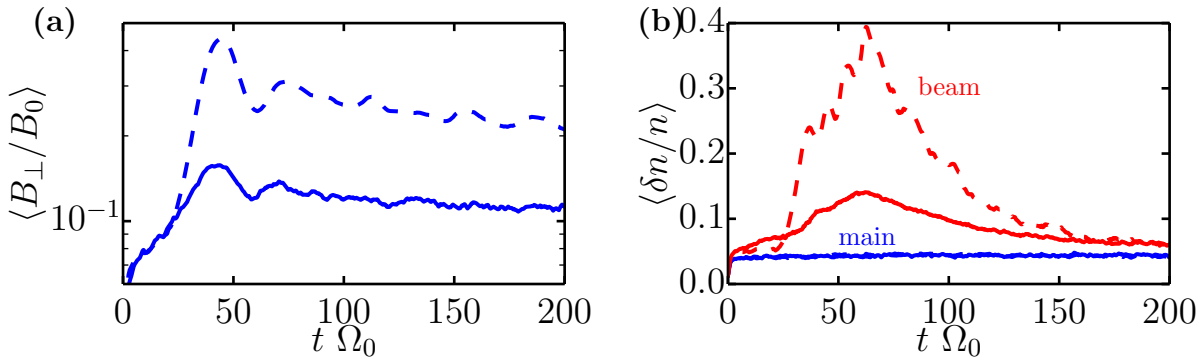

Figure 5.1: **(a)**: evolution of the magnetic perturbation $\langle B_\perp(t)/B_0\rangle$ and **(b)**: evolution of the relative density perturbation $\langle \delta n/n(t)\rangle$ for the beam (red) and the main plasma (blue) in the cases $\sigma_0 = 0$ (dashed) and $\sigma_0 = 0.2\Omega_0$ (plain).

with as expected from the previous discussion, a smaller value of the maximum of the spectral energy density in the collisional case. This results indicates that the mechanism involved in the instability (the $\mathbf{j}_1 \times \mathbf{B}_0$ force) is not affected by the collisions, other than the amount of energy the magnetic field is able to gain from the beam.

5.2.1 Effects on the energies

Figure 5.4 shows the time evolution of the energies in the collisionless (dashed lines) and collisional cases (plain lines, with $\sigma_0 = 0.2\ \Omega_0$), normalized to the initial beam kinetic energy $E^0_{k,b}$. Panel **(a)** plots the evolution of the thermal energies for the beam (blue line) and the main (red line) in the collisional case (solid lines) and collisionless case (dashed line). An important outcome of the simulations is the demonstration that main plasma is substantially heated in the collisional case: its thermal energy increases from $E_{T,m} \approx 3\ E^0_{k,b}$ to $E_{T,m} \approx 3.9\ E^0_{k,b}$, which is equivalent to 90% of the initial beam kinetic energy. Although the beam is initially heated at early times (to reach a value of $E_{T,b} \approx 0.33\ E^0_{k,b}$), it then relaxes via collisions with the main plasma to reach $E_T, b \approx 0.04\ E^0_{k,b}$. This is related to the observation made in chapter 4 for the collisionless case that the beam and main plasmas are not in thermal equilibrium after the development of the instability (see figure 4.7 and 4.15). Coulomb collisions result in an energy exchange and relaxation process for all particles (whatever their population) to a thermal equilibrium (see section 3.8). As a consequence, the beam and the main are relaxed to thermal equilibrium as soon as the inter-species collisions become important. We observe that by the end of the simulation, the ratio between the beam and the main energy densities is $E_{T,b}/E_{T,m} \approx 0.01 = f = n_b/n_m$, which means that both populations are at thermal equilibrium. This thermalization takes place after an increase in $E_{T,b}$, which is due to the strong heating induced by the instability, both in the collisionless as well as the collisional case. Relating to figure 5.1 **(b)**, we can see that, although there is a strong heating of the main due to collisions, there is no evidence of significant density perturbation of the main plasma. This means that this heating is probably only due to the collisional relaxation to thermal equilibrium. The fact that the beam experiences a relatively strong heating

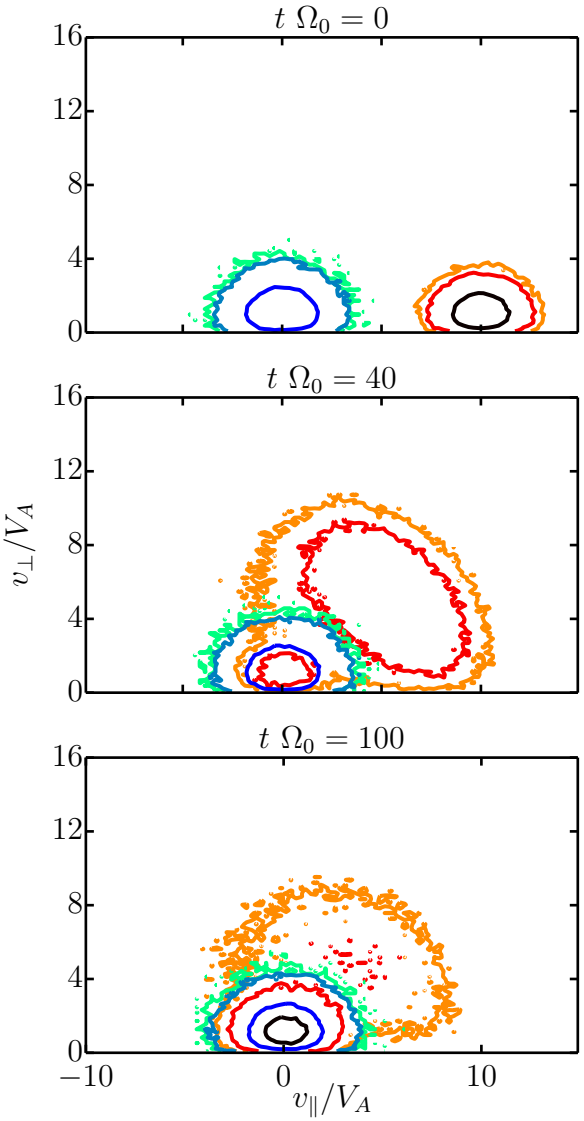

Figure 5.2: Contours of the distribution function $f(v_\parallel, v_\perp)$ in the plan $v_\parallel/v_\perp$, velocities parallel and perpendicular to the local magnetic field for the RHR case with $\sigma_0 = 0.2\Omega_0$. The distribution is integrated over the computational domain. The blue color scale is the main plasma and the red one corresponds to the beam. The different panels correspond to different stages of the instability: the initial state ($t\ \Omega_0 = 10$), the end of linear phase ($t\ \Omega_0 = 40$) and third stage ($t\ \Omega_0 = 100$).

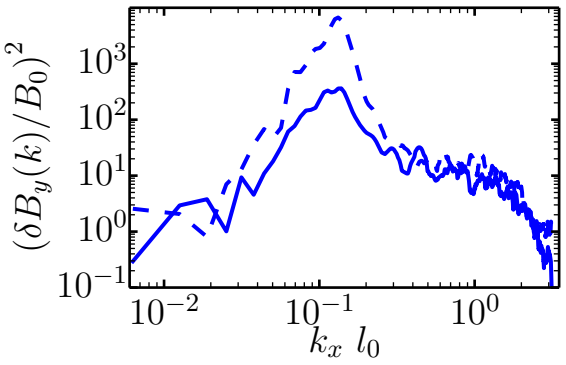

Figure 5.3: Magnetic spectral energy $(B_y(k_x)/B_0)^2$ in the RHR case with $\sigma_0 = 0$ (dashed) and $\sigma_0 = 0.2\Omega_0$ (plain). This is for $t\ \Omega_0 = 40$, when the magnetic field is close to its saturation according to figure 5.1.

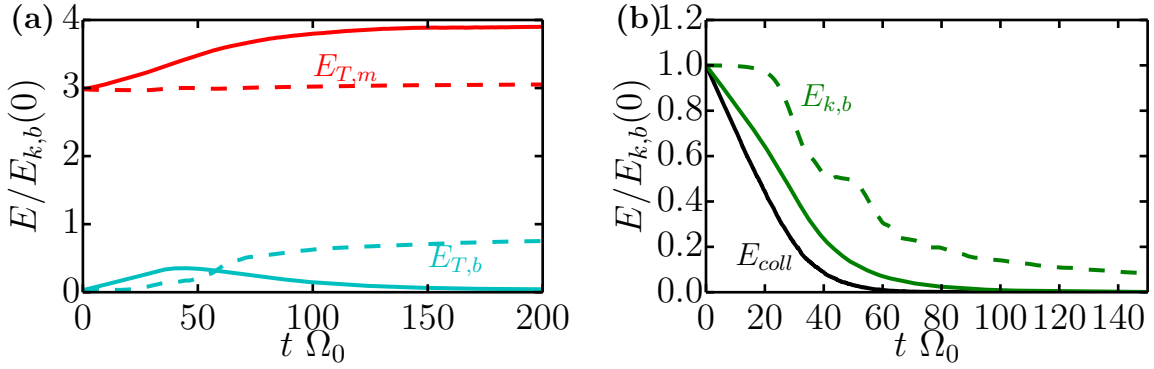

Figure 5.4: Evolution of **(a)**: thermal energies (main $E_{T,m}$ (red) and beam $E_{T,b}$ (cyan)) and **(b)**: beam kinetic energy $E_{k,b}$ in the cases $\sigma_0 = 0$ (collisionless) in dashed lines and $\sigma_0 = 0.2\Omega_0$ in solid lines. The energies are normalized by the initial beam kinetic energy $E_{k,b}(0)$. The black line E_{coll} corresponds to the collisional slowing down in a 0D model.

before the instability has time to develop also leaves less particles to resonate with the waves, which explains the reduction of the growth rate observed in figure 5.1 **(a)**.

Figure 5.4 **(b)** depicts (green line) the time evolution of the kinetic energy of the beam in the collisional (solid line) and collisionless (dashed line) cases. It can be seen that it takes about $20\Omega_0^{-1}$ for the instability to start slowing down the beam in the collisionless case, while the velocity decreases from the beginning in the collisional case. In this panel, the black line represents the expected slowing down from a simplified simulation in 0D that only includes collisions (see section 3.6). The slowing down of the beam when the instability is present is less severe than in the case where only collision where present, indicating that effects due to the instability, such as the heating of the main and the beam, play indeed an important role in the evolution of the plasma.

From figure 5.4 we saw that in the collisional case, the thermal energy of the beam is transferred, after a initial growth, to the main plasma. More details on temperature of the beam and main plasma are shown in figure 5.5. There the temperature anisotropies, $T_\parallel/T_\perp$ of the main (blue) and the beam (red), are shown for the cases $\sigma_0 = 0$ (dashed

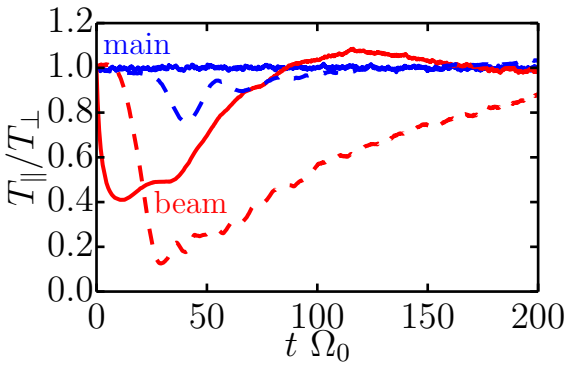

Figure 5.5: Evolution of the temperature anisotropies $T_\parallel/T_\perp$ for the cases $\sigma_0 = 0$ (dashed) and $\sigma_0 = 0.2\Omega_0$ (plain). The blue line corresponds to the main plasma and the red to the beam.

line) and $\sigma_0 = 0.2\ \Omega_0$ (solid line). Focusing on the main population, collisions can be seen to essentially erase the anisotropy that develops in the collisionless case. This is a clear consequence of the high level of collisions between particles of the main, as initially $\nu_{mm} = 100\Omega_0$. On the other side, the strong anisotropy ($T_\parallel/T_\perp < 0.2$) for the beam in the collisionless case does not vanish in the same way with collisions, although it is decreased. This is because the beam-beam collision frequency responsible for the relaxation of this anisotropy is not high enough at this value of σ_0. Instead, we can see that before the instability has time to develop (between $0 < t\Omega_0 < 10$), the beam shows a sharp increase in its perpendicular temperature, as well as a relatively strong relaxation of the anisotropy after the linear stage, both due to the main-beam collisions. The early heating of the beam observed in figure 5.4 **(a)** thus goes primarily in the direction perpendicular to the magnetic field, creating this strong anisotropy that we observe here.

5.2.2 Evolution of the collision frequencies

As previously said, the two populations (main and beam) results in three types of collisions: the main-main collisions, the beam-beam collisions and the main-beam collisions, with their associated collision frequencies, ν_{mm}, ν_{bb} and ν_{mb}, respectively. The collision frequency depends on the local value of the density and relative velocity, this value will evolve with time as the instability develops. To quantify the relative importance of these collisions, we define using equation (3.69) a mean value of the collision frequency. For a given pair of particles, this collision frequency is:

$$\nu_{\alpha\beta} = \sigma_0 \frac{\tilde{q}_\alpha^2 \tilde{q}_\beta^2 \tilde{n}_L}{\tilde{m}_{\alpha\beta}^2 (\tilde{v}_\alpha - \tilde{v}_\beta)^3} \lambda \tag{5.4}$$

with $\tilde{q}_s = q_s/e$, $\tilde{m}_s = m_s/m_p$, $\tilde{m}_{\alpha\beta} = m_\alpha m_\beta/(m_\alpha + m_\beta)$, $\tilde{v}_s = v_s/V_0$, $\tilde{n}_s = n_s/n_0$ and $\tilde{n}_L$ is the lowest density between n_α and n_β. λ is the Coulomb logarithm as defined in section 3.4. The charge and mass would be those of the two particles and the density would be the lowest of both. For intra-species collisions (ν_{mm} and ν_{bb}), the relative velocity of

a random pair of particle in the distribution function is statistically of the order of the thermal speed. For the inter-species collisions there are we can either use the thermal velocity when the bulk velocity is of the order of the thermal velocity, or the bulk velocity when this is large compared to the thermal speed. In order to satisfy these conditions, the following expressions are proposed:

$$\nu_{mb} = \nu_{bm} = \sigma_0 \frac{\tilde{q}_m^2 \tilde{q}_b^2 \tilde{n}_L}{\tilde{m}_{mb}^2 \left[\left(\tilde{V}_b - \tilde{V}_m \right)^2 + \tilde{v}_{T,m}^2 \right]^{3/2}} \lambda \tag{5.5}$$

$$\nu_{mm} = \sigma_0 \frac{\tilde{q}_m^4 \tilde{n}_m}{(\tilde{m}_m/2)^2 (\tilde{v}_{T,m})^3} \lambda \tag{5.6}$$

$$\nu_{bb} = \sigma_0 \frac{\tilde{q}_b^4 \tilde{n}_b}{(\tilde{m}_b/2)^2 (\tilde{v}_{T,b})^3} \lambda \tag{5.7}$$

These expressions correspond to the typical collision frequencies. However we need to take in account the correction of Nanbu and Yonemura 1998 for particles having different statistical weights as presented in section 3.5.3. For all the simulations of this thesis, we use the same number of macroparticles for both species. As a consequence, the ratio between the statistical weights equals the density ratio $W_b/W_m = n_b/n_m = f$. This means that in the RHR case for which $f = 0.01$, each particle of the main weights one hundred times more than a particle of the beam, so the main-beam collision frequency has to be multiplied by this factor n_m/n_b. In the rest of the section, this correction will be accounted for. For the parameters used in this section for the RHR case, the initial collision frequencies are then $\nu_{mb} = 0.02\ \Omega_0$, $\nu_{mm} = 20\ \Omega_0$ and $\nu_{bb} = 0.2\ \Omega_0$

The left panel of figure 5.6 displays the time evolution of the collision frequencies averaged over all pairs of particles for ν_{mb} (blue), ν_{mm} (green) and ν_{bb} (red) (for a simulation with $\sigma_0 = 0.2\ \Omega_0$). The spikes observable on these curves are associated to the very small value of the relative velocity for given pairs of particles, resulting in the divergence of the associated collision frequency. We see that the inter-species collisions frequency, although very low at early times compared to the main-main collision frequency, quickly increase to become comparable to ν_{mm}. This is a consequence of the significant slowing down of beam and a rapid decrease of the relative speed between both populations. Since ν_{mb} is very sensitive to this value, a rapid slowing down of the beam results in a strong increase of the inter-species collisions. At late times, the relative velocity tends to zero ($(V_b - V_m) \to 0$) and the thermal velocities of both populations are getting close, so the denominator in the expression of ν_{mb} becomes $m_{mb}^2 v_{T,m}^3$. As the main and the beam have the same mass, the inter-species collision frequency becomes equal to the main-main frequency ($\nu_{mb}(t) \to \nu_{mm}(t)$), which explains why both curves share the same asymptotic value.

Right panel of figure 5.6 displays the time evolution of the smoothed values of the collision frequencies, for $\sigma_0 = 0.2\ \Omega_0$. We use the same color code as in the left panel. We over-plotted the collision frequencies given by equations 5.7: $\nu_{mb}^{th}(t)$ in cyan, $\nu_{mm}^{th}(t)$ in yellow and $\nu_{bb}^{th}(t)$ in magenta. These curves show a quite good agreement, meaning that the statistical estimation make sense. The beam-beam collision frequency experiences a decrease during the growth of the magnetic field, then relaxes to a value close to the

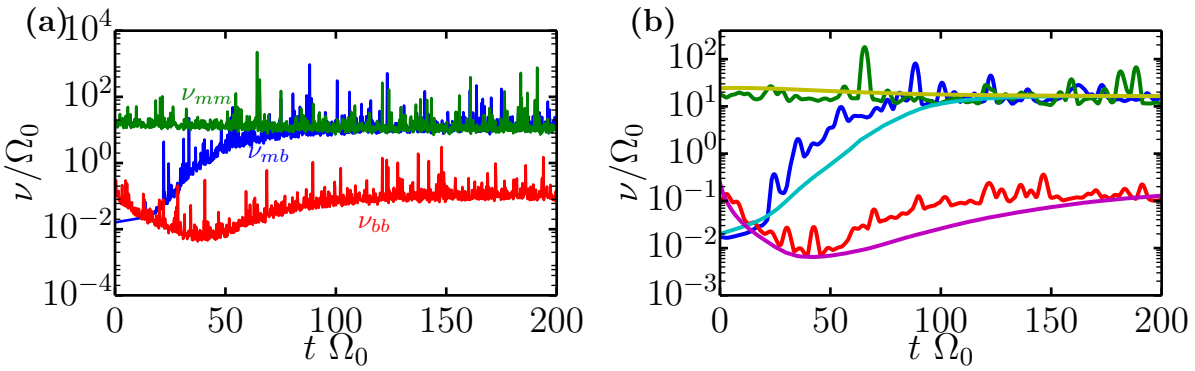

Figure 5.6: **(a)**: evolution of the collision frequencies (the inter-species (main-beam) collision frequency ν_{mb} in blue, the beam-beam frequency ν_{bb} in red and the main-main frequency ν_{mm} in green) calculated in the code with time for the RHR case with $\sigma_0 = 0.2\Omega_0$. **(b)**: evolution of the collision frequencies in the same case, with the lines smoothed in order to focus on the trend. The corresponding analytical expression 5.7 are also plotted: $\nu_{mb}^{(th)}$ in cyan, $\nu_{bb}^{(th)}$ in magenta and $\nu_{mm}^{(th)}$ in yellow.

initial one. This decreases is the consequence of the spread of the beam distribution function during the linear stage (especially due to the pitch-angle scattering), that tends to increase the relative speed between the beam particles, hence to reduce ν_{bb}.

5.3 The effects of collisions on the non-resonant and mixed cases

The NR mode shows significant differences with the RHR mode, for example the level of density perturbation or in energy exchanges. We focus in this section on the NR mode as well as what we call the "mixed case", where both RHR and NR modes can coexist. We will try to identify more clearly the specificities of each modes and the effects of collisions on them.

5.3.1 Non-resonant mode

We study the non-resonant mode with $f = 0.016$ and $V_b = 57V_0$. As detailed in section 4.3, this mode needs a very large value of the bulk velocity to grow. With such parameters, simulations in the collisionless case (see section 4.3) give $\gamma \approx 0.22\Omega_0$. As for the RHR mode, we choose a value of the σ_0 parameter which allows to see a significant effect on the mode development. In that case, the main-beam collision frequency is lower because of the highest drift speed of the beam. We take $\sigma_0 = 50\Omega_0$, which allows us to observe a substantial reduction of the magnetic field. The associated initial values for the collision frequencies are then $\nu_{mb} \approx 0.027\ \Omega_0$, $\nu_{mm} \approx 5000\ \Omega_0$ and $\nu_{bb} \approx 80\ \Omega_0$. In this case, while the inter-species collisions have approximately the same frequency as in the RHR case, the beam and the main are much more collisional here.

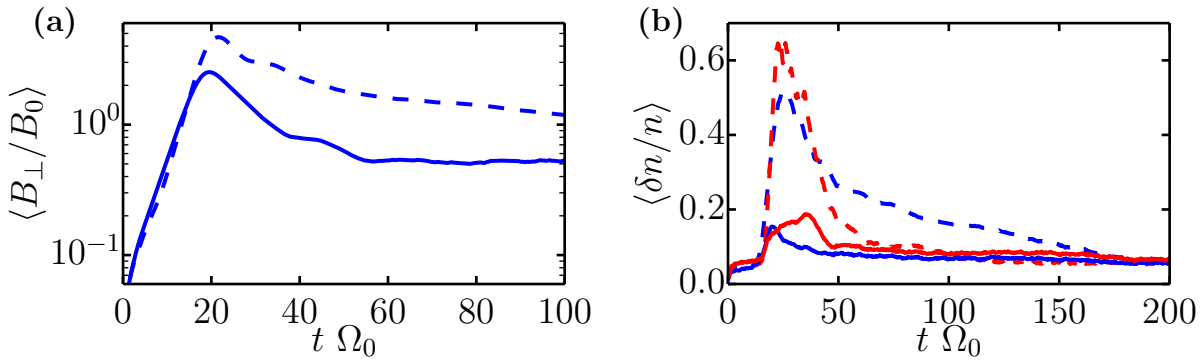

Figure 5.7: Magnetic (panel **(a)**) and relative density (panel **(b)**) perturbations for $\sigma_0 = 0$ (dashed) and $\sigma_0 = 50\Omega_0$ (plain). In panel **(b)**, the red line is the beam and the blue is the main plasma.

5.3.1.1 Development of the NR mode

Figure 5.7 **(a)** plots the magnetic perturbation as a function of time for the NR case with (plain line) and without (dashed line) collisions. As in figure 5.1 we can see that the value of the magnetic fluctuation at saturation is reduced as well as its asymptotic value. The magnetic fluctuation at saturation for $\sigma_0 = 0$ is $B_\perp^{(max)} \approx 4.7\ B_0$ while it is only $B_\perp^{(max)} \approx 2.5 B_0$ with $\sigma_0 = 50\ \Omega_0$. For the RHR mode, $\sigma_0 = 0.2\ \Omega_0$ was enough to reduce the saturation level of the magnetic field by a factor three, while for the NR mode, $\sigma_0 = 50\ \Omega_0$ "only" results in a reduction by a factor of two. Moreover the reduction of the magnetic saturation is not associated with a reduction of the instability growth rate. Instead, the saturation only happens earlier in time, which explains why is it lower in the collisional case.

Figure 5.7 (b) shows the relative density perturbation, $\delta n/n$ as a function of time for the beam (red) and the main plasma (blue). The figure shows the collisionless case with a dashed line and the collisional case with a solid line. We see that the maximum levels of density fluctuations in the collisionless case for both the beam (around $\delta n_b/n_b \approx 0.65$) and the main ($\delta n_m/n_m \approx 0.5$) are severely reduced when collisions are present. In the latter we find peak values of $\delta n/n \sim 0.1 - 0.2$ for both populations. A reduction that is consistent, but somewhat smaller, than that of the magnetic field saturation level.

5.3.1.2 Energies exchanges in the collisional NR mode

We are now interested in the impact of collisions on the particles in the NR case. Figure 5.8 **(a)** plots the evolution in time of the energies for the collisionless (dashed) and collisional cases with $\sigma_0 = 50\Omega_0$ (plain). Again as previously seen, the main difference lies in the fact that the populations are relaxed to thermal equilibrium in the presence of collisions, which gives a much bigger gap between the beam and main thermal energy density in the final phase. Another important difference is that, while in the collisionless case the beam kinetic energy takes some time before starting to decrease (about $10\Omega_0^{-1}$), this slowing down is much more rapid in the collisional case. And so are the heatings of

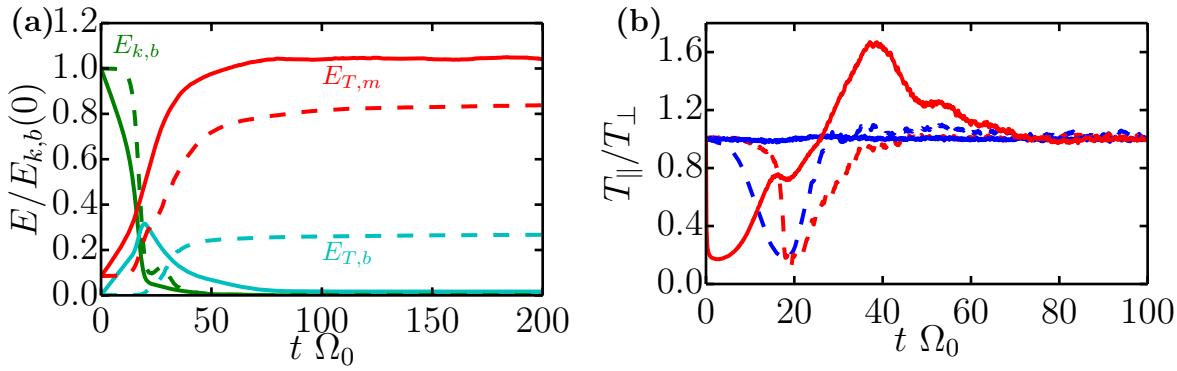

Figure 5.8: **(a)**: evolution of the energies (main plasma thermal energy $E_{T,m}$ (red) and beam kinetic (green) and thermal (cyan) energy $E_{k,b}$ and $E_{T,b}$) in the NR cases for $\sigma_0 = 0$ (collisionless) in dashed lines and $\sigma_0 = 50\Omega_0$ in solid lines. The energies are normalized by the initial beam kinetic energy $E_{k,b}(0)$. **(b)**: temperature anisotropy $T_\parallel/T_\perp$ in the NR case for the main (blue) and the beam (red) and for $\sigma_0 = 0$ (dashed) and $\sigma_0 = 50\Omega_0$ (plain).

the main and the beam. Again, this difference is due to the main-beam collisions, which slow down the beam to transform the corresponding bulk kinetic energy into heating both the beam and the main.

Figure 5.8 **(b)** presents the evolution of the temperature anisotropy for the beam (red) and the main (blue) in the collisionless (dashed lines) and $\sigma_0 = 50\Omega_0$ (plain) cases. As in the RHR case, we see that the main-main collision suppress any main anisotropy because of its high frequency (in that case $\nu_{mm,0} = 5000\Omega_0$), as already seen in the RHR case. The sharp heating in the perpendicular direction is present as well, that decreases during the linear stage of the instability. We can see that the beam anisotropy ($T_\perp < T_\parallel$) created by the instability is reduced by the beam-beam collision ($\nu_{bb} = 80\Omega_0$), and there is a relatively strong anisotropy with $T_\parallel > T_\perp$ that is created between $30 < t\Omega_0 < 70$. We distinguish three different parts: the first increase of the perpendicular temperature for $0 < t\Omega_0 < 20$, the reduction of the anisotropy compared to the collisionless case for $10 < t\Omega_0 < 30$ and the increase of the parallel temperature in $30 < t\Omega_0 < 70$. The first part was already investigated in section 5.2, with a strong heating of both the beam and the main before the instability can develop, and this thermal energy is going mainly in the perpendicular direction. The second part can be explained by the presence of beam-beam collisions, and the third part is directly linked to the second. Indeed, the non-linear collisionless processes that make the anisotropy relax to 1 after the linear stage actually increase the parallel temperature. In the presence of collisions, this process is still present and parallel temperature is still increased but the anisotropy is not so important, which creates this situation with $T_\parallel > T_\perp$ during the last phase. This anisotropy finally relaxes from $t\Omega_0 \approx 40$ because of the beam-beam collisions.

Figure 5.9 **(a)** and **(b)** show the distribution function for the main (blue colors) and the beam (red) at different times for two cases with different levels of collisionality. These are respectively $\sigma_0 = 10\Omega_0$ and $\sigma_0 = 50\Omega_0$. We can observe that as we increase the collision parameter, while the pitch-angle scattering is still present (as it is a consequence

of the development of the instability), the shape of the distribution becomes less and less anisotropic, with a parallel temperature higher when increasing σ_0. Collision have, as we know, the effect of redistributing the energy to all directions and in that case, that means that the shell observed in the collisionless case becomes broader and broader as we increase the collision frequency. Also the very distorted shape that we observed in the collisionless case (figure 4.16, second panel, with a very low density around $v_\perp = 0$ and strong inhomogeneities in the distributions function) is no longer here. These distinctive features are completely suppressed by the collisions that "fill the holes" in the distribution. As expected, any remaining relative velocity is removed when activating collisions. In the last two panels of the two figures, we observe the emergence of a two-population distribution for the beam (in red-orange): the main part, with the bean-like shape, following the normal evolution of the instability, and a population is situated in the same place as the main plasma distribution in the $(v_\parallel, v_\perp)$ space, created by the main-beam collisions as they make particles of the beam and of the main "attract" each other in the velocity space (this effect being more important as we increase σ_0). Since the main has a higher density, it has more inertia in this process, which make the beam particles being attracted to the center of the velocity space, creating this secondary population in the beam distribution function.

5.3.2 Mixed case

In the following section we use the case presented in 4.4 to study the effects of the collisions on both the right-hand resonant and the non-resonant modes simultaneously, with $f = 0.1$ and $V_b = 10V_0$. Again, we will use a specific value for the parameter $\sigma_0 = 0.4\Omega_0$, which gives $\nu_{mb,0} = 0.4\Omega_0$, $\nu_{mm,0} = 40\Omega_0$ and $\nu_{bb,0} = 4\Omega_0$. We check that for the three cases that we study here, we always have the ordering $\nu_{mb,0} \ll \nu_{bb,0} \ll \nu_{mm,0}$, which is to be expected as we deal with cold populations (with a drift velocity much lower than the thermal speed of both species $V_b \ll v_T$).

Figure 5.10 **(a)** plots the magnetic perturbation of both RHR (blue) and NR (red) modes for $\sigma_0 = 0$ and $\sigma_0 = 0.4\Omega_0$ separated using the method discussed in section 4.1.3. We see that the magnetic saturation is reduced of a factor 2.33 for the NR mode ($B_\perp^{(max)}/B_0 \approx 1.31$ for $\sigma_0 = 0$ and $B_\perp^{(max)}/B_0 \approx 0.56$ for $\sigma_0 = 0.4\Omega_0$) and of a factor 2.51 for the RHR mode ($B_\perp^{(max)}/B_0 \approx 1.18$ for $\sigma_0 = 0$ and $B_\perp^{(max)}/B_0 \approx 0.47$ for $\sigma_0 = 0.4\Omega_0$). The values are quite close, which means that it takes the same values of σ_0 to reduce both RHR and NR modes in equal proportion. This makes a difference with the previous observation made in section 5.3.1 that we need a higher value of this parameter to reach the same decrease in the saturation. This suggests that the difference is not due to the mode itself but to the condition simulated. In the simulations of the RHR and NR cases, there was mainly a large difference in the drift velocity of the beam.

Figure 5.10 **(b)** shows the energy evolution for the collisional case with $\sigma_0 = 0.4\Omega_0$ (plain lines) and the collisionless case (dashed lines), normalized with the initial beam kinetic energy $E_{k,b}^{(0)}$. While in the collisionless case, we observed a stronger heating of the beam than of the main plasma (with $E_{T,b} \approx 0.5E_{k,b}^{(0)}$ and $E_{T,m} \approx 0.7E_{k,b}^{(0)}$ in the third stage),

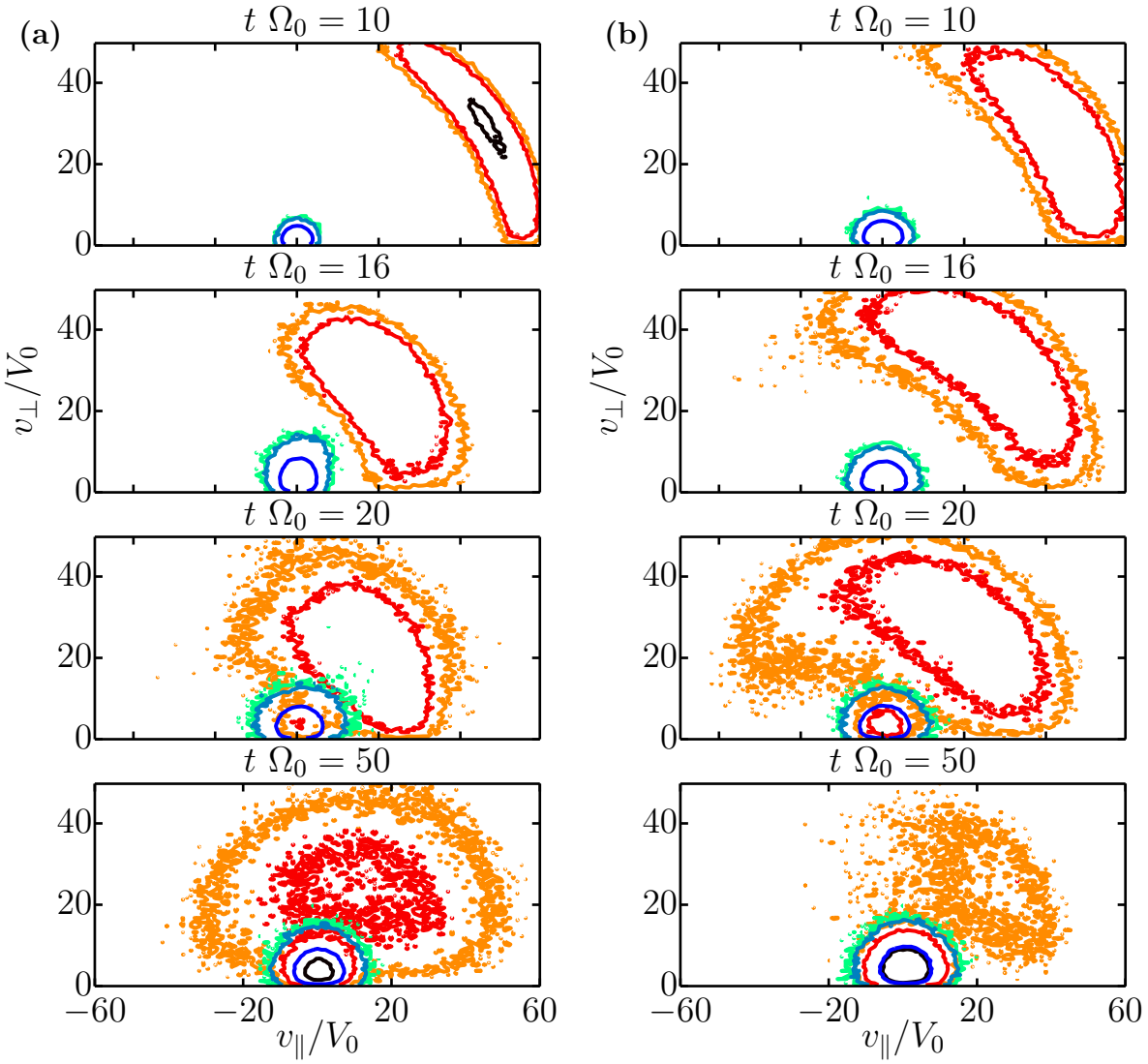

Figure 5.9: Contours of the distribution function $f(v_\parallel, v_\perp)$ in the plan $v_\parallel/v_\perp$, velocities parallel and perpendicular to the local magnetic field integrated over the spatial domain for the NR case and $\sigma_0 = 10\Omega_0$ (panel **(a)**) and $\sigma_0 = 50\Omega_0$ (panel **(b)**). The blue color scale is the main plasma and the red one corresponds to the beam. The different panels correspond to different times of the instability: $t\ \Omega_0 = 10$, $t\ \Omega_0 = 16$, $t\ \Omega_0 = 20$ and $t\ \Omega_0 = 50$.

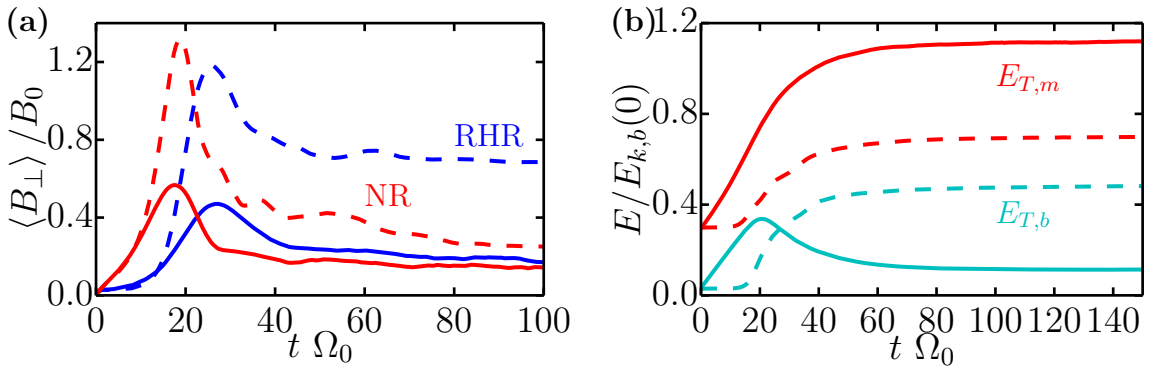

Figure 5.10: **(a)**: evolution of the magnetic perturbation for RHR (blue) and NR (red) modes and **(b)**: evolution of the thermal energies (main plasma $E_{T,m}$ (red) and beam thermal $E_{T,b}$ (cyan)) in the mixed case for $\sigma_0 = 0$ (collisionless) in dashed lines and $\sigma_0 = 0.4\Omega_0$ in solid lines. Energies are normalized by the initial beam kinetic energy $E_{k,b}(0)$.

the collisional case shows a much higher heating of the background plasma ($E_{T,m} \approx 1.1 E_{k,b}^{(0)}$ in the end) to the detriment of the beam thermal energy, that relaxes to a very low energy ($E_{T,b} \approx 0.11 E_{k,b}^{(0)}$). Again this is explained by the relaxation to thermal equilibrium induced by the collisions.

5.4 Effects of each type of collision frequency

As explained before, there are three types of collisions in the plasmas we study (ν_{mb}, ν_{mm} and ν_{bb}) and the effects of collisions inside the plasma are the sum of these three different kind of interactions. Situations where some collisions are "artificially" turned off are obviously not physical, as they only partially describe the collisional processes. However the results can helps us to gain a better understanding on the physical processes at play in the instability. Practically, this is done in the code by turning off one or more of these inter- or intra-species collisions (ν_{mm}, ν_{bb} and ν_{mb}). In this section we use the mixed case, as presented in section 5.3.2, as it provides sufficiently general information on the effects of each collisions.

As previously seen, when the RHR and NR modes are competing, they are similarly quenched by collisions. Furthermore the strong ordering between the initial values of the collision frequencies, and the fact that those two modes are reduced in the same range of σ_0, suggest that they are affected by the same type of collisions. However, we would expect the resonant modes to be more affected by beam-beam collisions, which would prevent particles from resonating. In contrast, the NR mode would be expected to be more affected by the main-beam collisions since the driving force of this mode is due to the first-order current, which is not affected by the intra-species collisions (also, since it can be described by a fluid model, the only collisions that could affect this mode are the inter-species collisions). We begin by identifying the type of collisions involved in the reductions of magnetic field saturation level that we observed in the previous sections.

	ν_{mb}	ν_{mm}	ν_{bb}
ν_{mb}	C_1	C_1	C_1
ν_{mm}		C_2	C_2
ν_{bb}			C_0

Table 5.2: Summary of the different collisional cases.

Considering the three kind of collisions (ν_{mm}, ν_{bb} and ν_{mb}), there are eight different cases corresponding to different combinations of collisions that we note C_i with i noting which type of collisions that are included:

1. collisionless case: C_0;
2. fully collisional case with all collisions enabled: C_{all};
3. without inter-species collisions, main-main and beam-beam enabled: C_{mmbb};
4. without beam-beam collisions, main-main and main-beam enabled: C_{mmmb};
5. without main-main collisions, beam-beam and main-beam enabled: C_{bbmb};
6. only inter-species collisions enabled: C_{mb};
7. only beam-beam collisions enabled: C_{bb};
8. only main-main collisions enabled: C_{mm}.

Some of these cases behave the same way and we can distinguish three different kind of behavior and group the cases accordingly:

- C_0 includes the collisionless (C_0) case and the case with only the collisions inside the beam (C_{bb}) activated;
- C_1 includes all cases with the inter-species collisions enabled: C_{all}, C_{mb}, C_{bbmb}, C_{mmmb};
- C_2 contains the cases C_{mm} and C_{mmbb};

these categories are summarized in table 5.2.

By exploring the different configurations, we can identify more precisely the type of collisions responsible for each of the effects that we observed until now. Figure 5.11 **(a)** shows the evolution of the magnetic perturbation for the mixed case, with the contribution by the RHR (blue) and NR (red) modes extracted from the data. The cases C_0, C_1 and C_2 are shown. More precisely, the dashed line corresponds to the case C_{bb} where only beam-beam collisions are enabled, and we can check that it corresponds to the collisionless case. So the collisions inside the beam have no effect on both modes in this set of parameters. The case C_1 is similar to the case with all collisions enabled. All cases that include inter-species collisions have the same behaviour. We can see that for both the cases C_0 and

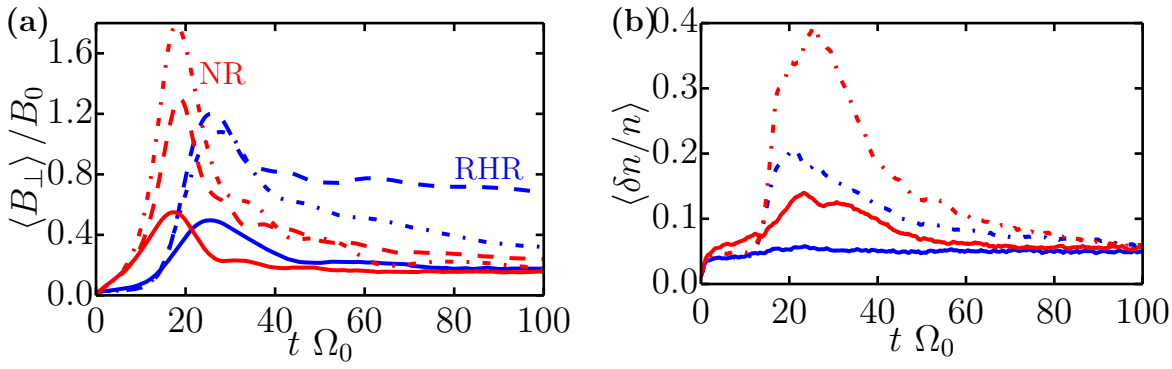

Figure 5.11: **(a)**: magnetic perturbations (RHR in blue and NR mode in red) and **(b)**: relative density perturbation (main in blue and beam in red) in the mixed for C_0 (dashed), C_1 (solid) and C_2 (dotted-dashed).

C_2, there is no observed reduction of the saturation for $0 < \sigma_0/\Omega_0 < 1$. These cases have in common the absence of inter-species (main-beam) collisions. The fact that it is the inter-species collisions which are responsible for the observed quenching of these modes, explains why both modes are reduced at the same values of σ_0. It also confirms the fact that both modes are affected in the same way. In the case C_2 (without main-beam collisions but with main-main collisions), we observe an increase in the saturation of the NR mode. This effect will be investigated in a later section (see 5.6).

Now looking at the effects of the collisions on the density perturbations, figure 5.11 **(b)** shows the evolution of the relative density variation with time ($\delta n(t)/n$), with the cases C_2 (dashed-dotted lines) and C_1 (plain lines). The case C_2, in which the inter-species collisions are disabled, has the same level of density perturbations than in the collisionless case, while the fully collisional case (C_1) shows a complete suppression of main plasma density fluctuations. The beam density is still perturbed, although at a much lower level.

Now that we have identified which type of collisions affect the evolution of the magnetic field and energy, we can draw a broader picture of the mechanisms affecting the magnetic streaming instability when adding collisions. Initially, the growing magnetic field fluctuations, driven by the instability, are very effective in slowing down the beam. However, although the main-beam collisions are initially negligible, their steep dependence on the beam's bulk speed, $\nu_{mb} \propto v_{beam}^{-3}$, means that the slowing down of the beam actually leads to a huge increase of the main-beam collisionality. These collisions can then further decelerate the beam, reducing the free energy available for the instability to grow. The perturbed magnetic field indeed saturates at lower levels, while the main-beam collisions continue to tap into the beam's bulk kinetic energy to provide an efficient heating of the main and beam plasma.

5.5 Dependence of the level of magnetic field saturation on the collision frequency

Now that we have identified the main effects of collisions on the instability and that inter-species collisions are largely responsible for the differences with the collisionless case, we investigate the dependence of the magnetic field saturation level on the collision frequency. Indeed, we already noticed for the RHR and NR cases (sections 5.2 and 5.3.1), that the saturation is reduced for a very different range of σ_0. We also saw that in the mixed case, the same two modes were affected by the same level of collisionality. In order to study the quenching of the instability by collisions, we increase the σ_0 parameter and look at the level of saturation of the instability $B^{(max)}$ reached during phase two (that gives the amount of energy that goes into the electromagnetic waves), or at the growth rate γ of each mode.

Figure 5.12 **(a)** shows the magnetic field saturation $\langle B_\perp \rangle^{(max)}/B_0$ versus the σ_0 parameter (collisionality) for the *mixed case*. The two modes are shown for different types of collisions enabled, the right-hand resonant mode is shown with a solid line, while the non-resonant mode is shown with a dashed line. In addition we colour code, the case with all collisions enabled (C_1 in black), the C_0 collisionless case in red, and the main-main collisions only (C_2) case in blue (see Table 5.2). As we increase the collision frequency (the σ_0 parameter), we observe for the "standard" case with all collisions enabled (C_1), a decrease of maximum perturbed magnetic field $B_\perp^{(max)}$, from $B_\perp^{(max)}/B_0 \approx 1.2$ with no collisions to a very low level of saturation ($B_\perp^{(max)}/B_0 \approx 0.2$). We consider the instability to be completely suppressed at this level of saturation. The results show that in a system where both modes are excited, collisions will affect the RHR and NR modes similarly, with lower energy in the saturated magnetic field over the same range of σ_0. The saturation is half of that of the collisionless case for $\sigma_0 \approx 0.3\Omega_0$ and the instability is completely suppressed when $\sigma_0 \approx 0.8 - 1\Omega_0$. Looking at the C_0 and C_2 cases, where no *inter-species* collisions are present, we can confirm that quenching of the instability comes from the presence of inter-species collisions. Interestingly, looking at the case with main-main collisions only (C_2), we observe an increase in the saturation of the NR mode while the RHR remains unchanged. This effect was also observed in the previous section in figure 5.11 and will be discussed in the next section.

Figure 5.12 **(b)** shows the growth rate γ, extracted from the simulations, as a function of σ_0. The figure shows the RHR (solid lines) and the NR (dashed) modes, again for the mixed case. As in panel **(a)** the black line corresponds to the "standard" fully collisional case (C_1) and the blue line to the case with main-main collisions only (C_2). First of all we point out that the increase of $B_\perp^{(max)}$ for the NR mode, for the case C_2, is not associated to a change of its growth rate. Indicating that main-main collisions tend to modify the saturation mechanism of NR mode (the temperature anisotropy of the main plasma) and not its initial development. We shall see this in more details later. Focusing now on the fully collisional case C_1, the results show that the decrease of the maximum perturbed magnetic field for the RHR mode is associated with a progressive reduction of its growth rate, while the decrease of $B_\perp^{(max)}$ for the NR mode is not (which is also consistent with figures 5.1 and 5.7). The decrease in the RHR growth rate can be understood by

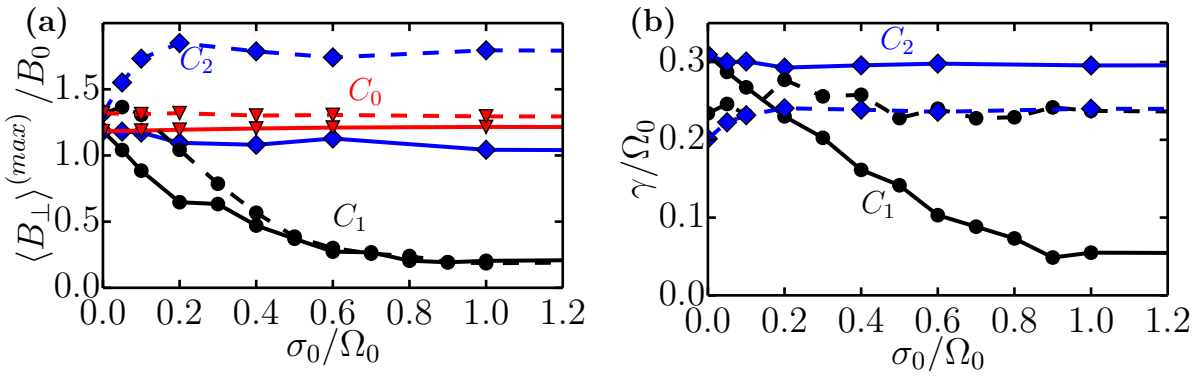

Figure 5.12: **(a)**: maximum values of the magnetic perturbation $\langle B_\perp \rangle^{(max)}/B_0$ and **(b)**: growth rates in the mixed case versus σ_0 for the different cases C_0 (only beam-beam collisions) in red, C_1 (all collisions enabled) in black and C_2 (main-main collisions) in blue. The solid line represents the RHR mode (positive helicity) and the dashed line corresponds to the NR mode (negative helicity), and all marker represent one simulation.

considering the heating of the beam that occurs right from onset of the instability in the collisional case (see section 5.2). In the mixed case presented here, the non-resonant mode grows first (see for example figure 5.10), leading to a substantial heating of the beam plasma. This means that when the RHR starts developing, at $t\ \Omega_0 = 12$, the beam has an effective thermal speed which is much higher than the initial one. At the start of the simulations we have $v_{t,b}(0) = V_0$, while by the time the RHR starts to grow $v_{T,b} \approx 2.8V_0$. The consequence of heating the beam was discussed in section 4.5.1, where we saw that increasing the temperature of the beam leads to a decrease of the growth rates of the RHR mode. The spreading of the beam distribution function means that fewer particles are able to resonate. On the other hand, the NR growth rate is affected mainly by the main plasma temperature (see section 4.5.2). Because the NR grows almost immediately, it does not feel the relatively small, initial heating of the main plasma induced by main-beam collisions. Its growth rate therefore remains constant even when the collision frequency is increased. However, we saw earlier that the collisions between main and beam ions then rapidly become important because of the slowing down of the beam. Thus effectively quenching the instability over a shorter time scale. An effect that is further exacerbated by increasing σ_0.

Figure 5.13 shows the level of saturation as a function of σ_0 for the cases where either the RHR (panel **(a)**) or the NR modes (panel **(b)**) dominate. These were studied respectively in sections 5.2 and 5.3.1. Furthermore, as it was done for figures 4.4 and 4.14, we can check that both modes have opposite helicity, and we colour code the positive helicity in blue and the negative helicity in red. Consistent with the results shown in figure 5.12 for the mixed case, the magnetic saturation decreases as we increase σ_0, albeit this time for a different range of values depending on the mode. The RHR is completely quenched at about $\sigma_0 = 0.5\Omega_0$ while it takes $\sigma_0 = 150\Omega_0$ to get the same result for the NR case.

As seen before, the inter-species collisions are responsible for a decrease of the energy going into the waves. The direct collisional interactions between the beam and the main

is more effective than the wave-mediated energy exchange. In the present case, the higher value of the beam drift velocity ($V_b = 57V_0$ against $V_b = 10V_0$ in the other cases) make the inter-species collisions initially much less frequent, which is why it takes a higher value of the σ_0 parameter to achieve the same reduction of the saturation level as in the mixed case. Using equation 5.7, we have initially for the RHR and mixed cases $\nu_{mb,0}^{(RHR)} = 0.1\sigma_0$ and for the NR case $\nu_{mb,0}^{(RHR)} = 5.10^{-4}\sigma_0$.

By plotting the magnetic saturation as a function of σ_0 $B^{(max)}(\sigma_0)/B_0$ in a log scale for the y-axis as in figure 5.13 panel **(b)**, we can see that $B_\perp^{(max)}(\sigma_0)/B_0$ follows a decreasing exponential law given by $B^{(max)} \propto e^{\Gamma\sigma_0}$ with the rate $\Gamma < 0$, at least until reaching the lowest level of saturation. The RHR and mixed cases follow the same trend (figures 5.12 **(a)** and 5.13 **(a)**) and we can calculate the value of Γ for each of these cases. This provides useful informations on the required value of σ_0 is to reduce the instability for a given set of parameters. For the NR mode we find $\Gamma \approx -0.015$, for the RHR mode $\Gamma \approx -4.68$ and for the mixed case $\Gamma^{(Mix)} \approx -2.3$ for both modes.

Given that the observed reduction is due to the main-beam collisions ν_{mb}, we compare the values of Γ to the initial value of this collision frequency. The ratio $\Gamma/(\nu_{mb,0}/\sigma_0)$ for each case gives:

$$\frac{\Gamma^{(RHR)}\sigma_0}{\nu_{mb,0}^{(RHR)}} \approx \frac{-4.68}{0.1} \approx -46.8 \tag{5.8}$$

$$\frac{\Gamma^{(NR)}\sigma_0}{\nu_{mb,0}^{(NR)}} \approx \frac{-0.015}{5.10^{-4}} \approx -30 \tag{5.9}$$

$$\frac{\Gamma^{(Mix)}\sigma_0}{\nu_{mb,0}^{(Mix)}} \approx \frac{-2.3}{0.1} \approx -23 \tag{5.10}$$

We can see that the values of the three ratio are quite close, of the same order of magnitude. This confirms that the magnetic saturation strongly depends on the main-beam collision frequency. As the inter-species collision frequency increases, collisional effects leave less energy for the magnetic field to grow and the magnetic saturation decreases. When the initial main-beam collision frequency is lower (for example, when the relative drift is higher, as in the NR case), it takes a higher value of the σ_0 parameter to reach the same level of quenching of the instability.

5.6 Other effects on the RHR and NR modes

In the previous sections, we identified the main-beam collisions as being largely responsible for modifying the instability. The results presented were restricted to the range of σ_0 where those effects were most important. However we also observed some other interesting effects, such as an increase of saturation level for NR mode when including the main-main collisions and not the main-beam collisions. In the next section, we will address two of these effects, both occurring without inter-species collisions. This kind

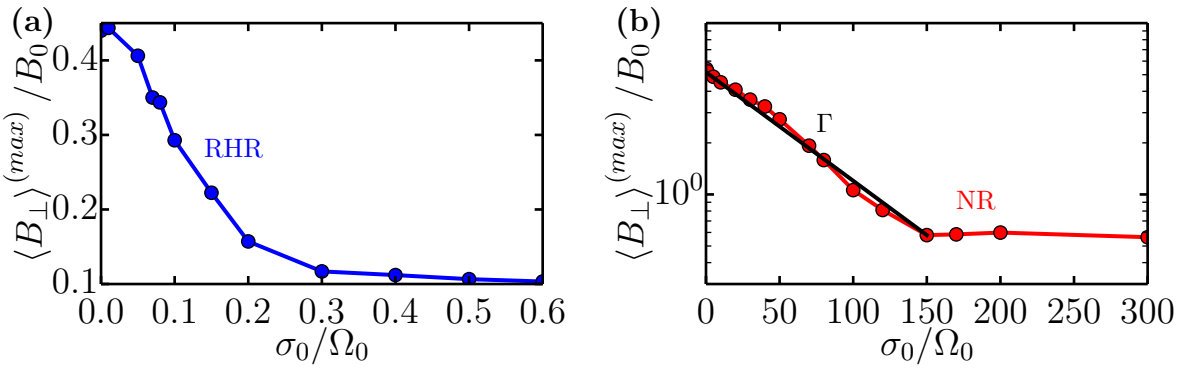

Figure 5.13: Level of saturation $\langle B_\perp \rangle^{(max)}/B_0$ depending on the σ_0 parameter in the RHR case (panel **(a)**) and the NR case (panel **(b)**) for the helicities corresponding to the resonant mode (positive helicity, blue) and the one corresponding to the non-resonant mode (negative helicity, red). Each dot corresponds to a simulations. The black line in the panel **(b)** corresponds to the decreasing rate of the saturation with σ_0.

of situations are not physical, but again they help us understand better the processes involved in the evolution of the magnetic streaming instability.

5.6.1 Quenching of the resonant mode with beam-beam collisions only

We have seen that inter-species (main-beam) collisions induce a damping of both right-hand resonant and non-resonant modes. We now investigate, in idealized simulations, the case when only intra-species collisions are present. This is the case referred previously as C_{bb}). We present results for two cases: (i) the mixed case presented in 4.4 and 5.3.2 with $f = 0.1$, $V_b = 10$ ($\nu_{bb,0} = 10\sigma_0$); (ii) the RHR case (see 4.2.2 and 5.2) with $f = 0.01$, $V_b = 10$ ($\nu_{bb,0} = \sigma_0$). We are interested in the evolution of the maximum perturbed magnetic energy when increasing σ_0 over the range $0.1 < \sigma_0/\Omega_0 < 10^8$, which is well beyond the values where the instability is quenched by the inter-species collisions. Although non-physical, the results presented here provide crucial information on the physical mechanisms at play, and a confirmation of the expected behaviour in such regimes.

Figure 5.14 **(a)** shows the evolution of the saturation level $\langle B_\perp \rangle^{(max)}/B_0$ for different σ_0 for the case with beam-beam collisions only (C_{bb}) The RHR mode in shown with solid lines and the NR mode in dashed lines; the colour coding refers to the simulations for the mixed case (black) or for the case where only the RHR mode is present (blue). We point out that to see any effect due to the beam-beam collisions requires a range of σ_0 which is very different from the range we studied until now. That is, the modes are affected only for very large beam-beam collision frequencies. The results were checked for convergence with different numerical parameters (smaller time step and longer computational domain).

First of all, we find that beam-beam collisions essentially only affect the RHR mode, whether in the mixed case or in the case where it dominates. Indeed, the NR mode is practically unaffected by a variation of more than eight orders of magnitude of σ_0. The

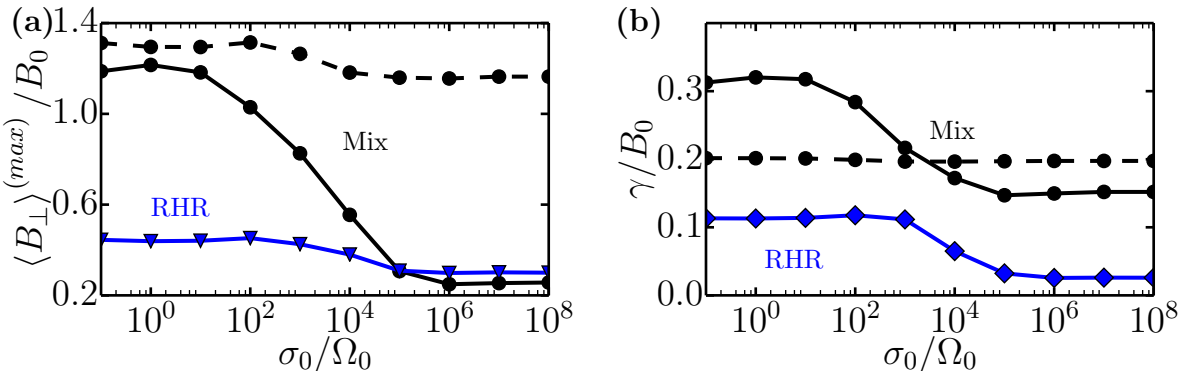

Figure 5.14: **(a)**: magnetic saturation $\langle B_\perp \rangle^{(max)}(\sigma_0)/B_0$ and **(b)**: Growth rate of the magnetic perturbation $\gamma(\sigma_0)/\Omega_0$ versus σ_0 for the case with only beam-beam collisions C_{bb}. The blue line corresponds to RHR cases studied in section 5.2 ($f = 0.01$, $V_b = 10V_0$) and the black to mixed cases studied in section 5.3 ($f = 0.1$, $V_b = 10V_0$). The solid line corresponds to the RHR (positive helicity) and the dashed line to the NR mode (negative helicity).

growth rate is seen to remain constant (fig, 5.14 **(b)**), while the saturation $\langle B_\perp \rangle^{(max)}/B_0$ only experiences a small decrease (about 11% of its initial value).

The maximum level of saturation for the RHR mode experiences a larger decrease (34% of the initial magnetic saturation for the RHR case (blue) and 78% for the mixed case (black)) over a broad range ($10 < \sigma_0/\Omega_0 < 10^5$, which explains why this effect could not be seen in section 5.2) where σ_0 was $0.2\Omega_0$. Contrary to the NR mode, this reduction of the saturation is associated with a reduction in the growth rate γ. This shows a decrease in γ that follows the decreases of the magnetic saturation in the same range of σ_0, indicating that the second is induced by the former. The RHR instability is completely damped for $\sigma_0 = 10^6\Omega_0$ for both cases, giving $\nu_{bb,0} = 10^6 - 10^7\Omega_0$. At that level of collisionality there is no evidence of any pitch-angle scattering that would reveal the presence of wave-particle interactions. Collisions keep the particles from resonating properly by ceaselessly displacing them in velocity space from a point to another, and thus stopping them from following waves coherently for times longer than $\sim 10^{-6}\Omega_0^{-1}$. Although this "demagnetization" of the particles by beam-beam collisions is expected, the level of collisionality needed shows that resonant wave-particle interactions are very effective even for episodic events of very short duration.

5.6.2 Enhancement of the non-resonant mode with main-main collisions only

Looking at the graph $\langle B_\perp \rangle^{max}(\sigma_0)/B_0$ in the *mixed case* (figure 5.12 **(a)**), we see that in the absence of main-beam collisions but in the presence of main-main collisions (case C_2), the non-resonant mode (blue dashed curve) experiences an increase in energy that is due to the main-main collisions ν_{mm}. We now investigate this further, in idealized simulations, the case where the NR mode is the dominant mode. Figure 5.15 **(a)** shows the magnetic saturation as a function of σ_0 for the case C_2 (in black) and C_0 (blue) in

the NR case (density ratio $f = 0.016$ and drift speed $V_b = 57V_0$). Indeed, we observe a similar behaviour to the mixed case, with an increase of the saturation of NR mode over a range of σ_0.

This effect is present whether the beam-beam collisions are included or not, demonstrating that it is the main-main collisions that are responsible. The impact of these collisions on the distribution functions is to isotropize the main plasma. However, as discussed in section 4.3, the non-resonant mode drives a strong anisotropy in the main plasma population. This is shown in figure 5.15 **(b)**, where the evolution of the temperature anisotropy $T_\parallel/T_\perp$ for the beam (red) and the main plasma (blue) are plotted as a function of time. The figure shows the collisionless case for $\sigma_0 = 0$ (dashed line) and the case with only main-main collisions present, C_{mm}, (solid line). The beam anisotropy is obviously unchanged because of the lack beam-beam collisions, however even if included, it's the anisotropy in the main plasma that affects the instability. Indeed, we see that main-main collisions reduce the level of anisotropy experienced by the main plasma during the growth of the instability. We also see evidence of a relatively small increase in the anisotropy between $25 < t\Omega_0 < 40$ above one. After the saturation of the instability (around $t\Omega_0 \approx 20$), a transfer of perpendicular thermal energy to parallel thermal energy relaxes the anisotropy in both cases.

We can see here that the increase in the magnetic saturation and the instability growth rate is probably related to the reduction in anisotropy induced by the main-main collisions. This result thus leads us to think that the reduction of the main anisotropy during the first and second stages increase the nonresonant mode. As we saw in section 4.5.2, increasing the main temperature has the effect of reducing the saturation of this mode through an opposition of the magnetic pressure by the thermal pressure. The main thermal pressure acts as a force that counter the development of the instability, reducing its growth rate when increasing β_m. Now, the anisotropy $T_\perp > T_\parallel$ is reduced when including the main-main collisions, which increases the growth rate of the NR mode.

So the NR mode is increase when reducing $v_{T,m}$, and for a given $v_{T,m}$ when reducing $T_\perp$. We can deduce that the force that acts against the development of this mode when increasing the main temperature comes from the perpendicular component to the local magnetic field of the main thermal velocity. The expansive motion of the electromagnetic wave is thus slowed down by the perpendicular force due to the thermal pressure that acts as a reducer to the development of the non-resonant mode, reducing its growth rate and therefore its level of saturation. By increasing $T_\perp$ during the linear stage, the non-resonant mode thus generates its own counter (the temperature anisotropy $T_\perp > T_\parallel$) feedback, and introducing the main-main collisions reduces this feedback, allowing the non-resonant mode to grow faster and reach a higher level of saturation.

5.7 Discussion

We investigated the effects of Coulomb collisions on the magnetic streaming instability, for both the right-hand resonant and the non-resonant modes. In section 5.3.2 we showed that both modes experience a decrease in their saturation level, which is directly related to the amount of magnetic energy generated by the instability as it feds on the bulk

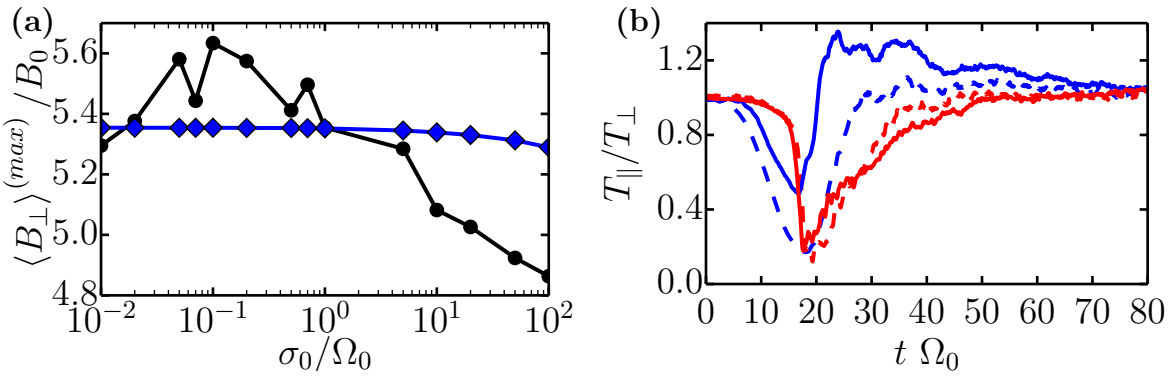

Figure 5.15: **(a)**: level of saturation with σ_0 for the NR case with the C_2 case (black) and the C_0 case (blue). **(b)**: temperature anisotropies $T_\parallel/T_\perp$ in time for the beam (red) and the main (blue) with $\sigma_0 = 0$ (dashed lines) and $\sigma_0 = 0.1\Omega_0$ and only $\nu_{mm} \neq 0$ (solid lines) in the NR case.

kinetic energy of the beam. In the case of the RHR mode, the decrease in the saturation level is associated with a reduction of the instability growth rate, which is due to the strong heating of the beam in collisional cases. For the non-resonant mode, the growth rate remains approximately constant, because the instability develops too quickly to sense any significant change in the plasma temperature. To identify which type of collisions were responsible for this behaviour, we run idealized simulation where the effects inter-species collisions (main-beam) and intra-species collisions (main-main and beam-beam) were studied separately for. These simulations demonstrated that both mode are affected by inter-species (main-beam) collisions, and that those are largely responsible of the quenching of the modes. The overall effect of collisions is schematically summarized in figure 5.16. As the beam is slowed down by the onset of the instability, intra-species collisions rapidly become dominant. These collisions can then transfer the momentum and bulk kinetic energy of the beam directly to the main plasma, creating a more efficient energy-transfer channel than the magnetic field, and thus leaving less energy for the waves to grow. Finally, over longer times, both populations relax to a thermal equilibrium.

We identify here some of the key results presented in this chapter:

- collisions lower the energy going into the waves, reducing the maximum magnetic field perturbations (saturation level) and the final amplitude of magnetic energy fluctuations;
- the reduction in the energy of the waves is associated with a reduction in the level of density perturbation;
- the collisions do not modify the most unstable wavelengths, only the amount of energy going into these waves;
- the type of collisions responsible for most of these effects is the intra-species collisions, even if their initial frequency is low compared to the other frequencies;

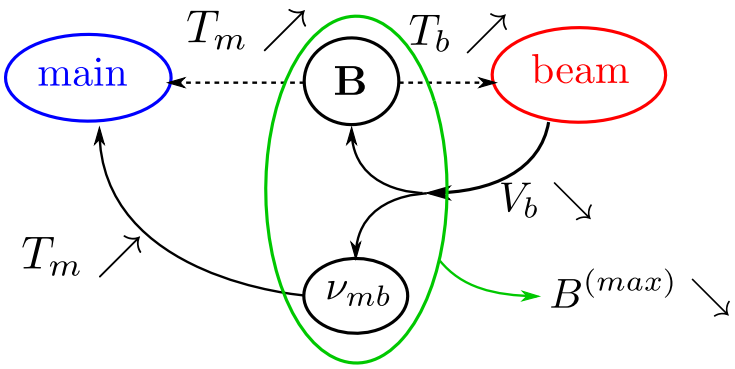

Figure 5.16: Schematic view of the behaviour of the instability in the presence of collisions. The blue and red area represent the beam and the main plasmas, **B** the electromagnetic waves, ν_{mb} the effects of inter-species collisions and the arrows represent the energy exchanges, associated with the effects on the plasmas (slowing down, heating).

- the decrease of the magnetic field saturation with σ_0 is directly linked to the initial value of the main-beam collision frequency. This is a common point between all the different cases we examined;
- idealized simulations with only beam-beam collisions present, show that at very high frequency they indeed reduce the RHR mode, by impeding the particle to resonate, while they do not affect the 'fluid-like' NR mode;
- main-main collisions tend to increase the saturation level of the NR mode. This led us to identify a feedback mechanism created by the anisotropy of the main plasma on the development of this instability.

The case of the left-hand resonant (LHR) mode was not addressed in this work because we could not highlight effects of the collisions on the development of the instability. Indeed, as soon as there were collisions involved, there was mostly a strong heating of the background and it was difficult to observe a growth of electromagnetic waves. However it can be interesting to stress some features that can be expected for this mode in the collisional case. One of the main differences in the LHR case is that this happens for a very hot beam (with $v_{T,b} \gg V_b$), which means that the ordering we saw in equation 5.1 is no longer valid since the beam-beam collision frequency is expected to be much lower than the other ones. Also, the expression for the main-beam collisions in equation 5.7 is no longer valid either since the highest velocity between the drift and the thermal speeds is no longer the drift speed. That means, as can be seen in the associated distribution function in figure 4.9, that a non-negligible portion of beam particles are close to the main in the velocity space from the start of the simulation. This makes a big difference as the main-beam collisions would then act as a very effective medium to relax both plasmas to thermal equilibrium. Also, since a very important part of the energy lies in the thermal energy of the beam, this situation would mainly lead to a heating of the main, at the expense of the development of the instability.

Chapter 6

Conclusion

> We don't need no education
> We don't need no thought control
> No dark sarcasm in the classroom
> Teachers leave them kids alone
>
> Another Brick in the Wall, Part 2 (1979), Pink Floyd.

The interaction of cosmic rays streaming in the magnetized interstellar medium is associated to processes of a major importance for solving several questions such as the long-time confinement of these cosmic-rays in the galaxy or the heating of the medium at local scales. This interactions has many aspects, among which the amplification of the interstellar magnetic field through the magnetic streaming instability. One can study this instability in laboratory, and in some conditions, collisions play an important part in its evolution. In this work, I was interested in the effects of Coulomb collisions on the development of the magnetic streaming instability.

In chapter 4, I studied the magnetic streaming instability for plasmas under different conditions, using the numerical hybrid-PIC model presented in chapter 3. I observed the presence of three different of modes that can either dominate or coexist depending the physical conditions. These are the right-hand resonant, left-hand resonant and non-resonant modes. In particular, I have been able to reproduce the left-hand resonant instability in our simulations, which, to the best of my knowledge, has not been studied before in numerical simulations. I also observed the mechanisms of wave growth predicted by analytical theory and verify some of its results. I compared my numerical results with previous analytical (Gary 1991) and numerical (Winske and Leroy 1984, Wang and Lin 2003) works, and found them to be consistent.

I developed a module, based on the works of Takizuka and Abe 1977 and Nanbu and Yonemura 1998, to simulate a Landau collision operator in order to study the effects of Coulomb collisions on the evolution of the magnetic streaming instabilities. I saw that collisions can quench the instability. Although interspecies collisions are the lowest compared to the other types of collisions, they have the most important role in the dynamics of the instability. Indeed, these collisions compete with electromagnetic field to redistribute the beam kinetic energy to the plasma, mainly in the form of thermal energy.

Collisions can thus be seen as a channel for the energy to flow between the populations in the plasma, in a much more effective way than the growth of the magnetic streaming instability.

Among the results I obtained in the collisionless and collisional cases for the magnetic streaming instability, the most important are:

- there are three distinct electromagnetic parallel mode in the magnetic streaming instability: the right-hand resonant (RHR), left-hand resonant (LHR) and non-resonant (NR);
- the RHR mode is more efficient to heat the beam, while the NR heats more the main plasma;
- the NR mode is more efficient than the others to generate strong magnetic field fluctuations;
- both RHR and NR modes are reduced when adding collisions in the system, and they are affected by the same kind of collisions: the interspecies collisions;
- interspecies collision can influence the instability even when the initial collision frequency is much smaller than growth rate;
- a big difference between the collisionless and collisional cases is that in the latter, the plasma reaches thermal equilibrium, where both the main plasma and the beam have the same temperature;
- the component of the main plasma pressure perpendicular to the magnetic field acts against the development of the NR mode and reduces the magnetic field saturation level.

On the energy point of view, it may be interesting to consider both the magnetic field and the collision as channels that guide the energy between the beam, the main and the magnetic field. In this case, this channel takes the beam kinetic energy and redistribute it to both the beam and the main in the form of thermal energy. With that perspective one can see that the collisions are much more effective than the instability to channel the energy, as they do not involve the generation of electromagnetic waves. The instability, in the other hand, takes some time before being truly effective. This point of view has its limits, however, as the effects of the instability is not limited to the transfer of energy.

The interaction of an ion beam with a charged background can be studied in laboratory, for instance with the help of a high power laser installation. Indeed, if one can manage to produce a ionized gas (for instance with a laser) and a strong enough magnetic field, one can use a beam of ions to induce the magnetic streaming instability and observe its effects. The experiments mentioned in Weidl et al. 2016 can give an experimental observation of the streaming instability, and support or refute the characteristics that I could observe in the numerical simulations. For instance, in some experimental installations, a beam of ions is produced by shooting a solid target with a laser. A magnetic field is generated in the background plasma using a Helmholtz coil. Then it is possible to measure the

energy spectrum of the particles or the amplitude of the magnetic field, which could give us informations about the efficiency of the instability to generate magnetic fields and heat the plasma.

In this study, I focused on the effects of Coulomb collisions on the magnetic streaming instability, and in particular the effects of ion-ion collisions. In some cases such as in the interstellar medium, the background is weakly ionized and the neutral atoms density (or molecules) is much higher. As a result, collisions between ions and neutrals are potentially very important. The associated complex chemistry that can occur with molecules and neutrals, as well as the ionization processes can also play an important role in the dynamics of the interstellar medium (see Padovani, Hennebelle, and Galli 2014). The full process of heating and ionization of the interstellar medium by cosmic rays, mentioned in chapter 2.2, need the inclusion of all these processes (ionization, excitation, recombination) in the model to be properly understood.

As discussed in section 3.4, the electrons are not expected to play a significant role in the dynamics of the beam in the range of parameters I used. However, for very high energy particles, or for much longer times, collisions with the electrons can become important. These can be included in the code using the method presented in Sherlock 2008 to account for collisions with a fluid background (such as the electrons) in a hybrid model.

While I only consider Maxwellian distribution functions (for the initial states) in this work, some astrophysical plasmas, such as cosmic rays, can have a very different distribution, like power-law spectrum as detailed in Zweibel 2013 (see section 2.2). Such difference can have a strong impact on the development or even the existence of a magnetic (and even electrostatic) streaming instability. Such difference should be investigated further as well. A distribution with a Lorentzian law or a kappa law, for example, could differ from the Maxwellian case I studied here. To get in a situation closer to the one of the cosmic rays, one also could investigate the influence of a power-law spectrum as a distribution function on the instability.

In the present study, I used mainly parameters with relatively high beam to main density ratio (the lowest being 1%), and beam drift velocities of a maximum of 57 Alfvén speeds. These conditions, although they allow an easy study of the different modes generated by the instability, can be very different than the ones one can find in astrophysical situations such as the interstellar medium or some supernovae shocks. It can be a good track to try to simulate parameters closer to the actual conditions of the cosmic rays in the interstellar medium. This way, one could be able to better identify the dominating modes involved in the confinement of these energetic particles.

Further, as explained in Padoan and Scalo 2005, large scale inhomogeneities in the density of the interstellar medium can lead to a confinement of the cosmic rays due to the magnetic streaming instability. Simulations of such inhomogeneous medium could allow a more precise description of the conditions needed to observe such confinement.

Bibliography

Gary, S. P. (1991). "Electromagnetic ion/ion instabilities and their consequences in space plasmas - A review". In: *Space Science Reviews* 56, pp. 373–415 (cit. on p. 127).

Winske, D. and M. M. Leroy (1984). "Diffuse ions produced by electromagnetic ion beam instabilities". In: *Journal of Geophysics Research* 89, pp. 2673–2688 (cit. on p. 127).

Wang, X. Y. and Y. Lin (2003). "Generation of nonlinear Alfvén and magnetosonic waves by beam-plasma interaction". In: *Physics of Plasmas* 10, pp. 3528–3538 (cit. on p. 127).

Takizuka, T. and H. Abe (1977). "A binary collision model for plasma simulation with a particle code". In: *Journal of Computational Physics* 25, pp. 205–219 (cit. on p. 127).

Nanbu, K. and S. Yonemura (1998). "Weighted Particles in Coulomb Collision Simulations Based on the Theory of a Cumulative Scattering Angle". In: *Journal of Computational Physics* 145, pp. 639–654 (cit. on p. 127).

Weidl, M. S. et al. (2016). "Hybrid simulations of a parallel collisionless shock in the large plasma device". In: *Physics of Plasmas* 23.12, 122102, p. 122102 (cit. on p. 128).

Padovani, M., P. Hennebelle, and D. Galli (2014). "Cosmic rays as regulators of molecular cloud properties". In: *ArXiv e-prints* (cit. on p. 129).

Sherlock, M. (2008). "A Monte-Carlo method for coulomb collisions in hybrid plasma models". In: *Journal of Computational Physics* 227, pp. 2286–2292 (cit. on p. 129).

Zweibel, E. G. (2013). "The microphysics and macrophysics of cosmic rays". In: *Physics of Plasmas* 20.5, p. 055501 (cit. on p. 129).

Padoan, P. and J. Scalo (2005). "Confinement-driven Spatial Variations in the Cosmic-Ray Flux". In: *Astrophysical Journal, Letters* 624, pp. L97–L100 (cit. on p. 129).

Abstract:

When a beam of energetic ions streams in a magnetized plasma background with a bulk velocity higher than the local Alfvén speed, it can drive electromagnetic waves unstable. The result is enhanced magnetic field fluctuations, the slowing down of the beam and plasma heating. This so-called magnetic streaming instability is commonly present in space plasma, such as streaming cosmic rays in the interstellar medium or reflected ions at shocks, as well as in laboratory plasmas. Under certain physical conditions, Coulomb collisions between ions can influence and even suppress the development of the instability. This work provides the first investigation of such effects. We study the magnetic streaming instability numerically with a hybrid-PIC code with a newly developed Monte Carlo ion-ion Coulomb collision module. Our results for the collisionless regime confirm previous studies related to the existence of resonant and non-resonant modes, and provide the groundwork for the comparison with the collisional cases. We find that collisions generally lower the amplitude of the magnetic field fluctuations, and we identify several regimes which are characterized by the competition between the growth of the instability and collisions. Even in weakly-collisional plasmas, the slowing down of the beam can actually induce a rapid increase of collisional energy exchanges, which leave less free energy for the non-linear growth of the magnetic field fluctuations and cause a more efficient heating of the plasma. For the resonant mode the enhanced heating of the beam reduces the number of particles resonating with the waves and leads to a reduction of its growth rate.

Key words: Streaming instability, Cosmic rays, Hybrid model, Polarized waves, Collisions, Resonance

Résumé :

Quand un faisceau d'ions énergétiques traverse un plasma magnétisé plus rapidement que la vitesse d'Alfvén, il peut rendre instables des modes électromagnétiques. Cela résulte en une augmentation des fluctuations magnétiques, un ralentissement du faisceau et un chauffage du plasma. Cette instabilité faisceau-plasma magnétisée est commune dans des environnements comme les rayons cosmiques dans le milieu interstellaire, les ions réfléchis au choc d'étrave terrestre, ou dans des plasmas de laboratoire. Sous certaines conditions, les collisions coulombiennes entre les ions peuvent avoir une influence et même supprimer le développement de l'instabilité. Ce travail fournit les premières recherches sur le sujet. Nous étudions l'instabilité numériquement avec un code hybride-PIC intégrant un module de collision Monte-Carlo nouvellement développé. Nos résultats pour le régime sans collision confirment les études précédentes sur la présence de modes résonants et non-résonant, et fournissent une base de comparaison pour le cas collisionnel. Nous trouvons que les collisions diminuent l'amplitude des fluctuations magnétiques, et identifions plusieurs régimes caractérisés par la compétition entre l'accroissement de l'instabilité et les collisions. Même en régime faiblement collisionnels, le ralentissement induit une augmentation rapide des échanges d'énergie collisionnels, ce qui laisse moins d'énergie libre pour l'amplification non-linéaire des fluctuations magnétiques et cause un chauffage plus efficace du plasma. Pour le mode résonant, l'augmentation du chauffage du faisceau réduit

le nombre de particules en résonance avec les ondes, réduisant du même coup son taux d'accroissement.

Mots-clés : Instabilité faisceau-plasma, Rayons cosmiques, Modèle hybride, Onde polarisée, Collisions, Résonance